Terms and Conditions of Use of Digitised Theses from Trinity College Library Dublin

Copyright statement

All material supplied by Trinity College Library is protected by copyright (under the Copyright and Related Rights Act, 2000 as amended) and other relevant Intellectual Property Rights. By accessing and using a Digitised Thesis from Trinity College Library you acknowledge that all Intellectual Property Rights in any Works supplied are the sole and exclusive property of the copyright and/or other IPR holder. Specific copyright holders may not be explicitly identified. Use of materials from other sources within a thesis should not be construed as a claim over them.

A non-exclusive, non-transferable licence is hereby granted to those using or reproducing, in whole or in part, the material for valid purposes, providing the copyright owners are acknowledged using the normal conventions. Where specific permission to use material is required, this is identified and such permission must be sought from the copyright holder or agency cited.

Liability statement

By using a Digitised Thesis, I accept that Trinity College Dublin bears no legal responsibility for the accuracy, legality or comprehensiveness of materials contained within the thesis, and that Trinity College Dublin accepts no liability for indirect, consequential, or incidental, damages or losses arising from use of the thesis for whatever reason. Information located in a thesis may be subject to specific use constraints, details of which may not be explicitly described. It is the responsibility of potential and actual users to be aware of such constraints and to abide by them. By making use of material from a digitised thesis, you accept these copyright and disclaimer provisions. Where it is brought to the attention of Trinity College Library that there may be a breach of copyright or other restraint, it is the policy to withdraw or take down access to a thesis while the issue is being resolved.

Access Agreement

By using a Digitised Thesis from Trinity College Library you are bound by the following Terms & Conditions. Please read them carefully.

I have read and I understand the following statement: All material supplied via a Digitised Thesis from Trinity College Library is protected by copyright and other intellectual property rights, and duplication or sale of all or part of any of a thesis is not permitted, except that material may be duplicated by you for your research use or for educational purposes in electronic or print form providing the copyright owners are acknowledged using the normal conventions. You must obtain permission for any other use. Electronic or print copies may not be offered, whether for sale or otherwise to anyone. This copy has been supplied on the understanding that it is copyright material and that no quotation from the thesis may be published without proper acknowledgement.

RECOVERY FACTOR AND CONJUGATE HEAT TRANSFER FOR MICRO JET IMPINGEMENT

by

Thomas Lupton

Department of Mechanical & Manufacturing Engineering,
Trinity College, Dublin.

A thesis submitted to the University of Dublin for the degree of
Doctor of Philosophy.

April, 2010

DECLARATION

I, Thomas Lupton, declare that this thesis is solely my own work except where clearly referenced. I also declare that no part of this thesis has been submitted as an exercise for any other degree at any other university.

I agree that Trinity College Library may lend or copy this thesis upon request.

Tom Lupton

Thomas Lupton

April, 2010.

"THE MORE YOU KNOW,

THE MORE YOU KNOW YOU DON'T KNOW."

—ARISTOTLE

SUMMARY

Impinging jets are renowned for achieving high rates of heat transfer over extended periods of time. The bulk of the research to date in this area has focused on relatively large diameter jets. However, the current study investigates micro jets of size less than a millimetre. The novel aspect of this research is that it investigates the significance of the effects of compressibility and conjugate heat transfer resulting from micro impinging jets. The influences of these phenomena on heat transfer resulting from larger diameter jets are generally negligible however these influences are amplified in smaller diameter jets. This study examines temperature distributions and associated recovery factors resulting from the impingement of micro, ambient temperature, air jets onto a 25 μm thick stainless steel foil. Prior to impingement the foil is at ambient temperature. However, the velocities of the impinging jets are sufficiently large enough to cause compressibility effects and consequently the temperatures of the jets are reduced. Impingement of these compressible jets results in non-uniform temperature distributions on the foil. These temperature distributions are recorded using an infrared camera with a spatial resolution of 47.5 μm.

Three different jet configurations are tested; a single jet, a 2×2 in-line jet array and a 3×3 in-line jet array, with a jet diameter of 610 μm. For the multiple jet arrays the inter-jet spacing is altered from 2.5 to 6 jet diameters. Tests are carried out at Reynolds Numbers of 5100 and 10500 which correspond to Mach numbers of 0.36 and 0.68, and the jet to impingement surface spacing is varied between 0.6 and 5 jet diameters. The effect of confinement is also investigated for a single 910 μm diameter jet by varying the distance of the confinement plate from 0 to 12 jet diameters upstream from the nozzle exit. Tests are carried out at Reynolds Numbers of 7500 and 14400 corresponding to Mach numbers of 0.36 and 0.64. The jet exit to impingement surface spacing is maintained constant, at 1 jet diameter, for the confinement study. The temperature distributions resulting from these tests show large variations in temperature over relatively small areas. This has the effect of producing significant magnitudes of lateral conduction within the foil. As both convection to/from the foil and conduction within the foil take place simultaneously, the temperature distribution recorded by the IR camera is a consequence of conjugate heat transfer. The findings from this

investigation are presented in terms of recovery factor and the heat flux distributions due to lateral conduction within the foil are also shown and discussed.

The results obtained show that the effect of nozzle to impingement surface spacing on recovery factor, R, is significant. R generally increases with increasing H/D. At low H/D values the recovery factor distributions for a single jet shows a local maximum at the jet's stagnation point and a cool annulus is formed around the stagnation point. Multiple jet interactions are found to alter the shape, magnitude and position of the recovery distributions when compared to a single jet. Circular annular zones seen for the single jet become more lobed when placed near neighbouring jets. The recovery factor distributions are linked to the amount of lateral conduction, q''_{lc}, with more significant lateral conduction corresponding to lower inter-jet spacing. The position of the stagnation point of a peripheral jet in a multi-jet array may be shifted away from the array's centre due to cross flow. The lateral conduction heat flux increases with increasing Reynolds number and decreasing H/D. The results from this study highlights heat transfer mechanisms that distinguish micro jets from larger diameter jets. This study generates a knowledge of the temperature distributions and the magnitudes of lateral conduction generated within a thin plate as a result of conjugate heat transfer generated from micro impinging jets.

ACKNOWLEDGEMENTS

TABLE OF CONTENTS

NOMENCLATURE

a	Matrix inputted to the Wiener filter
A	Area, (m^2)
b	Restored signal
Bi	Biot number, $\dfrac{hL_{char}}{k_f}$, (Dimensionless)
c	Speed of sound in air, (ms^{-1})
C	Coefficient (Dimensionless)
C_p	Specific heat capacity at constant pressure, $(J\ kg^{-1}\ K^{-1})$
d	Diameter of the spot that demonstrated a large temperature difference to the surrounding, (m)
dx	Length of an individual square pixel measured by the infrared camera, 47.5×10^{-6} (m)
D	Jet diameter, (m)
E	Emissive power, (W)
f	Fanning's friction factor, $f = \dfrac{\Delta P}{\frac{1}{2}\rho u^2 \left(L/D\right)}$, (Dimensionless)
F	Function of Reynolds number
Fr	Froude number, $Fr = \dfrac{u}{\sqrt{gD}}$, (Dimensionless)
g	Gravitational constant, $(m\ s^{-2})$
h	Heat transfer coefficient, $(W\ m^{-2}\ K^{-1})$
h*	Enthalpy per unit mass, $(J\ kg^{-1})$
H	Distance between the nozzle exit and the impingement plate, (m)
I	Current through the foil, (A)
i	Index
IR	Infrared

j	Index
k	Thermal Conductivity, (W m^{-1} K^{-1})
Kn	Knudsen number, $Kn = \dfrac{\lambda}{L_{char}}$, (Dimensionless)
L	Length, (m)
M	Mach number, $M = \dfrac{u}{c}$, (Dimensionless)
M*	Size parameter of the local neighbourhood 'η'
n	Index of matrix a used in the Wiener filter
N	Number of jets (Dimensionless)
N*	Size parameter of the local neighbourhood 'η'
Nu	Nusselt number, $Nu = \dfrac{hL_{char}}{k}$, (Dimensionless)
P	Pressure, (Pa)
P*	Power, (W)
Pr	Prandtl number, $Pr = \dfrac{\nu}{\alpha}$, (Dimensionless)
q	Rate of Heat Transfer, (W)
q″	Heat flux, (W m^{-2})
Q	Volumetric flow rate, (m^3 s^{-1})
r	Radial distance from the stagnation point, (m)
R	Recovery factor
R*	Ideal gas constant, (for air, R* = 286.9 J kg^{-1} K^{-1})
Re	Reynolds number, $Re = \dfrac{uD}{\nu}$, (Dimensionless)
S	Inter jet spacing, (m)
t	Thickness of the foil, (m)
T	Temperature, (K)
u	Velocity, (m s^{-1})
V	Voltage drop across foil, (V)
w	Uncertainty
W	Width of the heated foil, (m)
We	Weber number, $We = \dfrac{\rho u^2 D}{\sigma *}$, (Dimensionless)
x	Measurement

X	Unknown height, used in calibrating nozzle to impingement surface spacing
X*	Co-ordinate of the temperature data, [m]
z	Result of a calculation using measurement 'x'
Z	Distance of confinement plate above the nozzle's exit

Greek Symbols

α	Thermal diffusivity, $(m^2\ s^{-1})$
α^*	Absorptivity (Dimensionless)
γ	Ratio of specific heats, $\gamma = \dfrac{c_p}{c_v}$, γ = 1.4 for air (Dimensionless)
Δ	The laplacian operator (when used with temperature) Difference in pressure (when used with pressure)
ε	Emissivity (Dimensionless)
η	Local neighbourhood of a individual pixel in the matrix 'a' (Dimensionless)
θ	Angle, $(^0)$
λ	Mean free path, [m]
μ	Viscosity, (Pa s)
μ^*	Local mean around a pixel (Dimensionless)
υ	Kinematic viscosity, $(m^2\ s^{-1})$
υ^*	Standard deviation of the noise around a pixel (Dimensionless)
ρ	Density, $(kg\ m^{-3})$
ρ^*	Reflectivity (Dimensionless)
σ	Stefan-Boltzmann constant, 5.67×10^{-8} $(W\ m^{-2}\ K^{-4})$
σ^*	Surface tension, $(N\ m^{-1})$
σ^{**}	Standard deviation around a pixel (Dimensionless)
τ	Transmissivity (Dimensionless)

Subscripts

0	Stagnation
∞	Outside the thermal boundary layer

a	Adiabatic
ave	Average
b	Blackbody
c	Contraction
ch	Chamfer
char	Characteristic
conv	Convection
d	Discharge
dev	Development (length)
i	Index
lc	Lateral conduction
max	Maximum
p	At constant pressure
rad	Radiation
surr	Surroundings
u	Unheated
v	Velocity
w	Impingement surface (wall)
z	Calculated

Superscripts

m	Reynolds number exponent that proportionally relates Reynolds number to Nusselt number
n	Prandtl number exponent that proportionally relates Prandtl number to Nusselt number

LIST OF FIGURES

xiv

array and (c) a 3 x 3 square jet array.

xvii

xix

LIST OF TABLES

1 INTRODUCTION

The motivation of this research is to further the development of an innovative and effective method of cooling for electronic systems. Rapid progress in electronic devices has led to the generation of more heat and a reduction in component size. The rapid increase in heat fluxes, associated with next generation devices, will make current thermal management methods obsolete in years to come. As a result, various innovative thermal management methods are being investigated. This chapter seeks to explain the electronic thermal management problem by looking at the recent advancement of CPUs. This is followed by a discussion of some potential solutions to the thermal management problem; one of which, the focus of this study, is micro impinging jet cooling. Some of the shortfalls within the literature are identified and finally the research objectives are stated.

1.1 MOTIVATION FOR RESEARCH

The area of electronics technology is advancing swiftly: *"If the automobile industry advanced as rapidly as the Gordon Moore semiconductor industry, a Rolls Royce would get ½ million miles per gallon and it would be cheaper to throw it away than to park it."* – Moore (1998), co-founder of the Intel Corporation in 1968. The progression of the semiconductor industry has been coupled with an increased transistor population on chips. *"The number of transistors per chip has been doubling every 18 months or so, according to a general principle called Moore's law. From tens of transistors on a chip in the 1960s, we are now in the age where billion-transistor chips will be a reality,"* – Sapatnekar (2005). Transistors generate heat, and increasing the number of transistors produces increasingly more heat. The local heat flux generated by chips can be equivalent to the heat flux present in space shuttle rocket nozzles. However, microprocessors have the additional constraint of an expected life time of numerous years with maximum allowable temperatures of less than 90 ^{0}C. Failure to maintain the working environment of electronic components at the specified operating temperature can result in component failure. *"Thermal phenomena are not directly responsible for the electrical functionality and performance of semiconductor devices, but adversely affect their reliability. Three major thermally-induced reliability*

concerns for transistors are failure due to the electrostatic discharge phenomenon, stresses due to different rates of thermal expansion of transistor constituents, and failure of metallic interconnects due to diffusion or flow of atoms along a metal interconnect in the presence of a bias current, known as the electro migration phenomenon. Self-heating of the device and interconnects reduces electron mobility and results in a poor or, at best non-optimal, performance of these devices and structures," – Asheghi (2007). For silicon devices and numerous other electronic components, for instance electrolytic capacitors, the life expectancy approximately doubles for every 10 °C reduction in temperature. Currently thermal management is recognised as a pressing concern: *"the cooling needs of the electronics and computer industries for high-end applications have surpassed the capabilities of conventional methodologies such as natural convection or fan-blown air cooling."* – Garimella (2006). The importance of electronic thermal management is obvious, but the means by which thermal barriers are prohibited from obstructing component miniaturisation and processor speed amplification has yet to be resolved. Brief overviews of the various novel high performance cooling techniques for electronic devices have been formulated by Incropera (1999), Garimella (2006) and Lasance and Simons (2005); piezo fans, jets, heat pipes, microchannels and micropumps are looked at. The focus of the current research is on one of the most promising innovative cooling methods, micro jet array impingement.

1.2 RESEARCH OBJECTIVES

A comprehensive body of literature exists for heat transfer resulting from macro impinging jets, Martin (1977), Viskanta (1993), Webb and Ma (1995) and Garimella (2006). The bulk of the research conducted to date has focused on large diameter, unconfined, single jets. However, the potential use of jets in thermal management of electronic devices has generated an interest in small scale, confined, multiple jet heat transfer. In particular, as the scale of the components reduce so must the thermal management solution. As the jet scales reduce to the micro-region we pass beyond the envelope of understanding with regard to flow and heat transfer. This research seeks to further the general understanding of micro multiple jet heat transfer by identifying unresolved issues in the literature and investigating them.

The wealth of knowledge available for large scale jets cannot be conventionally scaled to describe micro jet heat transfer. Garimella and Rice (1995) tested nozzle diameters ranging from 0.79 to 6.35 mm and found the effect of nozzle diameter on heat transfer is not always captured by Nusselt number correlations. San et al. (1997) noted similar effects for jet diameters smaller than 6 mm. Pence et al. (2003) noted that direct scaling of macro scale heat transfer equations, as correlated by Martin (1977), to the micro scale is improper as the fluid flow is dynamically different. Moderate Reynolds number jet flows can correspond to high Mach numbers in micro scale jets since the small characteristic lengths result in high jet velocities. As a consequence of large jet velocities the temperature of a high speed jet, at the nozzle exit, is reduced. When such a jet impinges onto an unheated surface it results in a non uniform surface temperature distribution that is influenced by interactions between the jet and the surrounding fluid, prior to impingement. When the impingement surface is one of zero heat flux, the resulting temperature distribution is referred to as the adiabatic wall temperature distribution, $T_{a,w}$. Knowledge of $T_{a,w}$ is important, as it provides information on the thermal interaction between a jet and a surface and also $T_{a,w}$ is used commonly as the reference temperature in evaluating the heat transfer coefficient. In this study adiabatic wall temperature distributions are presented in the non-dimensional form of recovery factor distributions. The recovery factor is the ratio of the actual temperature recovered on the impingement surface to the ideal temperature change in the fluid due to adiabatic compression. Thus, when the fluid is accelerated in the jet nozzle, the temperature of the fluid decreases; when the fluid is decelerated on the impingement surface, the temperature of the fluid is increased. The recovery factor is the ratio of these two temperature differences. Due to the small scale and large temperature gradients associated with micro jet impingement the practical implementation of this cooling technology is a conjugate heat transfer problem rather than a purely convective one. As a consequence, this study also investigates the effects of lateral conduction within the impingement surface. Non uniform recovery factor distributions lead to both warm and cool regions and the effect of lateral conduction is to neutralise these regions, so conduction acts to remove heat from the warm regions and dissipate this heat to the cool regions. The heat flux levels due to lateral conduction from micro jet impingement are high and this study quantifies the magnitudes of heat flux removed from warm regions and added to cool regions.

For these reasons much of the research previously pursued at large scale needs to be investigated further at smaller scales. At small scale the use of multiple small jets is preferable to the use of a single larger jet as a single jet generally achieves high convective heat transfer in the jet's stagnation region but the cooling effect of the jet diminishes with increasing radial distance from the stagnation point. Arrays of jets increase the number of stagnation points and introduce interjet interactions, which can create high cooling secondary stagnation regions between jets, Pan and Webb (1995). Garimella and Schroder (2001) performed a study involving a 3×3, 1.59 mm diameter jet array, a 2×2, 3.18 mm diameter jet array and a single impinging jet, but the Mach numbers studied were sufficiently low to use the jet exit temperature as their reference temperature in evaluating the heat transfer coefficient; and also, their interjet spacings were maintained constant for their array studies. Goodro et al. (2007) performed a study where a large number (~90) of 3 mm diameter jets impinge onto a surface at Mach numbers up to 0.74. However they did not vary the number of jets or the non dimensional interjet spacing. The impinging jet literature seems to lack a fundamental understanding of the interaction of micro jets at large Mach number and this is what determined the objective of the current thesis.

This study considers the surface temperature distributions resulting from the impingement of jets, on an unheated metal foil. Results are presented in the form of recovery factor distributions and plots of the lateral conduction heat flux within the foil. Parameters such as nozzle-to-impingement surface spacing, interjet spacings, Reynolds number, Mach number, jet population and confinement are studied in this work. To complete the project objectives an experimental rig was designed and constructed and an effective experimental procedure was developed. Particular focus is paid to compressibility and conjugate heat transfer effects that differentiate micro jet impinging heat transfer from its large scale counterpart.

2 IMPINGING JETS

Jet impingement is a convective heat transfer method renowned for achieving high heat transfer coefficients and is utilised in numerous heat dissipation applications such as tempering of glass plates, annealing of metal sheets, drying of textile/paper products, de-icing of aircraft systems, freezing of tissue in cryosurgery, cooling of turbine blades and other thermal management systems. The flow and heat transfer characteristics of an impinging jet are affected by numerous parameters such as:

- Nozzle geometry: diameter, aspect ratio and shape,
- Flow confinement,
- Inter jet spacing (in the case of an array of jets),
- Jet exit velocity/ Reynolds number /Mach number,
- Nozzle-to-impingement surface spacing,
- Fluid surrounding the jet prior to impingement (free surface/submerged),
- Jet exit conditions, turbulence level/ development of the fluid,
- Thermal boundary condition of the heated surface,
- Prandtl number/ fluid properties,
- Impingement surface geometry/ roughness,
- Gravitational effects,
- Jet pulsations,
- Surface tension (liquid jets),
- Impingement angle.

The extent of this list indicates that impinging jet heat transfer is dependent on numerous parameters which makes it difficult to characterise it. Many researchers have correlated their empirical data for the local and area averaged heat transfer coefficients. Large deviations exist between the results reported from different studies despite experimental uncertainties of the order of 5 % being stated. Discrepancies can be attributed to differences in jet exit conditions, nozzle geometry, thermal boundary conditions, target plate geometry, experimental techniques, etc. Such inconsistency has hindered the task of understanding the

significant physical phenomena associated with impinging jets. Heat transfer from jet impingement has been reviewed comprehensively by Viskanta (1993), Lienhard (1995), Webb and Ma (1995), Martin (1977) and Garimella (2000). Contained within this section is a review of the jet impingement literature that identifies the need for the current investigation. Specific parameters are studied in this thesis and the selection of ranges over which to examine these parameters was made based on information from the literature that is outlined hereafter.

2.1 GENERAL CHARACTERISTICS OF AN IMPINGING JET

'Impingement' means 'collision' which refers to the interaction between the jet flow and the target surface. Figure 2.1 demonstrates the bulk fluid flow of a jet issuing from a nozzle and impinging perpendicularly onto a flat surface. An impinging jet can be characterised by three regions (i) the free jet region, (ii) the stagnation region and (iii) the wall-jet region.
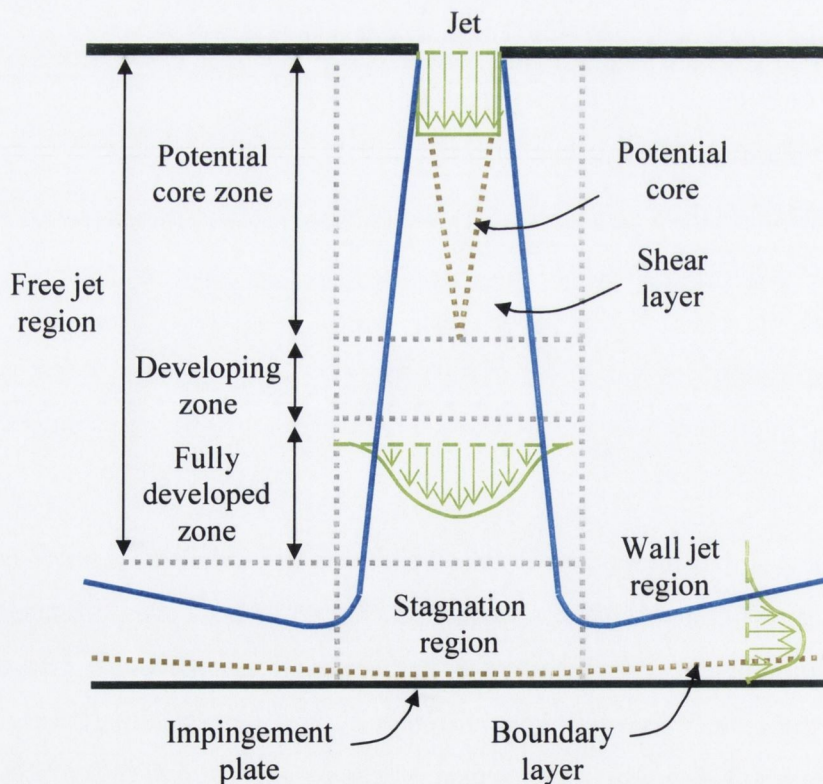
Figure 2.1, Different flow regions in an impinging jet, Geers (2003).

= Vorticity-containing fluid

Smaller scale within larger eddy

Some loss of eddy coherence due to shedding of the fluid

Entrainment

Nozzle

Potential core

Vortex rings coalesce

Wave instability of vortices grows

Entanglement of distorted vortices results in turbulent flow

Large turbulent eddies are three-dimensional wedges, not circumferentially coherent

Figure 2.2, Shear layer formation of ring vortices in a submerged jet, Yule (1978).

As the jet moves away from the nozzle its velocity is initially equal, or slightly higher as a result of compressibility effects, to the jet exit velocity of the fluid. At first, the jet acts as a free jet i.e. the presence of the impinging surface has a negligible effect on the initial jet fluid flow. As the jet advances it interacts with the surrounding ambient fluid; the edges of the jet are retarded and the speed of the ambient fluid is increased. These shear driven interactions set up a non uniform velocity profile across the jet and can modify the jet temperature (by entrainment), in the case where the ambient fluid is of a different temperature than that of the jet. In the shear layer surrounding the potential core, vortex rings form as illustrated by Yule (1978), figure 2.2. We shall examine the consequences of the vortex interactions with the flow structure in section 2.4.1. The centre of the jet which is unaffected by the shear layer is called the potential core. The potential core length can be quantified as the distance from the centreline jet exit to the point where the jet velocity retards to 95 % of its exit velocity, Livingood and Gauntner (1973) , Walker et al. (1987),

Ashforth-Frost et al. (1997) and Baydar (1999). The length of the potential core varies with Reynolds number, Re, decreasing from approximately 20 nozzle diameters to 5 nozzle diameters as Re is increased from 1000 to 4000 and increasing to approximately 6 nozzle diameters for Re > 4000, Hrycak et al. (1970). However for micro diameter jets the length of the potential core may be shorter; Garimella and Rice (1995) suggested that a 1.59 mm diameter jet at a Reynolds number of 13000 demonstrated a potential core length of 4 jet diameters. Gardon and Akfirat (1965) studied the effects of varying nozzle-to-plate spacings, H and found the stagnation Nusselt number, Nu_0, to increase slowly with increasing H values. (The stagnation Nusselt number is located at the centre of a single jet.) This trend is observed as H is increased up to the length of the potential core. As H is increased to 5 jet diameters a sharp increase in the heat transfer is noticed. This increase in Nu_0 is attributed to the increase in turbulent intensity that occurs after the potential core. Ashforth-Frost and Jambunathan (1996) have shown that the maximum value of Nu_0 occurs at a distance from the nozzle exit of approximately 110 % of the potential core length. Figure 2.3 shows typical variations in relative Nusselt number distributions with varying H/D values. This is attributed to an increase in the turbulence level just beyond a jet's potential core. The enhanced heat transfer due to increased turbulence intensity more than compensates for the loss of centreline velocity. Increasing values of H/D further leads to falling Nu_0 values, as a consequence of continuously decreasing impinging jet velocity. H/D < 1 amplifies the flow resistance and the required supply pressure without a significant improvement in the heat transfer coefficient. The results reported by Garimella and Rice (1995) indicate that this relationship between Nu_0 and H is not evident for small diameter jets. They found that for a 6.35 mm diameter jet, Nu_0 increased with increasing H/D greater than 1, following a trend exhibited by large diameter jets. However, for a 1.59 mm diameter jet, Nu_0 exhibits an absolute maximum at H/D = 1 and then continuously decreased with increasing H/D values, figure 2.4, thus demonstrating a different relationship between Nu_0 and H/D for micro jets. This observed difference in how Nu_0 varies with H/D for small diameter jets suggests the need for further study of micro jets. In the current investigation H/D values of 0.6, 1, 2, 3, 4 and 5 are studied.
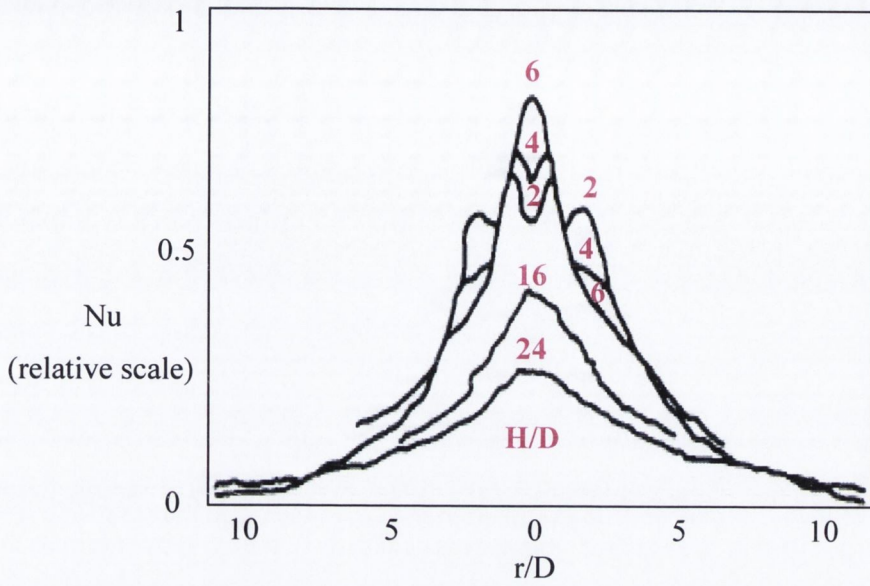
Figure 2.3, Radial variation of Nusselt number between a plate and an impinging jet for various nozzle to impingement surface spacings, Gardon and Corbonque (1962).
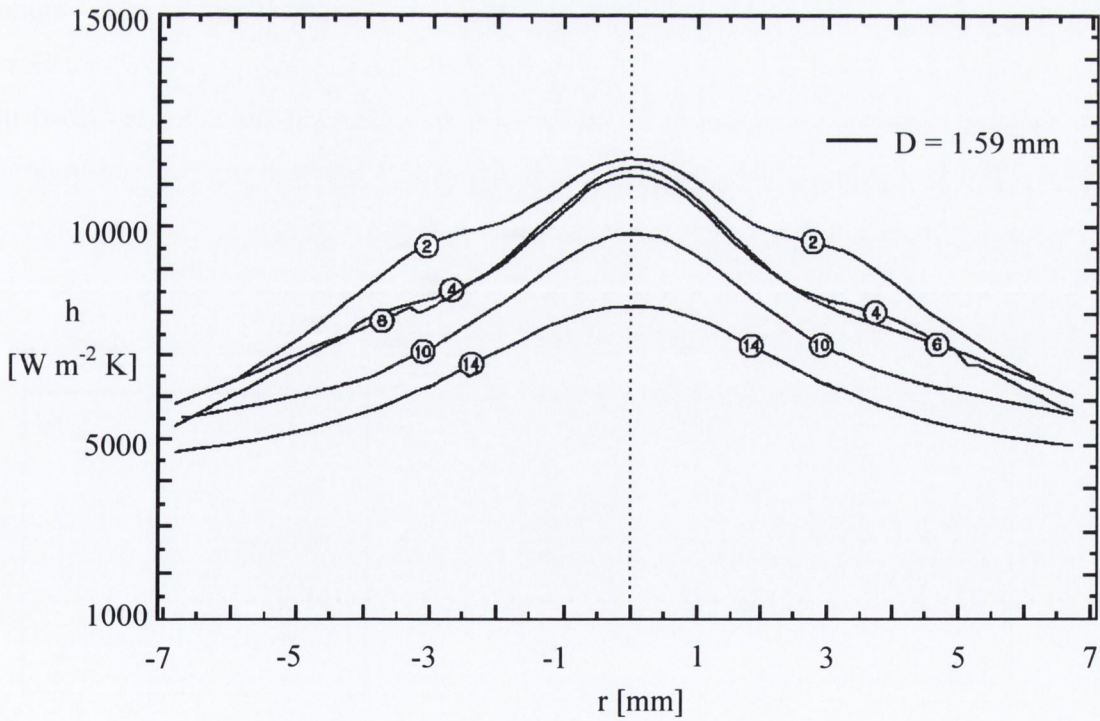
Figure 2.4, Radial variation of heat transfer coefficient between a plate and an impinging jet. Various H/D values are shown contained within the circles, Garimella and Rice (1995).

When the jet nozzle is placed at relatively large distances from the impingement surface, a developing zone exists after the potential core, figure 2.1. In this region the axial velocity decreases and the turbulence level increases. At 8 to 10 jet diameters downstream, the velocity profile becomes fully developed and the axial velocity continues decreasing while the turbulence level starts to decrease, Kataoka (1990). The influence of the impingement surface on the fluid flow initiates at approximately 1.2 jet diameters from the impingement surface, Giralt et al. (1977). The jet now moves from the free jet region to the stagnation region, where the axial transport of axial momentum and the turbulent normal stress are converted into static pressure, Nishino et al. (1996). The bulk fluid motion now changes from perpendicular to the plate to parallel to the plate and, aided by a strong favourable pressure gradient parallel to the surface, the parallel fluid flow tends to be laminar, Jen and Lavine (1995). Thin thermal and hydrodynamic boundary layers, of the order of 10 μm, are formed on the impingement surface as a result of jet deceleration and increase in pressure. These small boundary layers produce large heat transfer coefficients. Downstream from the stagnation region is the wall-jet region, figure 2.1, which initiates at r/D > 1.9, Martin (1977). The wall-jet region can be divided into two regions, Glauert (1956): an inner region where the flow and turbulence are affected by the wall and an outer region where flow conditions are determined by shear interactions with the quiescent fluid, as described in section 2.4.1. The maximum velocity occurs in the boundary between the two sub-regions after which transition to turbulence reduces the fluid's velocity.

2.2 JET CONFIGURATIONS AND FEATURES
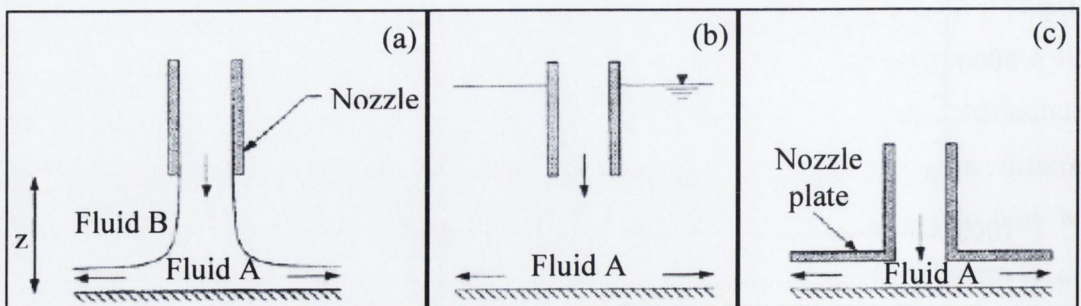
Figure 2.5, Flow configurations: (a) unconfined free-surface jet (fluid A is denser than fluid B), (b) unconfined submerged jet and (c) confined submerged jet, Narumanchi et al. (2005).

When a jet exits from a nozzle, the environment into which it enters plays a major role in the development of the jet. In figure 2.5 three different flow configurations are shown; free surface, submerged and confined. A free-surface jet is one in which the impinging jet is surrounded by a less dense fluid. This type of configuration is commonly seen when a liquid jet leaves a nozzle and is surrounded by air. Air jets were explicitly studied in this thesis but often information from studies of liquid jets is used in air jet investigations and vice versa. Garimella and Rice (1995) compared Nusselt numbers for numerous fluids and reported that Nusselt number is approximately proportional to $Pr^{0.4}$ for different fluids. However when comparing information from different fluids it is useful to be aware of interfacial effects that can exist in free jets, such as surface tension. This effect, which is significant for small diameter jets at low Reynolds numbers, can be characterised by the Weber Number, We. This dimensionless number, which represents the ratio of fluid inertia to surface tension, is useful in analysing fluid flows where an interface exists between two different types of fluids.

$$We = \frac{\rho u^2 D}{\sigma *} \qquad (2.1)$$

where,

ρ, density of the jet fluid [kg m^{-3}]

u, jet velocity [m s^{-1}]

D, jet diameter (characteristic length) [m]

$\sigma*$, surface tension [N m^{-1}]

Lienhard and Lienhard (1984) showed that the flow from an orifice will choke at a Weber number of approximately eight. Xin et al. (1993) showed how the surface tension influences the stagnation flow field for a Weber number less than a hundred. Care was taken to omit data from this literature review where surface tension effects were significant.

The second type of flow configuration shown in figure 2.5 (b) is a submerged jet. A submerged jet is one in which the ambient fluid being entrained in the jet is the same as the jet fluid. For comparable Reynolds numbers, submerged jets generally achieve higher levels of heat transfer than free-surface jets due to higher levels of fluid mixing and

turbulence, as demonstrated by Womac et al. (1993). Gravitational effects are mostly negligible in submerged jets and Lee et al. (2004a) showed that these effects can be ignored when the magnitude of the Froude number squared was greater than 100, which is the case for all tests carried out in the current investigation. The Froude Number, Fr, is a dimensionless parameter representing the ratio of the inertia forces on an element of fluid to the weight of the fluid element.

$$Fr = \frac{u}{\sqrt{gD}} \qquad\qquad (2.2)$$

where,

u, jet velocity [m s^{-1}]

g, gravitational constant [m s^{-2}]

D, jet diameter (characteristic length) [m]

The final configuration shown in figure 2.5 (c) is a confined submerged jet. Early jet impingement studies were mainly based on unconfined geometries but interest in jet impingement cooling for electronics applications where space is limited has led to confined geometries becoming a focus of interest. A confined jet is one which places a geometrical restriction, other than the impingement plate, on the jet exit flow. In this study, reference to confinement will refer to the placement of a horizontal confinement plate flush with the nozzle exit as shown in figure 2.5 (c) and figure 2.6. However, other studies have examined the effects of confining the jet exit flow with a confinement boundary perpendicular to the impingement surface. Cheng et al. (2002) achieved such a configuration by surrounding the impingement surface with a cylindrical chamber, as shown in figure 2.7.

Confined   Unconfined

W
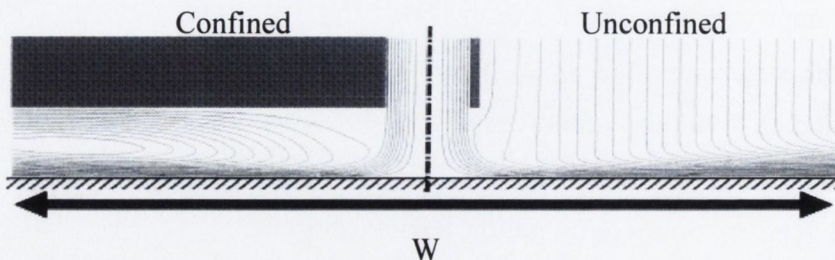
Figure 2.6, A comparison of the flow field for a confined and an unconfined jet, H/D = 1 and Re = 23000, Behnia et al. (1999).

Impingement surface   Jet   Confinement walls

Exhaust   Exhaust
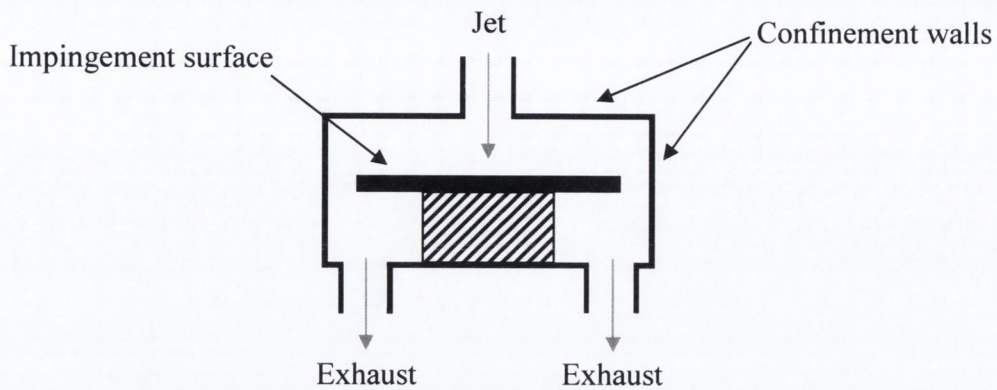
Figure 2.7, Experimental set up used by Cheng et al. (2002).

The main observed difference between a confined and unconfined impinging jet is the presence of a recirculation zone in the confined jet, figure 2.6. In studies by Fitzgerald (1997) and Ichimiya and Yamada (2003), it has been shown that the confining wall results in a recirculation zone on both the impingement surface and confinement surface for low nozzle to impingement spacings. Recirculation reduces the amount of entrainment but when the impingement surface is heated the recirculation causes warm exhaust fluid to be recirculated towards the pre-impact jet. The entrainment of this warm fluid into the pre-impact jet can alter the temperature of the jet, Voke and Gao (1998), Behnia et al. (1999) and Chua et al. (2000); this effect diminishes heat transfer, Striegl and Diller (1984). The characteristics of the recirculation are influenced by the jet Reynolds number and nozzle to target spacing. Marple (1974) and Fitzgerald and Garimella (1998) showed that the center of the flow recirculation moves away from the jet axis with increasing H/D values and increasing Reynolds number. Baydar and Ozmen (2006) studied the effects of confinement on a 25 mm diameter jet, and found the stagnation point Nusselt number to be mostly independent of the degree of confinement; this is in agreement with the results of Behnia et al. (1999). However, the findings of San et al. (1997), who tested confined jets of diameters ranging from 3 mm to 6 mm, suggest that different results may be expected for smaller diameter jets. They investigated the effects of varying W, the width of the heated impingement plate, figure 2.6, on local Nusselt numbers. They found that increasing the surface heating width, W, results in lower stagnation Nusselt numbers. They attributed this phenomenon to flow recirculation. As recirculation occurs with confined jets, and the space

constraints associated with electronics cooling applications suggest that jet confinement is likely, this thesis investigates the effects of confinement on a micro jet.

2.3 JET NOZZLE GEOMETRY

The geometry of a jet nozzle affects the turbulence levels generated in the nozzle and also the shape of the jet exit velocity profile. These effects have a major influence on the flow structures that develop near the impingement surface. Flows over an impingement surface that involve large amounts of mixing and disturbance of the thermal boundary layer growth lead to higher surface heat dissipation. From a heat transfer perspective an optimal nozzle may be thought of as one that achieves maximised heat transfer to the fluid with minimal pressure drop across the nozzle. This section looks at the effect on heat transfer of different nozzle parameters such as basic shape, diameter, aspect ratio and nozzle inlet chamfering, and equations are presented which relate to the pressure drop across a single jet and an array of jets. Knowledge of the pressure drop across the nozzle is useful as it gives an indication of the amount of energy required to drive the flow.

2.3.1 NOZZLE TYPE

This study focuses on long, circular, square edge nozzles however numerous different shaped nozzles have been studied: slot nozzles, Ichimiya and Hosaka (1992), rosette nozzles, Huber and Viskanta (1994b) and elliptical nozzles, Arjocu and Liburdy (1999). Lienhard (1995) reviewed such nozzle types and their effects on the fluid flow.

(a) Pipe exit   (b) Bell-shaped nozzle   (c) Orifice in flat plate
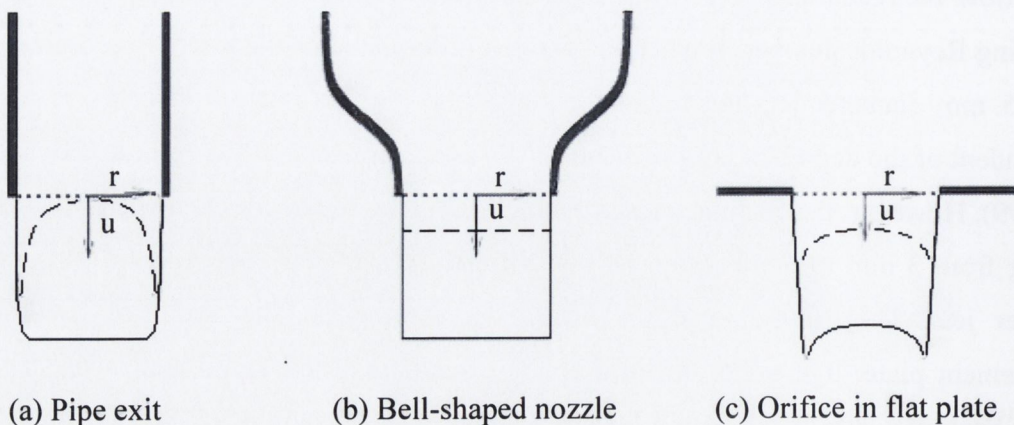
Figure 2.8, Velocity (———) and turbulent kinetic energy (– – –) profiles in jets issuing from three different nozzle types, Geers (2003).

Three basic types of circular nozzles were studied by Geers (2003), figure 2.8. A jet created from a developed turbulent pipe flow is characterised by a smooth velocity profile with high turbulent kinetic energy near the edges due to wall-friction. The circular pipe nozzle (figure 2.8 a) can be used to achieve fully developed velocity profiles for turbulent jets with a non-dimensional development length, L/D, of 20 jet diameters, Incropera (1999). (The nozzles in the current multi-jet study were initially designed to be 20 jet diameters long; however manufacturing constraints dictated that their development lengths were slightly less, as described in chapter 3.) Converging nozzles suppress boundary layer growth along the wall and thus the turbulence generated in the nozzle. The bell-shaped nozzle (figure 2.8 b) produces a jet with a homogeneous velocity profile and distribution of the turbulent kinetic energy. A sharp-edged orifice (figure 2.8 c) produces peaks in both the velocity and the turbulent kinetic energy profiles near the jet edges, due to the vena contracta effect and turbulence generated at the sharp edges. Lee and Lee (2000a) found the flow pattern of the sharp-edge nozzle to yield the highest local and area averaged Nusselt number. Vena contracta refers to the phenomenon of the jet contracting for some distance after exiting the nozzle which means the cross sectional jet flow area is smaller than that of the jet itself. The effective velocity after the nozzle exit must be found using the vena contracta instead of the nozzle area, Royne (2005). The vena contracta is determined by (i) the nozzle geometry which is characterised by the coefficient C_c and (ii) the velocity coefficient C_v, which accounts for velocity losses through the orifice, Walshaw and Jobson (1972). A discharge coefficient, C_d, is defined to take account of bulk contraction and velocity losses, $C_d = C_c \cdot C_v$. Royne and Dey (2007) theoretically quantified the pressure drop across various types of nozzles for an incompressible fluid as:

$$\Delta P = \frac{1}{2}\rho u^2 = \frac{1}{2}\rho\frac{Q^2}{C_d^2 A^2} = \rho Q^2\frac{8}{N^2\pi^2 C_d^2 D^4} \qquad (2.3)$$

where,

       ΔP, the pressure drop across the nozzle [Pa]

       ρ, the density of the fluid [kg m^{-3}]

       u, the velocity of the fluid [m s^{-1}]

       Q, the volumetric flow rate of the fluid [m^3 s^{-1}]

       C_d, the discharge coefficient of the nozzle, values of which can be seen

in Table 2.1

A, the area of the nozzle [m^2]

N, the number of jets

Table 2.1, Discharge coefficients for different nozzle configurations,
Walshaw and Jobson (1972).

Nozzle configuration	C_d
Short/straight	0.582
Long/straight	0.613
Sharp-edged	0.520
Countersunk	0.653

2.3.2 NOZZLE ASPECT RATIO

Obot et al. (1979) investigated the effect of nozzle length-to-diameter ratio on unconfined impingement heat transfer. The radial Nusselt number profiles were similar in shape for all tests but showed a considerable difference in magnitudes. Sharp edged nozzles showed greater heat transfer than contoured nozzles which agreed with results by Popiel and Boguslawski (1986). The differences between the local heat transfer profiles disappears for H/D > 6, Colucci and Viskanta (1996). Lepicovsky (1989) studied the effect of nozzle exit boundary layer, which controls the rate of jet mixing and spreading, thereby affecting the decay of the jet potential core and as a result the heat transfer distribution. It was concluded that a thin laminar boundary layer at the nozzle exit formed a shorter potential core than a thick turbulent nozzle exit boundary layer. Ashforth-Frost and Jambunathan (1996) showed that the jet potential core is up to 7 % longer for the fully developed jet exit velocity profile when compared to the flat jet exit velocity profile.

2.3.3 NOZZLE DIAMETER

A few studies have examined the effects of nozzle diameter on the heat transfer from an impinging jet. Hollworth and Gero (1985) tested air jets produced by 5 mm and 10 mm diameter square-edged orifices with an aspect ratio of 1. They found that the local Nusselt

number curves were identical for these two nozzles when tested at the same Reynolds number and H/D values. Lee et al. (2004b) studied larger diameter jets with similar findings. However, Mohanty and Tawfek (1993), who studied smaller diameter jets, found significantly different profiles for their tapered nozzles ranging in diameter from 3 to 7 mm. Garimella and Rice (1995) concluded that small diameter nozzles achieve higher heat transfer coefficients particularly in the stagnation point region: the stagnation heat transfer coefficient for a 0.79 mm diameter jet was found to be 3.5 times greater than that of a 6.35 mm diameter jet. Their experiments were carried out using a single jet of FC-77 at Re = 8500 and for H/D values ranging from 1 to 14. With fixed H/D and Re, the expectation is that the stagnation Nusselt numbers for both tests would be relatively equal in magnitude; however, assuming that the fluid thermal conductivity for both tests is similar, the stagnation Nusselt number for the 6.35 mm diameter jet is 2.3 times greater than that of the 0.79 mm jet. This suggests that the use of Nusselt number to scale micro jets is flawed. One possible reason for the difference in stagnation Nusselt number may be that these two tests were at non-dimensional heating width values, W/D, of 12.7 and 1.57 for 0.79 mm and 6.35 mm diameter tests, respectively. As discussed earlier, San et al. (1997) showed the effect of increasing the width of the heated surface, up to width of 40 D, was to reduce the heat transfer. The difference in non dimensional plate width may partially explain the difference in Nusselt numbers but it is believed that the predominant reason for the difference is the failure of the jet diameter, used as a characteristic length, to successfully non-dimensionalise small diameter jet heat transfer. San et al. (1997) also examined the effect of varying the diameter of the jet nozzle and found it to strongly affect the Nusselt number with smaller diameters having lower Nusselt numbers. San's findings indicated that the influence of the jet nozzle diameter on the Nusselt number is significant at jet diameters less than 6 mm.

2.3.4 NOZZLE CHAMFER

Brignoni and Garimella (2000) studied the effects of nozzle inlet chamfer and nozzle development length on pressure drop and heat transfer. They performed a study on nozzles with a development length of 1 jet diameter and found an inlet nozzle chamfer of 60^0, figure 2.9, resulted in a significantly lower pressure drop when compared to an inlet nozzle

chamfer of 41^0 and a square-edged nozzle. This decrease in the pressure drop may be attributed to the removal of the sharp corner at the inlet leading to an alleviation of the vena contracta within the nozzle and thus to a reduction in pressure losses. Brignoni and Garimella also varied the nozzle depth, L_{ch}, figure 2.9, and found over the range of values 0.2 D, 0.46 D and 0.73 D that 0.46 D was optimal for pressure drop. They also found chamfered nozzles achieve better average heat transfer than other geometries. Whelan and Robinson (2009) studied the influence of inlet and outlet geometry for an array of 1 mm diameter liquid jets. The nozzle geometries studied included straight, contoured and chamfered nozzles. Both submerged and free surface jets were studied and the resulting heat transfer was compared to hydraulic pumping power so as to assess the effects of various nozzle geometries, figure 2.10. They found straight nozzles with exit chamfers to achieve better average heat transfer than straight nozzles with inlet chamfers, for the same level of pumping power. Fabbri and Dhir (2005) looked at tapered arrays of circular jets with water and FC 40 as working fluids and developed an empirical expression for Fanning's friction factor as a function of Reynolds number, Re, using a least squares fit of the data.

$$f = 0.507 + \frac{189.9\mu N\pi D}{4\rho Q} = 0.507 + \frac{189.9N}{Re} \qquad (2.4)$$

where,

μ, fluid viscosity at the nozzle exit [Pa s]

N, number of jets

D, jet diameter [m]

ρ, fluid density at the nozzle exit [kg m^{-3}]

Q, volumetric flow rate [m^3 s^{-1}]

f, Fanning's friction factor

The Fanning friction factor is a non dimensional measurement of pressure:

$$f = \frac{\Delta P}{\frac{1}{2}\rho u^2 \left(\frac{L}{D}\right)} \qquad (2.5)$$

where,

ΔP, pressure loss across the nozzle

L, thickness of the nozzle

u, velocity
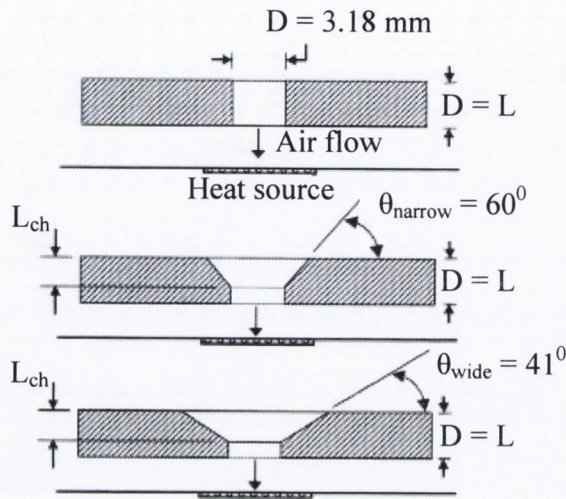
Figure 2.9, Various nozzle geometries investigated by Brignoni and Garimella (2000).

h_{ave} (kWm^{-2}K^{-1})
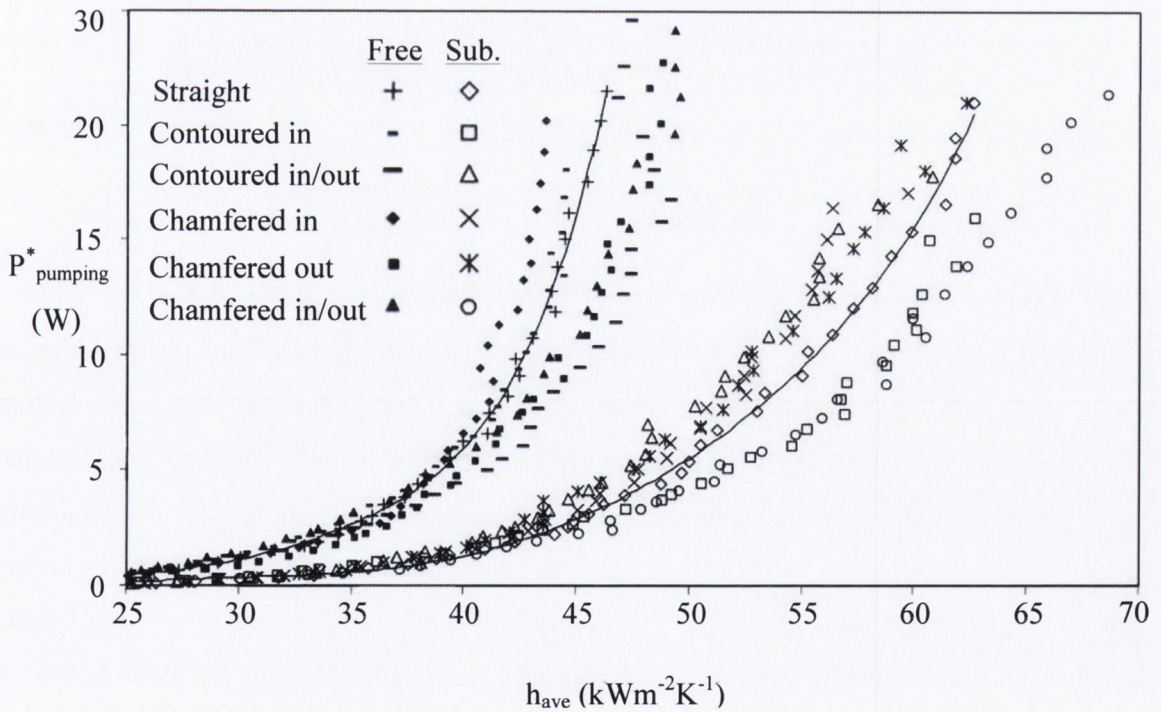
Figure 2.10, Pumping power vs. average heat transfer coefficient for nozzles with different inlet and outlet geometries. Both free and confined-submerged conditions were studied, Whelan and Robinson (2009).

2.4 JET FLOW CHARACTERISTICS

Different fluid flow regions were discussed at the beginning of this chapter, in section 2.1. This section looks in more depth at the fluid flow associated with jet impingement. Particular focus is given to the flow structures (vortices) that form in a jet's shear layer and that interact with the wall-jet. Initially this section discusses the flow in single jets and this is followed by a look at the interactions that occur between multiple jet arrays. Most of the information in this section is found from flow visualisation techniques such as that shown in figure 2.11, although associated heat transfer findings are reported for the array case.
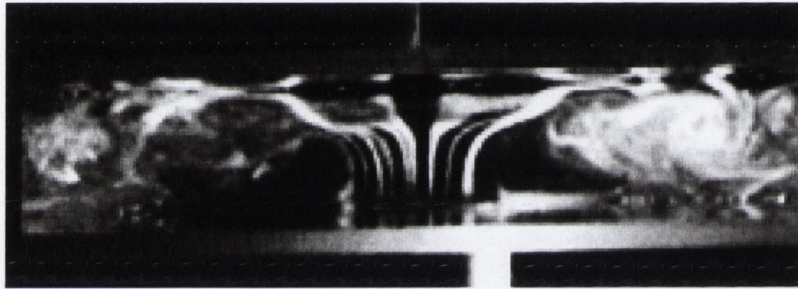
Figure 2.11, Flow entering from a confining plate, located at the bottom of the figure, and impinging upwards with Re = 4800 and H/D = 1, Baydar and Ozmen (2005).

2.4.1 SINGLE JET FLOW CHARACTERISTICS

When the jet fluid exits the nozzle it interacts with the surrounding fluid to form a shear layer. Often the velocity difference across the shear layer is sufficient to cause Kelvin Helmholtz instabilities which initiate coherent structures known as vortices. Vortices that roll-up naturally in the shear layer of the free jet, close to the nozzle exit, are initially relatively strong vortices. Much work has been carried out by O'Donovan and Murray (2007a) and (2007b) who used laser Doppler anemometry to understand the role of these vortices in determining the heat transfer resulting from an impinging jet; here follows a summary of some of their key findings. As the vortices travel they merge, forming larger yet weaker vortices, before being broken down into smaller scale random turbulence. These vortices, found around the jet's shear layer, are referred to as primary vortices, figure 2.12. Upon impingement the flow is deflected from the impingement wall and a wall-jet develops, as described in section 2.1. During impingement the primary vortices move along

the wall jet before being broken down. Chung and Luo (2002), figure 2.12 (a), who used direct numerical simulation and Lee and Lee (2000b), figure 2.12 (b), who visualised the flow using a smoke-wire technique, showed the presence of these vortical structures in the impinging jet's flow. As the primary vortices move along the wall they interact with the wall jet to form secondary vortices on the impingement surface that counter-rotate with respect to the primary vortices, Fox et al. (1993); this is shown in figure 2.13. The creation of a secondary vortex in this manner was observed by Harvey and Perry (1971) who studied how a primary vortex generated from a trailing wing-tip approached the ground and then lifted off after it approached a minimum distance. The reason for this 'rebounding effect' has been discussed by Didden and Ho (1985). As the primary vortex, contained in the inviscous region of the flow, moves towards the impingement plate it produces a fast moving stream. This stream approaches the wall and the resulting accelerating flow causes a negative wall pressure in the low pressure region downstream from the jet axis. Further downstream, pressure recovery results in an unsteady adverse pressure gradient. This retards the flow in the viscous-inviscid interface and the instability of this shear layer leads to the roll up of the vortex sheet and the formation of a secondary vortex. Fox et al. (1993) reported that the presence of secondary vortices depends on H/D. At low H/D values, the primary vortex rings approach the plate close to the stagnation point. Near the stagnation point the momentum of the wall boundary layer is low and so an adverse pressure gradient is sufficient to cause the boundary layer to separate and roll up into a secondary vortex. For larger H/D values the primary vortices approach the surface further away from the stagnation point where the boundary layer momentum is greater and as a result no separation occurs. These vortical structures strongly influence the adiabatic wall temperature distribution resulting from impinging jets as will be discussed in section 2.6.
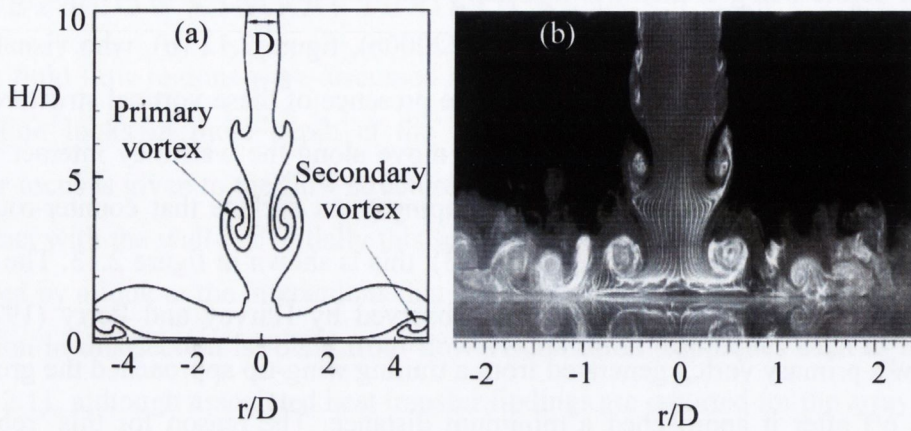
Figure 2.12, Instantaneous scalar field of an impinging jet flow, (a) Chung and Luo (2002) and (b) Lee and Lee (2000 b).
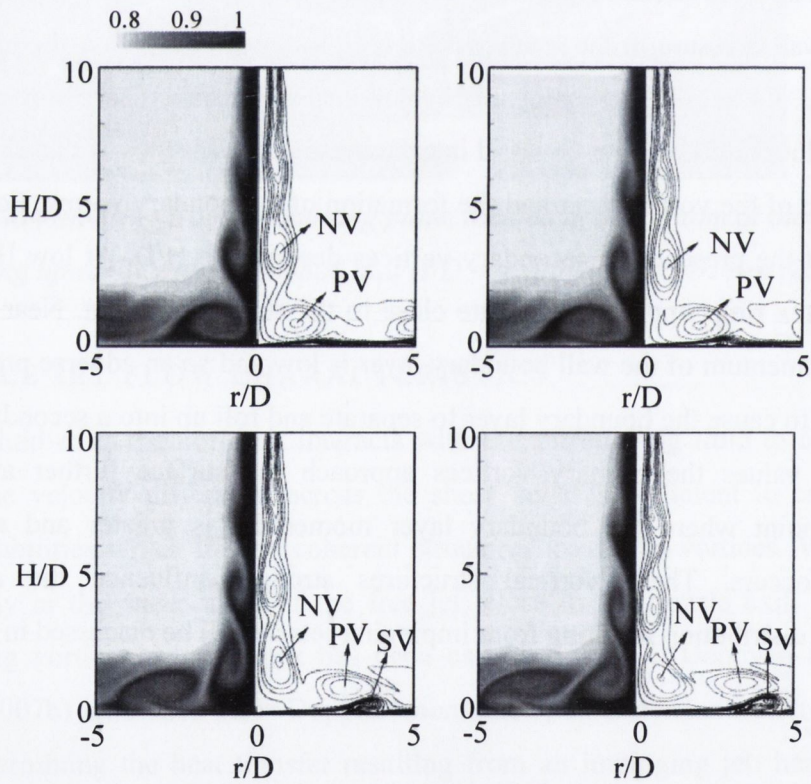
Figure 2.13, Temperature (left) and vorticity (right) contour lines for Re = 500 at approximately 1.33 second time intervals where PV is a primary vortex, NV represents the next primary vortex emanating from the jet shear layer and SV indicates a secondary vortex formed in the wall-jet region. These images were acquired from direct numerical simulation, Chung and Luo (2002).

2.4.2 JET ARRAY FLOW AND HEAT TRANSFER CHARACTERISTICS

The flow of a jet in an array differs from that of a single jet due to the interaction between neighbouring jets. In a study of free jet interactions, Lin and Sheu (1991) showed that jets can merge after a certain distance. They studied two 2 mm diameter parallel, turbulent, free (non-impinging) jets and showed that decreasing the centre to centre spacing, S, from 40 to 30 jet diameters reduces the merging distance of the two jets from 32.4 to 23.5 jet diameters. (In the present investigation, no jet merging occurs. The S/D values studied vary from 2.5 to 6 jet diameters and H/D values were less than or equal to 5.) There are two significant classes of interactions in multi-jet flows (i) free jet interactions and (ii) wall-jet interactions, as illustrated in figure 2.14. Free jet interactions are more significant with decreasing distance between adjacent jets, S, and increased nozzle to impingement surface spacing, H. The second interaction, resulting from the collision of wall-jets, is increased at small S values, decreasing H values and increasing jet velocity, Huber and Viskanta (1994a). After impingement, the collision of the wall-jets from neighbouring jets results in an upwash flow, Barata and Durao (2002). This leads to two mechanisms of discharge of the exhaust fluid, Matsumoto (1999). Part of the exhaust fluid is discharged along the nozzle plate, while more of the fluid is entrained back into the pre-impinging jet, figure 2.14 (b). At the collision of neighbouring wall-jets a secondary stagnation zone is created which achieves heat transfer coefficients up to 50 % of that experienced at the stagnation point, Pan and Webb (1995). As with the wake zone in the rear of cylinders or spheres in cross flow, the secondary stagnation region is characterised by boundary layer separation and eddying of the flow.
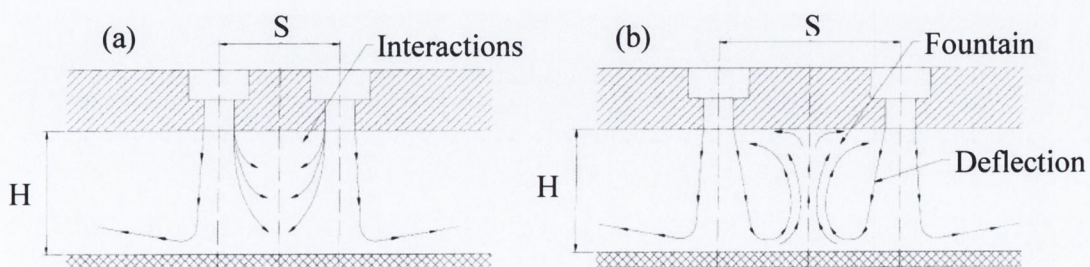
Figure 2.14, (a) Jet interaction prior to impingement (b) Jet fountain in a multi-jet after impingement, San and Lai (2001).

When numerous jets exit in an array, the resulting exhaust from centrally located jets forms a cross flow with peripheral jets. Timmers (1982) studied 3 collinear jets at small spacings and found that the maximum heat transfer coefficients of the outer jets did not occur at the geometric centres of the jets. Huber and Viskanta (1994a) found that for a 3×3 inline jet array, the Nusselt number distribution was axisymmetric for the centre jet but the outer jets were not axisymmetric but rather ovular in shape. Barata and Durao (2002), who studied submerged water jets, found that this cross flow gives rise to horseshoe type vortices around peripheral jets, as illustrated in figure 2.15. Impinging jets under strong cross flow are deflected prior to impact, which greatly reduces the magnitude of the jet velocity impinging perpendicularly onto the impingement surface. The high cross flow associated with small jet-to-target spacings (H/D~2) causes outward movement of the maxima and the non circular shape of the Nusselt number distribution for the outer jets. Interactions between the relatively warm exhaust fluid, emanating from the neighboring jets, and the relatively cool pre-impact jets have a negative effect on local Nusselt numbers. To reduce the effects of cross flow, recent developments have seen the manufacture of jet arrays which have escape holes introduced to reduce cross flow effects caused by the spent fluid, figure 2.16. Motakef (2005) reported that a jet to target spacing of one jet diameter was optimal for the micro jet array with exhaust ports, due to the reduced influence of cross flow effects on the heat transfer distribution.
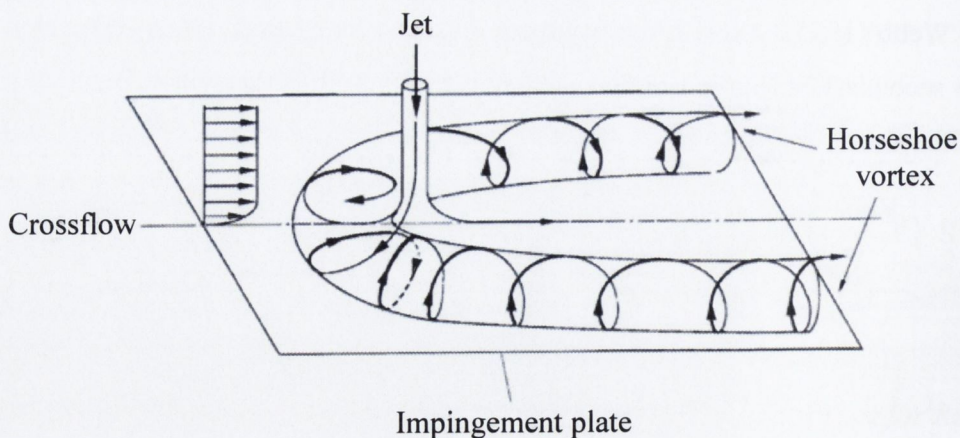
Figure 2.15, Jet impingement with low velocity cross flow, Barata and Durao (2002).
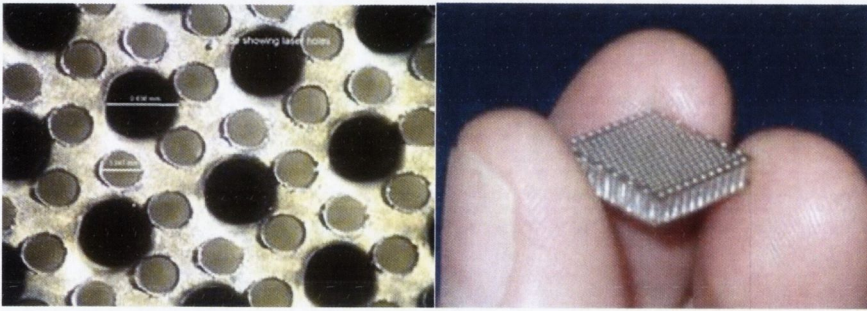
Figure 2.16, A micro jet array with jet impingement holes (large holes) surrounded by the exhaust ports (small holes), Motakef (2005).

(a) In-line   (b) Hexagonal   (c) Staggered
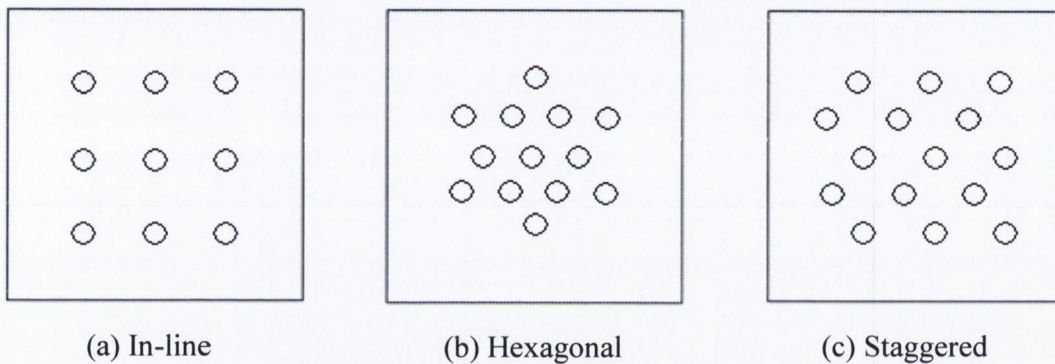
Figure 2.17, Common nozzle configurations for round impinging jets, Geers (2003).

The effect of different spatial configurations of nozzles, figure 2.17, was investigated by Geers (2003). He found that Kelvin-Helmholtz instabilities in the jet shear layer were amplified by the presence of the upwash flow, which results in shortening of the jet's potential cores. For the in-line case, this leads to elliptical impingement patterns rather than circular ones. Metzger et al. (1979) reported in-line jet configuration to provide superior heat transfer than a staggered arrangement. For the current investigation in-line jet arrays are exclusively studied.

Many researchers have varied the nozzle-to-nozzle pitch, S, and jet-to-impingement surface spacing, H, in search of optimal values. Can et al. (2002) studied a hexagonal array of round nozzle, air jets and found the maximum area-averaged heat transfer to occur at $S/D =$ 5.5, regardless of the H/D values within the range $4 \leq H/D \leq 20$. At jet to jet spacings greater than 5.5 diameters the impinged area per jet was large, which caused low area-

averaged Nusselt numbers, and at pitches less than 5.5 the negative effect on heat transfer from adjacent jet degradation was more significant than the benefit due to the increase in jet population per surface area. In the current study S/D values of 2.5, 4 and 6 are investigated.

Huber and Viskanta (1994a), who used a square array of 6.35 mm diameter air jets at S/D values of 4, 6 and 8 and with Reynolds numbers ranging from 3500 to 20400, concluded that, other things being equal, the local heat transfer rates produced by a single jet are everywhere higher than the rates produced by one jet in an array for H/D = 6, As shown in figure 2.18. However, both single and array jets demonstrate similar heat transfer as H/D is decreased to 1. The jet arrays used in figure 2.18 contained spent air exits, therefore the effects of crossflow and jet interference in the wall jet region were minimised.
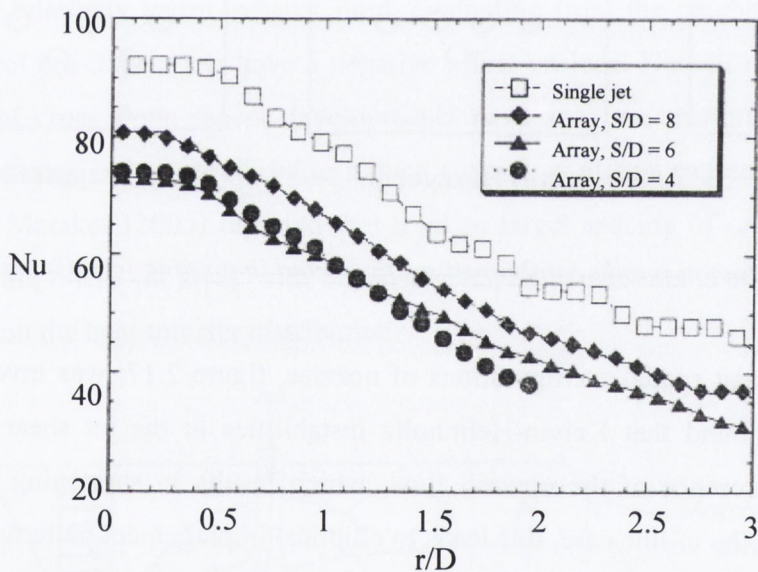
Figure 2.18, Local Nusselt number distributions from the centre jet contained within a 3×3 square array, with 6.35 mm diameter holes with various values of interjet spacings, S. Tests were carried out at H/D = 6 and Re = 10300. Contained within the orifice plate were spent air exit ports. A single jet distribution is also plotted for comparison, Huber and Viskanta (1994a).

Hollworth and Dagan (1980) found that introducing spent air exits into a staggered array increased heat transfer by 20-30 %. This suggests that if the spent air exits were blocked for

the test shown in figure 2.18, the magnitude of the difference in heat transfer between the single jet and the array jet would have been greater. However, different trends are visible for smaller diameter jets. For a 1.59 mm diameter jet, Garimella and Schroeder (2001) compared local heat transfer coefficients of a single jet, a 2×2 square array and a 3×3 square jet array; some of their results are presented in figure 2.19. They found that the central jet in the nine-jet array had considerably larger local heat transfer coefficients than the corresponding single jet at the same Reynolds number and nozzle-to-target spacing. For the four-jet array the local heat transfer coefficients for each of the four jets were comparable to that of the corresponding single-jet.
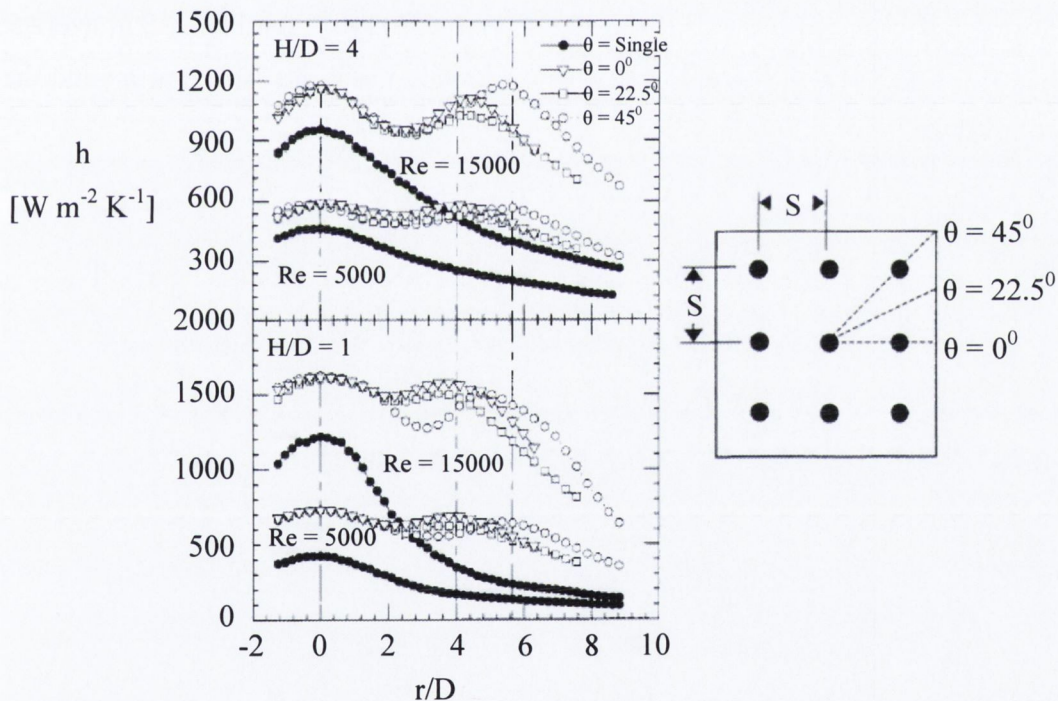
Figure 2.19, A plot of heat transfer coefficients against radial distance from the centre jet's stagnation point. The hollow symbols represent data recorded at angles θ for the 1.59 mm diameter jet array shown on the right. The vertical dashed lines indicate the centres of the array jets located at r/D = 0, 4 and 4√2 (S/D = 4). Single-jet results at the same Re and H/D values of the array data are in solid symbols, Garimella and Schroeder (2001).

Brevet et al. (2002) studied a single row of 10 mm diameter air jets impinging onto a flat plate at H/D values of 1, 2, 5 and 10, for Mach numbers < 0.1 and Re numbers ranging

from 3 000 to 20 000. They found an optimum impingement distance with maximum heat transfer rates to occur at H/D = 2 and S/D = 5. However, for smaller diameter jets, lower H/D values exhibited higher heat transfer. Thus, the results of Garimella and Schroeder (2001) for 1.59 mm diameter air jets showed that decreasing the nozzle-to-plate spacing from 4 to 1 jet diameters resulted in an increase in local heat transfer values; this effect was found to be greater for the higher Reynolds number tests. The H/D = 4 spacing demonstrated distinct peaks in heat transfer coefficient at the jet centerlines while the H/D = 1 distribution is flatter. The array heat transfer was compared with that of a single jet. It was found that the array heat transfer increases faster with increasing Reynolds number than is the case for the single jet at a H/D value of 1. Thus, the increase in average heat transfer coefficient as Reynolds number increases from 5000 to 15000 with H/D = 1 is 124 % for the array but only 87 % for the single jet. At H/D = 4, the increase in average heat transfer coefficient with Reynolds number is roughly the same for the array and the single jet (~100 %).

2.5 REYNOLDS NUMBER AND MACH NUMBER EFFECT

Reynolds Number, Re, is the ratio of inertial forces to viscous forces in a fluid.

$$Re = \frac{\rho u D}{\mu} \qquad\qquad (2.6)$$

where,

ρ, density of the fluid [kg m^{-3}]

u, jet exit velocity [m s^{-1}]

D, diameter of the nozzle [m]

μ, dynamic viscosity of the fluid [m^2 s^{-1}]

Goldstein et al. (1986) found the recovery factor to be independent of Reynolds number but most of the research into impinging jet heat transfer has studied the effects of Reynolds number on Nusselt number. The dependence of the Nusselt number on the Reynolds number has been expressed as a power-law such that $Nu \propto Re^m$. The exponent, m, is approximately 0.5 for a laminar jet flow, White (1974), but this exponent is higher for

incompressible flows with Re < 800, namely $0.7 \leq m \leq 0.83$. This is due to destabilisation of the initial laminar jet, Elison and Webb (1994). San et al. (1997) tested over a range of values, H/D = 2; $30000 \leq Re \leq 67000$; 3 mm $\leq D \leq 9$ mm; $0 \leq r/D \leq 4$; $4.17 \leq W/D \leq 37.5$, and found the local Nusselt number of a confined jet to be proportional to the 0.6375 power of the Reynolds number.

The Mach number, M, is the ratio of the jet fluid speed to the speed of sound in the same medium, and is a measure of compressibility effects in the fluid. Brevet et al. (2001) studied a single unconfined air jet, 3 mm $\leq D \leq 15$ mm, and found the influence of Mach number on local Nusselt number can be neglected for M < 0.2. Increasing the value of M tends to improve surface heat transfer. Brevet et al. (2001) established from their data that for $r/D \leq 5$ and $M \leq 0.2$ the average Nusselt number, Nu_{ave}, can be approximated by a power law dependence based on $Re^{0.74}$. For M > 0.2 they found that the dependence on Reynolds number decreases to $Re^{0.67}$. At high velocities recovery and entrainment effects are apparent and this is discussed in the next section. The jet static temperature becomes much lower than the ambient temperature as the fluid is accelerated through the nozzle. In order to calculate the static temperature of the fluid the Mach number of the flow is required and vice versa, therefore an iterative approach is taken to evaluate the static jet temperature. This method was utilised by Goodro et al. (2007) and is presented in chapter 4.

2.6 JET TEMPERATURE AND RECOVERY FACTOR IN HIGH VELOCITY FLOW

At a microscopic scale the temperature of a gas is related to the speed at which its molecules move. However, for this study we are interested in a macroscopic understanding of temperature in a moving gas which requires the definition of three separate types of temperature, Benedict (1977) and Han and Goldstein (2003):

1. Static temperature (T_{static}): the actual temperature of the gas at all times (in motion or at rest). This is the temperature that may be measured by a sensor moving at the same velocity as the fluid.

2. Dynamic temperature ($T_{dynamic}$): the thermal equivalent of the directed kinetic energy of the gas continuum.

3. Total temperature (T_{total}): the sum of the two above. This temperature can be sensed by a stationary sensor when the fluid is stagnated adiabatically so that its kinetic energy is converted into thermal energy.

In the present work air flow enters a plenum and is stagnated such that the temperature recorded by a thermocouple placed in the plenum is T_{static}. The air then leaves the plenum through a long nozzle. Knowing the volumetric flow rate of air traveling through the nozzle and using the continuity equation the average jet exit velocity is calculated. This value is then used, along with the test method described in chapter 4, for calculating T_{static} at the nozzle exit. Knowledge of this temperature allows for the calculation of air properties required to determine the Reynolds number.

A common method of quantifying the convective heat transfer between a moving fluid and a solid is via the heat transfer coefficient which can be calculated from Newton's law of cooling.

$$q_{conv\,jet} = hA(T_{h,w} - T_\infty) \qquad (2.7)$$

where,

$q_{conv\,jet}$, heat removed by forced convection [W]

h, convection heat transfer coefficient [W m^{-2} K^{-1}]

A, solid-fluid contact surface area [m^2]

$T_{h,w}$, temperature of the heated plate [K]

T_∞, fluid temperature [K]

In equation 2.7 the jet total temperature at the nozzle inlet, T_{total}, is commonly used for the value of T_∞ but it is only correct to do so when the speed of a jet is sufficiently low. For higher speed jets the impinging fluid cannot be stagnated adiabatically. Gardon and Cobonpue, (1962) recommended the use of the adiabatic wall temperature, $T_{a,w}$, as the reference temperature in the heat transfer equation when the speed of the jet is high. $T_{a,w}$, is the temperature assumed by a wall, with no heat flux, subjected to a moving fluid stream,

Meola et al. (1995) and Meola and Carlomagno (2004). In the current investigation air jets are impinged at high-speed onto an initially unheated surface resulting in a non uniform surface temperature distribution. The vortical structures, discussed in section 2.4.1, have a significant effect on the thermal fields of jets. Fox et al. (1993) noted how vortices convected in flows can separate the total temperature into region of high and low total temperature. They studied the adiabatic wall temperature distributions resulting from a single high subsonic Mach number jet impinging onto a thermally insulated flat plate. Keeping the jet temperature equal to the ambient temperature they noted the occurrence of hot and cold regions as shown in figure 2.20. Also noticeable from this figure is that the cold region, generated by the presence of the secondary vortex rings, only occurs at low H/D values, as discussed in section 2.4.1. Goldstein et al. (1986) noted this significant minimum in the radial distribution of the adiabatic wall temperature, caused by the secondary vortex rings. The adiabatic wall temperature may be non-dimensionalised to form the recovery factor, R, Goldstein and He (2001). Recovery factor is the ratio of the actual temperature recovered on the impingement surface ($T_{a,w}$ - T_{static}), due to shear work, to the ideal temperature change in the fluid due to adiabatic compression (T_{total} - T_{static}), Limaye et al. (2010), equation 2.8. When a low speed jet impinges onto a surface the resulting recovery factor distribution has a uniform magnitude of one over the entire surface. However, as the speed of the jet increases the temperature changes throughout the jet and impingement of a high speed jet can result in both warm and cool regions on the impingement surface. Warm regions, R>1, occur where the local temperature of the jet is warmer than the jet's total temperature and cool regions, R<1, occur where the local jet temperature is less than the jet's total temperature. Knowledge of the warm and cool regions of the recovery factor distributions are informative as they give an indication as to how an impinging jet cools or heats a surface. Under normal testing conditions the total temperature of air in a room changes with time; this makes it difficult to compare multiple adiabatic wall temperature distributions to one another as they lack a common reference temperature. However, when adiabatic wall temperature distributions are non-dimensionalised to form the recovery factor distributions the data are easily compared as R = 1 acts as a common reference value for all recovery factors. R = 1 signifies that the adiabatic wall temperature is equal to the total temperature of jet; this is the temperature of the jet recorded in the plenum. The recovery factor is important as it is used in calculating

$T_{a,w}$, which is used as the reference temperature in evaluating heat transfer coefficients. Once the desired initial jet temperature, T_{total}, and the speed of the jet, u, are known an adiabatic temperature distribution can be calculated by rearranging the latter part of equation 2.9 and using R.

$$R = \frac{T_{a,w} - T_{static}}{T_{total} - T_{static}} = 1 + \frac{T_{a,w} - T_{total}}{u^2 / 2C_P} \qquad (2.8)$$

where,

T_{total}, jet total temperature (measured in the plenum) [K]
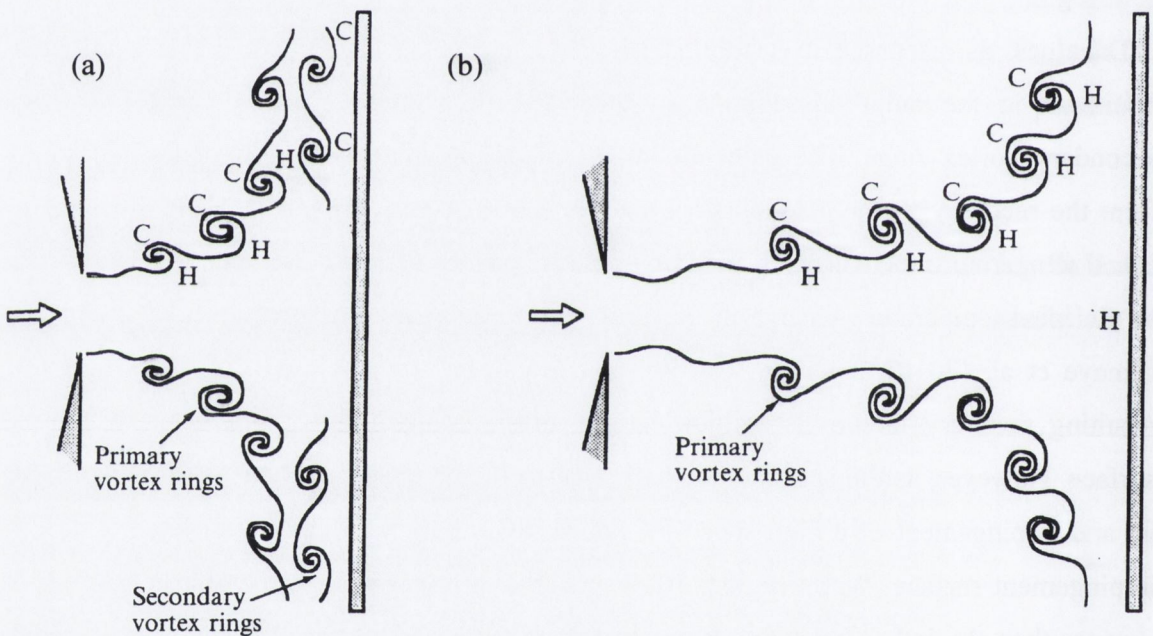
Figure 2.20, Schematic of the instantaneous total temperature separation in an impinging jet: (a) small H/D (b) large H/D. ' C' denotes cold and 'H' hot, Fox et al. (1993).

Goldstein et al. (1986) tested a 12.7 mm diameter jet with H/D varying from 2 to 12 and Re ranging from 64000 to 124000. They found the recovery factor to be independent of Re but to vary significantly with H/D. At the stagnation point (r/D=0) they reported a recovery factor close to unity for H/D = 2. As H/D is increased the recovery factor was found to increase up to a maximum at H/D of 8, after which the recovery factor levels off. Some of the recovery distributions studied by Goldstein et al. (1986) are shown in figure 2.21. They also noticed an off centre minimum in the recovery factor for H/D = 2. The recovery factor

at this minimum increases towards unity with increasing values of H/D and for H/D greater than 4 this minimum disappears. This can be explained by the disappearance of the secondary vortices at increasing H/D values as discussed at the end of section 2.4.1.
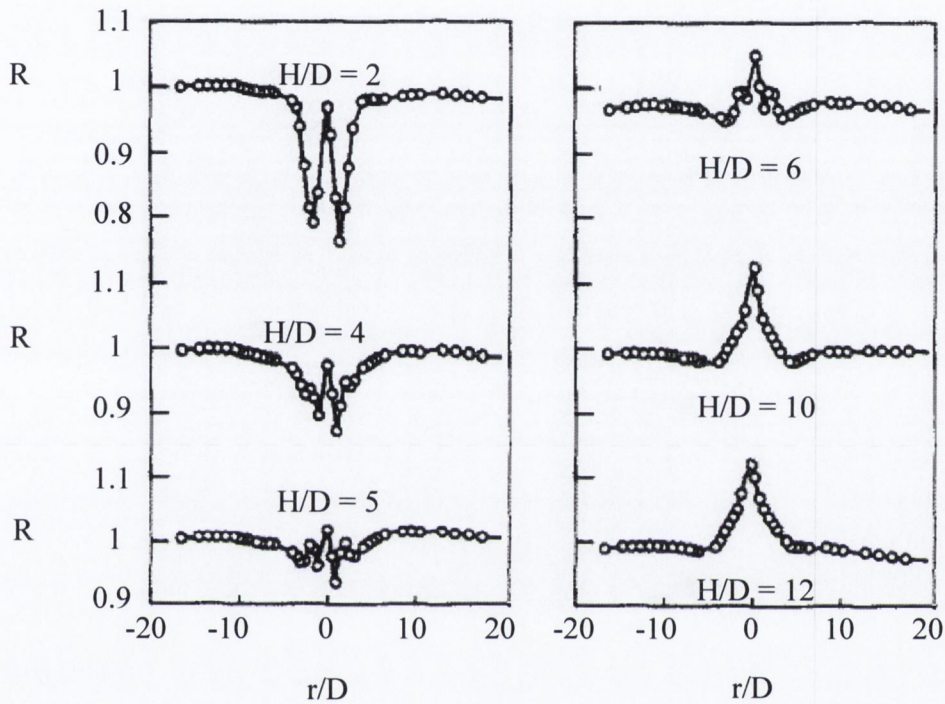
Figure 2.21, Recovery factor versus r/D for a single air jet: D=12.7 mm and Re from 64000 to 124000, Goldstein et al. (1986).

Meola and Carlomagno (2004) studied the effect of Mach number on the adiabatic wall temperature distribution from a 10 mm diameter jet. At relatively low Mach numbers adiabatic wall temperature distribution would be expected to be close to the initial total temperature of the jet over the entirety of the impingement surface. However, their findings show Mach numbers as low as 0.07 to have a significant effect on the $T_{a,w}$ distribution. At greater values of M they found the adiabatic wall temperature distribution to consist of a central peak surrounded by a single minimum or double minima depending on the magnitude of M, figure 2.22. At a Mach number of 0.3 a single minimum appears at approximately 1.2D from the stagnation point while at a M = 0.71 two minima at present at 0.9D and 2.2D. The minimum at 1.2D can be explained by the occurrence of flow

separation in the jet boundary layer, on the impingement surface, as described in section 2.4.1. Meola and Carlomagno (2004) noted that the flow reattaches at about 2D from the jet's center resulting in a local temperature increase, which is followed, in the wall jet region, by a decrease towards the ambient temperature. As the Mach number is increased the vortex rings strengthen, which results in increased recovery and entrainment effects.
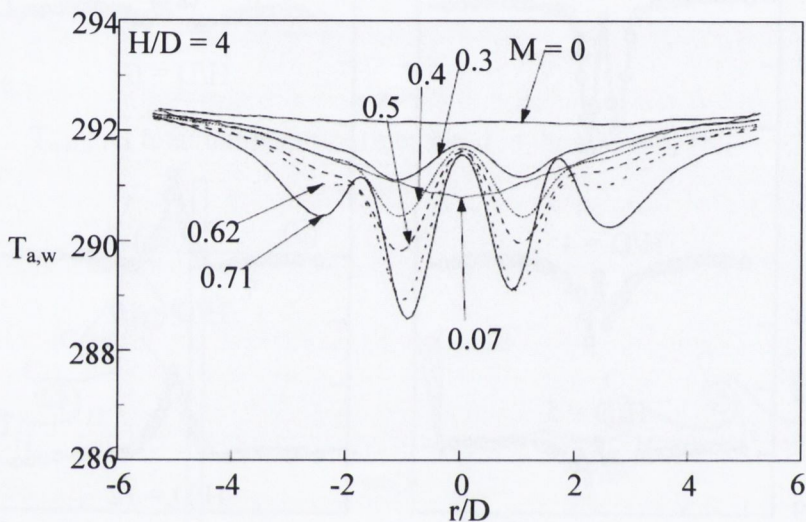
Figure 2.22, Adiabatic wall temperatures versus non-dimensional radial distance from the stagnation point for various subsonic Mach numbers. Tests were carried out on a truncated cone 10 mm diameter jet placed 4 jet diameters above the impingement surface, Meola and Carlomagno (2004).

At M = 0.71, break up of the primary vortex into two vortices results in the wall-jet entrainment of warmer ambient air. As a consequence, discrete minima form over circumferences centered at approximately 0.9 and 2.2 jet diameters. The need to account for Mach number effects, along with Reynolds number, is discussed in the next section. As part of their investigation they also varied H/D for a fixed Mach number of 0.4. It was found that for H/D < 5 the minimum temperature at 1.2D is not completely developed but takes the shape of a semicircle, figure 2.23. This shape is transformed into an annulus for H/D = 5 and breaks up into three structures because of flow instability at H/D = 6.
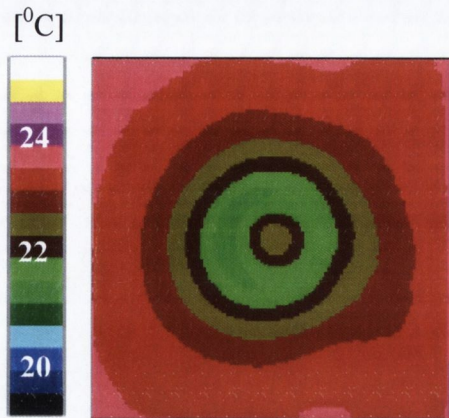
Figure 2.23, $T_{a,w}$ for D = 5 mm, M = 0.4 and H/D = 4, Meola and Carlomagno (2004).

Few studies exist that report recovery factors for jet arrays. Goldstein and Seol (1991) performed a study on a confined row of 6.35 mm diameter air jets with two side walls. The study was carried out for a Reynolds number of 40000, H/D values varying from 2D to 8D and two S/D values were studied. A row of 4 jets was used for the S/D = 8 test and 8 jets for the S/D = 4 test. From figure 2.24 one can see that the R distributions for S/D = 8 are broadly similar to the R distributions for the single jet in figure 2.21. Recovery values less than one are seen for both cases at low H/D and as H/D increases so do the local values of R. The increase of R with H/D is initially greater for the array jets than for the single jet. The R distributions for the array jets tend towards unity at the midway point between adjacent jets (r/D = 4) for S/D = 8 which resembles the single jet distribution. For the row of jets with S/D = 4 and H/D of both 2 and 4 the recovery values halfway between stagnation points (r/D = 2) show similar magnitude to the values at the stagnation points. These secondary maxima in the recovery are attributed to the collision of the wall jets from adjacent jets and the creation of a stagnation region. As H/D is increased, the local maximum at the collision region transforms to a local minimum.
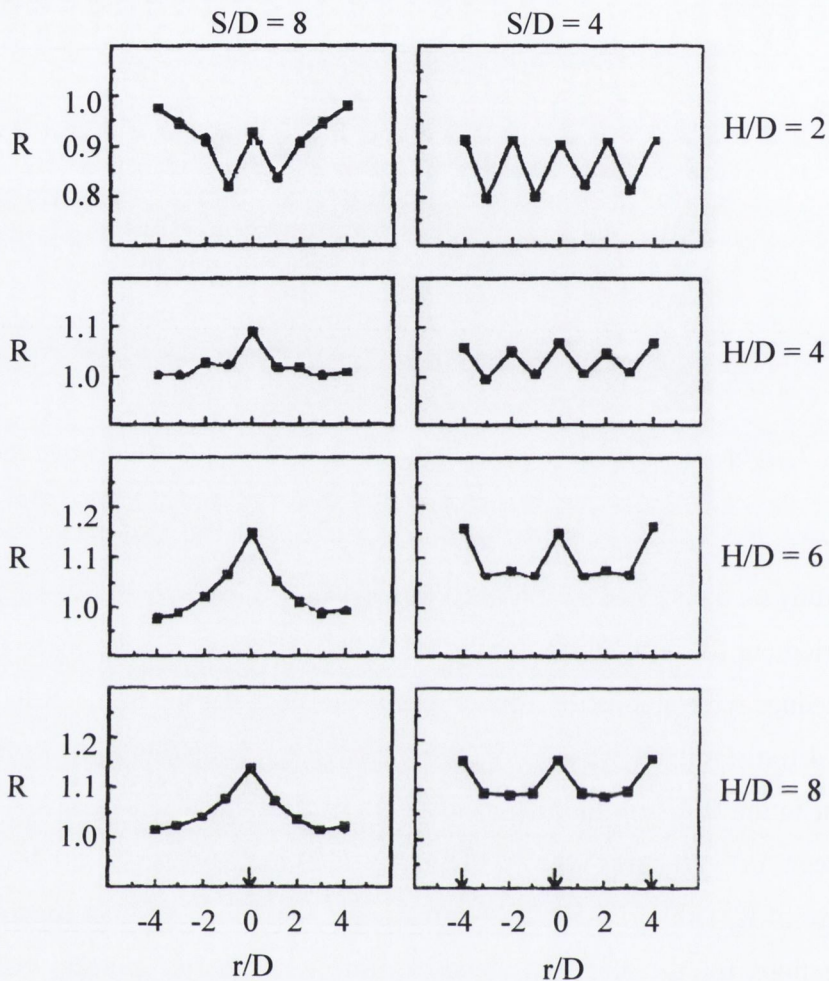
Figure 2.24, Recovery factor distributions for a row of jets, D = 6.35 mm and Re = 40000, Goldstein and Seol (1991). The arrows above the labeled x-axis represent the centre of the jets.

Other researchers, such as Goodro et al. (2007), have defined the heat transfer coefficient using $T_{a,w}$ as the reference temperature. However, they do not present or comment on recovery factor or adiabatic wall temperature distribution in their findings. Knowledge of the adiabatic temperature distribution is useful as it contains information that is lost when the heat transfer coefficient or Nusselt number is calculated. Thus, for the case of a forced convection problem involving a heated plate with a uniform wall flux boundary condition, q'', that is cooled by a fluid with reference temperature of T_∞, the shape of the heat transfer coefficient is determined by the heated wall temperature, $T_{h,w}$, as q'' and T_∞ are constants. In such a case, low values of $T_{h,w}$ occurs in areas of effective cooling and are represented

by high values of Nu and vice versa. However, when $T_{a,w}$ is used as the reference temperature this relationship between $T_{h,w}$ and Nu does not always apply. Figure 2.25 (a) shows the temperature distributions from an underexpanded 12.7 mm diameter single jet impinging onto a heated and an unheated plate, Rahimi et al. (2003). The two temperature distributions are quite similar in shape close to the stagnation region, showing a local maximum in temperature at r/D = 0. However the locally high value of $T_{h,w}$ at r/D = 0 corresponds to a maximum value of Nu, figure 2.25 (b), as $T_{a,w}$ has been used as the reference temperature for estimating Nusselt number. Therefore the Nusselt number alone does not provide enough information to understand the cooling effects of high Mach number jets. Knowledge of the surface temperature distribution and the associated lateral conduction may be of greater value than Nusselt number for many practical applications. Due to the lack of information available in the literature on these topics this study explores these topics through a micro impinging jet array study.
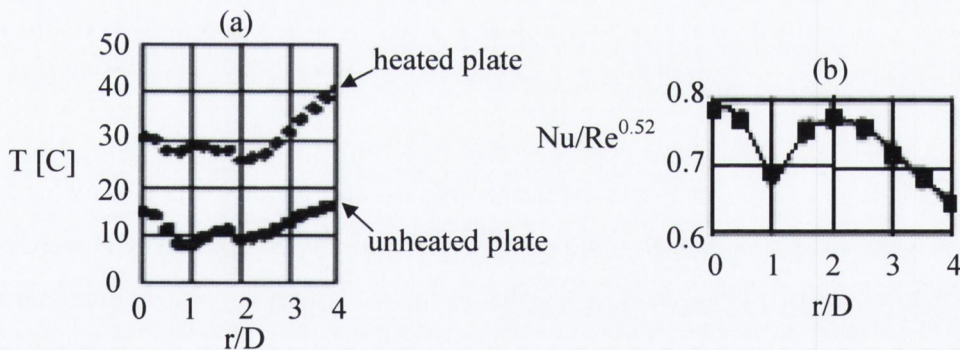
Figure 2.25, (a) Surface temperature and (b) Heat transfer distributions for a 12.7 mm diameter convergent jet at H/D=3 and $P_{up\ stream\ of\ nozzle}/P_{ambient}$ = 3.04, Rahimi et al. (2003).

It is important to note that the standard definition of the recovery factor is given in equation 2.8 and that the adiabatic wall temperature $T_{a,w}$ is used to define R. However, this study focuses on the conjugate heat transfer problem and the impinging surface, a thin stainless steel foil, is subjected to lateral conduction. Because the temperature distributions recorded in this study are recorded from a conducting surface and not a zero heat flux surface the resulting temperature distributions are referred to as unheated wall temperature distributions, $T_{u,w}$ and not $T_{a,w}$. So for this investigation the definition of the recovery factor

has been modified, as $T_{u,w}$ is used in replace of $T_{a,w}$ in the definition of R in equation 2.8. The significance of lateral conduction for R is that it decreases the absolute values of maxima and minima in the recovery factor distributions as heat is conducted from warm regions to cool regions. A definition of the modified recovery factor is given in section 4.2.

2.7 SCALING

Garimella and Rice (1995) noted that the effect of nozzle diameter on heat transfer is not captured by Nusselt number non-dimensionalisation. Beskok and Karniadakis (1994) showed that the flow in some micro-scaled geometries does not behave according to the continuum hypothesis but rather exhibits characteristics associated with a slip flow regime. This was reinforced through evaluation of the Knudsen number.

$$Kn = \frac{\lambda}{L_{char}} \qquad (2.9)$$

where,

λ, mean free path [m] (approximately 10^{-7} m for air at standard conditions)

L_{char}, characteristic length [m]

For most geometries $Kn < 0.01$ implies that the continuum hypothesis is valid whereas the slip flow regime is characterised by $0.01 \leq Kn < 0.1$. Narasimha et al. (1973) were one of the first research teams to acknowledge that the traditional use of the nozzle diameter as the reference scaling for wall-jet flows was not always appropriate. They proposed a scaling length that took into consideration the flow evolution. Pence et al. (2003) proposed the use of the viscous boundary layer thickness as possibly a more appropriate length scale, as this layer can be considerably smaller than the jet diameter. They showed for their tests with air that the inner region of the velocity profile is of the order of 0.1 times the jet radius. For the present investigation the 610 μm diameter jet corresponds to a Knudsen number of 0.164×10^{-3}, which is significantly below the level at which the onset of the slip flow region commences. Thus, the fluid is treated as a continuous medium and described in terms of the macroscopic variables: velocity, density, pressure, and temperature.

2.8 CONJUGATE HEAT TRANSFER

Many heat transfer studies have been performed using a heated thin foil to generate a constant heat flux boundary condition. In such a study the magnitude of lateral conduction within the foil is generally assumed to be negligible as the foil is sufficiently thin. The current investigation looks at recovery effects of jets impinging onto a thin foil surface that is at ambient temperature prior to impingement. With jet impingement, temperature gradients are developed on the foil due to recovery, as described in section 2.6. Jets of the order of 610 μm in diameter are studied in this investigation and the resulting temperature gradients associated with impingement of these jets vary considerably over a small area of the foil. These variations in temperature gradients with respect to distance are sufficiently large to induce a considerable amount of lateral conduction within the foil. Conduction occurs through the transfer of thermal energy between neighbouring molecules in the foil. The lateral conduction acts to equalise temperature differences by transferring heat from warm regions of the foil to cooler regions. Conduction can play a major role in the cooling of localised hot spots as conduction effects act to spread out the heat generated at a hot spot. Incorporating heat flux removal due to lateral conduction into a cooling solution allows one to remove heat from a small hot spot by cooling a large area surrounding the hot spot, which is most advantageous. This study investigates the amount of heat flux due to lateral conduction, q''_{lc}, that can be removed from a region as a result of jet impingement. The fact that both convection and conduction occur simultaneously in the current investigation makes the current study one of conjugate heat transfer. Jahangeer et al. (2007) described conjugate heat transfer as a process of heat transfer that involves interaction between conduction within a solid body and convection from the solid surface to a fluid moving over the solid surface. Wolfersdorf (2007) stated that the effects of lateral conduction due to adiabatic wall temperature variations can be more significant than due to variations in the heat transfer distribution. Sarghini and Ruocco (2004) notes that most of the large body of impinging jet heat transfer literature focuses on the fluid flow region and there is a lack of knowledge about the conjugate mechanisms that drive heat transfer. They investigated the conjugate heat transfer using a cooling jet and in their findings they identified 'the conjugate effect' as the competitive effect of conduction over convection. The dominant presence of concurrent substrate conduction caused localised heat transfer

reversal (the heat flux is directed from the flow to the plate). In the present study, lateral conduction distributions corresponding to the modified recovery factor distributions are presented and discussed. One recent study that presented such data in a similar manner is that carried out by Stafford et al. (2009), figure 2.26. They studied a fan, rather than a jet, cooling a thin foil. Their results give an indication of the magnitudes of lateral conduction associated with surface temperature variations on a thin foil. In figure 2.26 (a) is a temperature distribution consisting of both relatively warm regions (red) and relatively cool regions (blue). Lateral conduction effects result in heat conducting from warm regions to cool regions. Figure 2.26 (b) shows the corresponding heat flux due to lateral conduction distribution. On the q_{lc}'' distribution both negative regions (red) and positive regions (blue) exist. The negative q_{lc}'' regions correspond to warm temperature regions, these regions have negative q_{lc}'' as heat is conducted from these warm regions to cooler regions. Similarly cool temperature regions correspond to positive q_{lc}'' regions as heat is conducted into these cool regions. This investigation performs a similar study but the scale of the micro jet study is smaller.
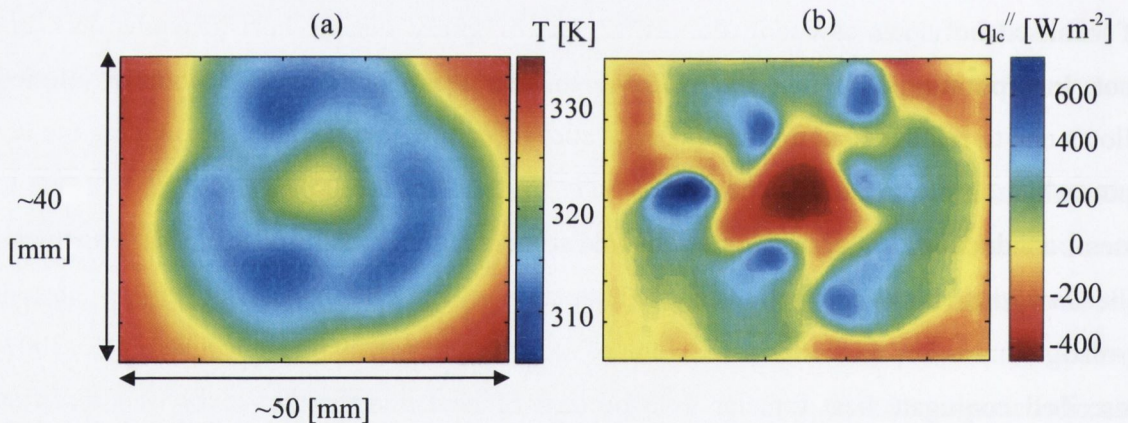
Figure 2.26, (a) Temperature and (b) Lateral conduction distributions resulting from a 24 mm axial fan cooling a 41.7 μm thick foil, Stafford et al. (2009).

2.9 CONCLUDING REMARKS

Jet impingement fluid flow and heat transfer has been extensively researched at large scale. However studies into the effect of varying nozzle diameter have shown that correlations developed for large diameter jets over predict Nusselt numbers for smaller diameter jets and this would suggest that further research is required into the area of micro impinging jets. Based on the findings of Garimella and Rice (1995) and San et al. (1997), it was

decided that the current investigation would focus on jets of diameter less than 6 mm but as very small scale jets have been investigated far less thoroughly it was decided to concentrate on jets of less than 1 mm in diameter. Another constraint in choosing the jet diameter was the camera's spatial resolution as it was important that the resolution of the camera would facilitate accurate determination of lateral conduction in the test foil, resulting from the jet induced temperature distribution. The 610 μm diameter chosen is within the range appropriate to the thermal imaging camera and lens available.

A number of studies have been carried out into the heat transfer resulting from an array of micro impinging jets but most research has focused on area averaged heat transfer from numerous jets, Whelan and Robinson (2009) and Robinson and Schnitzler (2007). The closest comparable study to the current study was one carried out by Garimella and Schroeder (2001), who studied the local heat transfer from 1.59 mm diameter jet arrays, but their study was performed for low Mach number jets whereas the current study investigates large Mach number jets. This study looks at the effects of varying jet population and inter-jet spacing, as well as exploring the influence of Reynolds number and jet to plate spacing. The results are presented in the form of recovery factor as there seems to be a lack of knowledge available on surface recovery distribution resulting from arrays of jets. As an integral part of this investigation, the contribution of lateral conduction in the conjugate heat transfer process for impinging jets is examined, as this topic seems to have received little attention to date.

This study explores also the effect of varying the level of confinement on a 910 μm diameter jet. Baydar and Ozmen (2006) studied the effects of confinement on a 25 mm diameter jet and found the stagnation point Nusselt number to be mostly independent of the degree of confinement; this is in agreement with the results of Behnia et al. (1999). However San et al. (1997), who investigated 3 mm to 6 mm diameter jets, found that increasing the surface heating width of the impingement plate, W, results in lower stagnation Nusselt numbers and attributed this phenomenon to flow recirculation and mixing. This finding suggests that confinement effects may be more pronounced for micro jets and therefore this effect is investigated here.

3 EXPERIMENTAL RIG AND TEST PROCEDURES

The objective of this investigation is to gain a fundamental understanding of compressibility effects and associated conjugate heat transfer of micro impinging jets. Several experimental parameters influence these phenomena and five have been selected in this study; the jet velocity, the distance of the jet exit from the impingement surface, the interjet spacing in an array of jets, the number of jets and the level of confinement of the jet. This chapter gives an overview of the experimental rig and the measurement instrumentation used to gain insight into the effect of the above parameters.

3.1 EXPERIMENTAL RIG

This section contains a description of the main experimental rig elements. Initially an experimental rig and test procedure similar to that used by Patil and Narayanan (2005) was employed but numerous modifications of the rig were implemented to resolve issues as discussed hereafter. A schematic of the test section is shown in figure 3.1.

Air from a compressor entered a mass flow controller that dictates the air flow rate; it then entered a plenum that stagnated the fluid and both the temperature and pressure of the fluid were measured at this point. The air was then passed from the plenum through a nozzle and the exiting jet flow impinged perpendicularly onto an impingement surface made of stainless steel foil. The high Mach number of the jet flow created a non-uniform surface temperature distribution on the foil. Evaluation of the Biot number, section 3.1.3, confirms that measuring the temperature distribution on the bottom surface of the foil gives a good indication of the temperature distribution on the top surface of the foil as the temperature difference across the 25 μm thick foil was negligible. The base of the foil was painted with a thin layer of matt black paint to increase emissivity, and it was then viewed by an infra red camera. In the current investigation the temperature distributions recorded by the IR camera explore solely the effects of temperature recovery. However, it is planned to continue this research with an investigation of convective heat transfer coefficients for

micro impinging jets and for this the foil will be ohmically heated. To facilitate this, the foil is connected at either ends to copper bus bars which are in turn connected to a power supply.
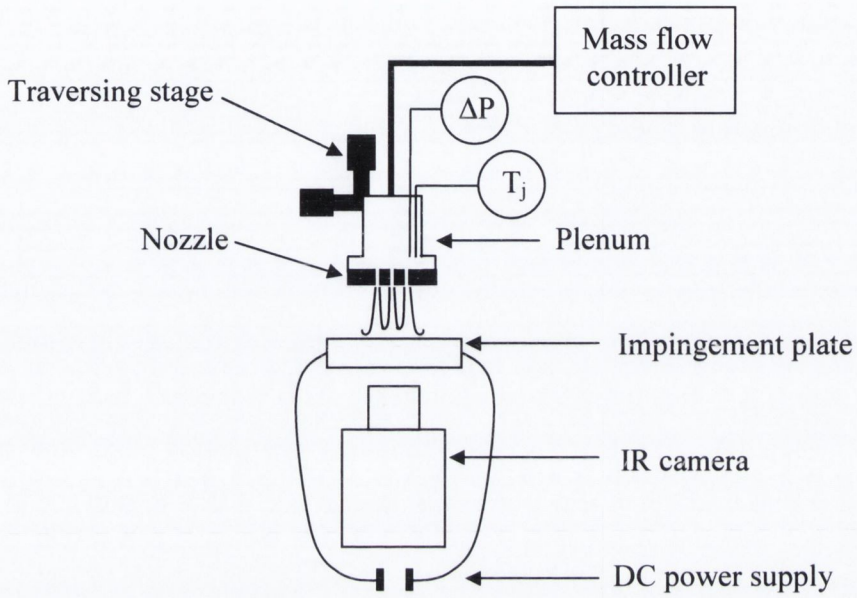
Figure 3.1, Overall impingement test set-up.
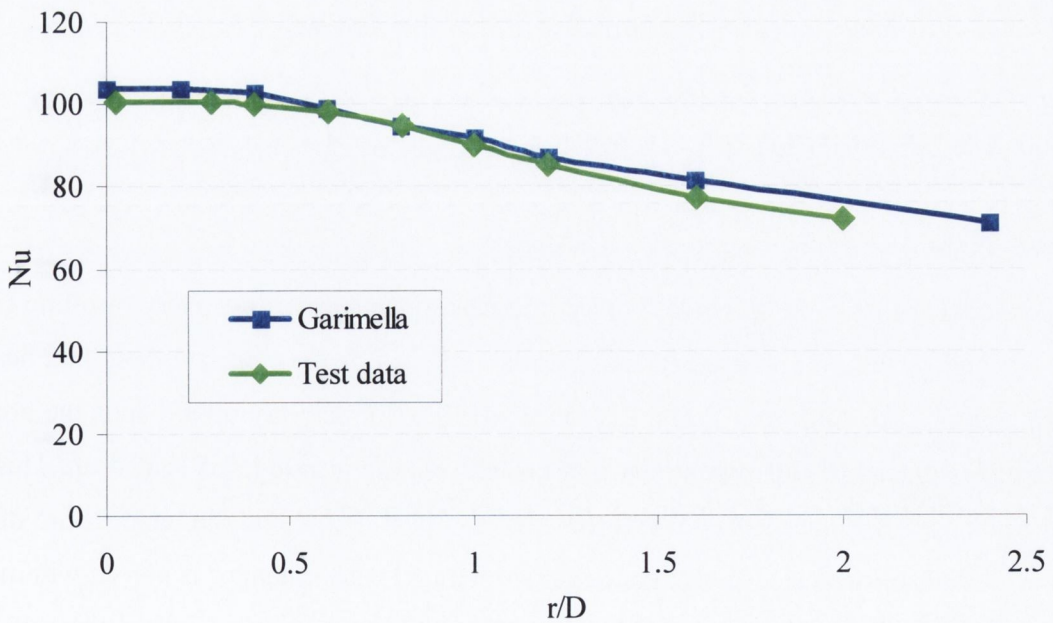
Figure 3.2, Comparison of measured Nusselt numbers with findings of Garimella and

Schroeder (2001).

- 43 -

In the first stage of this research, a study was carried out to validate the experimental setup. Test data were compared with results presented in work carried out by Garimella and Schroeder (2001). They used a confined jet and presented local heat transfer values. To perform an accurate comparison it was important that parameters affecting the heat transfer coefficient were replicated, Table 3.1. (The parameters given in Table 3.1 were only used for the initial comparative study; the thesis parameters are different.) Further information on the comparative investigation can be found in Lupton et al. (2007a). Local Nusselt number distributions shown in figure 3.2 illustrate that the test data are slightly lower than Garimella's data which is consistent with findings from the literature as the diameter of the test jet is slightly smaller than that used by Garimella. Although this validation study related to convective heat transfer measurement with a heated foil, it does provide preliminary validation of the Reynolds number calculation and the temperature measurement set-up, both important factors for the current adiabatic study.

Table 3.1, Test parameters and parameters used by Garimella and Schroeder (2001).

	Test data	Garimella and Schroeder (2001)
H/D	4	4
Re	20 000	20 000
D [mm]	3	3.18
L/D	1	1
W [mm]	20	21.2

3.1.1 NOZZLE

As previously mentioned this investigation focuses on temperature recovery resulting from jets impinging onto an unheated surface but the test rig was developed for use in a heated configuration also. An initial study, Lupton et al. (2007b), demonstrated that as the nozzle plenum was placed in close proximity to a heated foil, the nozzle itself heated up. This, in turn, heats up the plenum and this has the adverse effect of causing the temperature of the pre-impact jet to increase. To eliminate this problem a heat exchanger is placed within the structure of the nozzle. Two types of nozzles were used in the current investigation, one for the multiple jet investigation and one for the confinement study. The nozzles used for the multiple jet investigation were made from perspex while the confinement nozzle is a more

complex system but with a confinement surface which is quite similar to the multi-jet nozzles and consisted of a 9.5 mm thick sheet of perspex with multiple cooling channels drilled into the perspex, as shown in figure 3.3. Most of the cooling channels shown in figure 3.3 are sealed but two remain unsealed in order to allow for ambient water to pass in and out of the cooling channels. Schematics of the nozzle designs are contained within Appendix A.

The nozzles used to study the multiple jets and the effects of interjet spacings are shown in figure 3.4. Different jet configurations as shown in figure 3.5 were drilled into the center of the nozzle plates. The through holes were 9.5 mm in length and 0.61 mm in diameter. The length of these nozzles was initially designed to be 20 jet diameters, as Incropera (1999) stated that a development length, L, greater than 20 jet diameters was necessary to ensure a fully developed flow. However, manufacturing constraints resulted in the actual test nozzles consisting of a development length of 15.5 jet diameters. This means that the jets tested may not be fully developed but it is expected that the jet's maximum velocity occurs
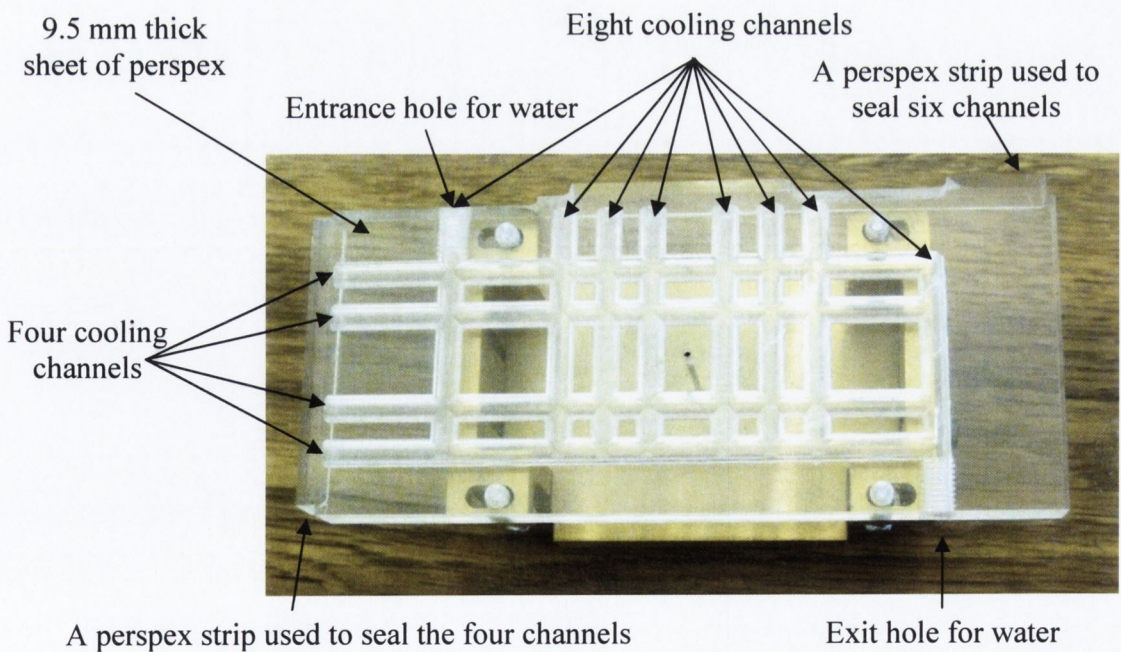
Figure 3.3, Cooling channels drilled into a sheet of perspex, for use as a confinement surface in the confinement study.

In the centre of the nozzle is a 3×3 square jet array (to the left is a view of this array under a microscope)

Water outlet

9.5 mm sheet of perspex

Water inlet

Threaded holes for fixation of plenum
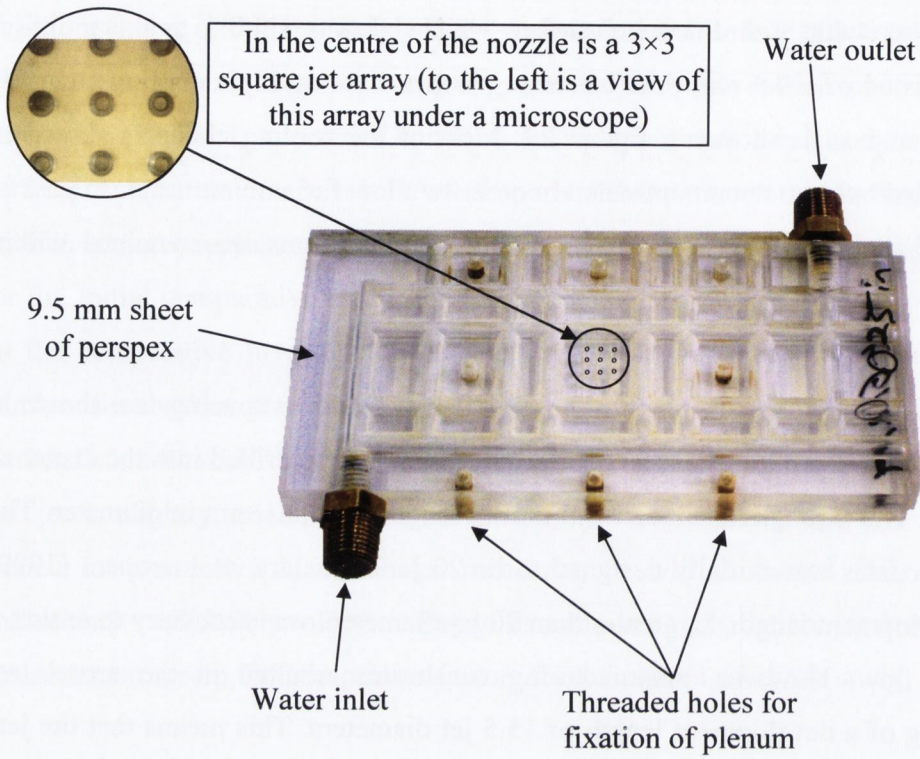
Figure 3.4, 3×3 square jet array nozzle arrangement with liquid cooling channels.

(a)　　　　　　(b)　　　　　　(c)
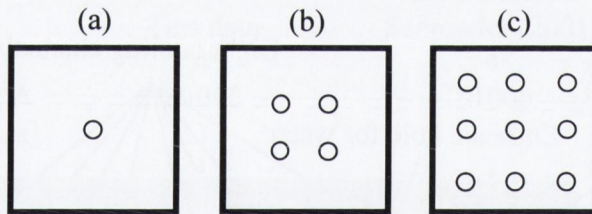
Figure 3.5, Nozzle configurations for (a) a single jet, (b) a 2×2 square jet array and (c) a 3×3 square jet array.

A through hole

9.5 mm thick perspex sheet

A chamfer in the perspex
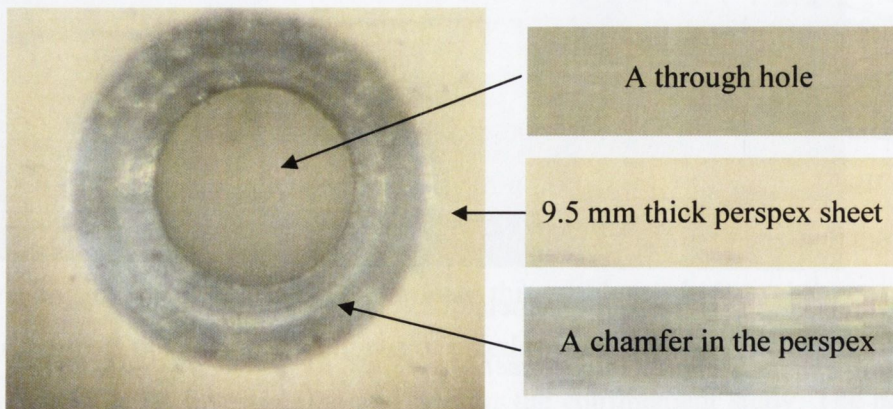
Figure 3.6, A magnified overhead view of a 610 μm diameter jet drilled into perspex that shows the chamfer caused by the initial wobble in the drill.

at the centre of the jet, as shown in figure 2.8 (a). Problems encountered with drilling micro holes for the jets in the perspex were initial wobble of the drill bit as it grips the perspex surface and also the wandering of the drill as it travels through the perspex. The initial wobble of the drill tool as it grips the perspex resulted in the creation of a nozzle chamfer on the exit of the nozzles, figure 3.6; however the nozzle inlets were square edged. Whelan and Robinson (2009), who examined submerged water jets, compared an array of jets with outlet chamfers to an array of jets with square edge exits. Their findings show that for the same pumping power, the introduction of a chamfer to the jet's outlet reduces heat transfer by approximately 8 % for their higher flow rates studied, figure 2.10. The effect of the wandering of the tool was most significant for an individual jet contained within the 3×3 jet array with the interjet spacing of 4 jet diameters. Using a microscope the offset angle of this jet was calculated to be approximately 0.42 degrees from top to bottom. Beitelmal et al. (2000) who studied the effects of inclination on the heat transfer between a flat surface and an impinging air jet found the maximum Nusselt number value in the impinging region to be proportional to $(1 + 0.365 \sin\theta)$, where $\theta = 90^0$ corresponded to a perpendicular impinging jet. Using this relationship, an offset angle of 0.42^0 shows insignificant effect on heat transfer when it is compared to a perpendicular jet; however, the recovery values induced by this particular jet were found to be somewhat lower than values presented for its neighbouring jets, as reported in chapter 5.

The nozzle used in the confinement study is illustrated in figure 3.7. It consists of five main parts; a needle, a horizontal brass plate, a pair of vertical guidance tracks, a height fixation screw and a perspex confinement plate. The vertical needle is used to produce a jet; it has a 0.91 mm internal diameter cylindrical hole and is 45 jet diameters in length. The needle is attached to a horizontal brass plate. The two vertical brass guidance tracks allow vertical motion of the horizontal brass surface and the needle. During testing the distance from the bottom of the confinement plate to the nozzle's exit, Z_{plate}, is varied in order to investigate the effects of confinement, figure 3.8. The height of the plate above the impingement surface was found by using spacers and then this height was fixed via tightening screws placed within the guidance track, figure 3.9. Data was collected for values of Z_{plate} equal to 0, 4 and 12 jet diameters.

Fixation screw used to fix
the height of the slider

Horizontal brass slider which
traverses in a vertical direction

Vertical brass
guidance track for
the slider

Impingement surface,
stainless steel foil

Perspex base plate which
acted as a confining surface

Syringe needle with a 0.91 mm internal
diameter used to produce a fully developed jet
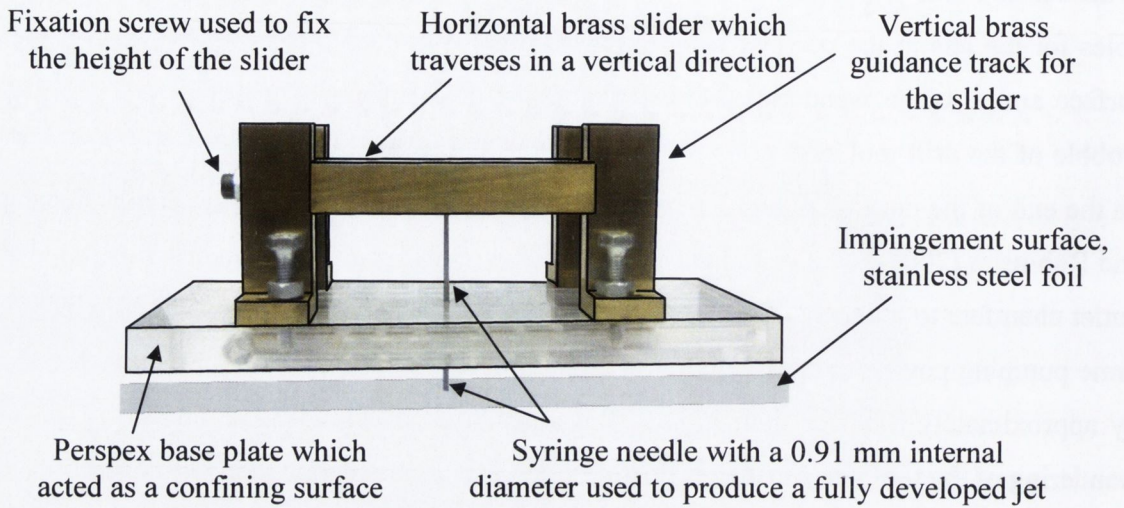
Figure 3.7, A front view of the nozzle used for the confinement study.

(a) <u>Confined jet configuration</u>

(b) <u>Unconfined jet configuration</u>

Slider positioned at an
elevated height relative to
the perspex plate

The base of the slider is
flush with the top of the
perspex plate

$Z_{plate} = 12D$

Base of the needle is flush with the base
of the perspex plate, $Z_{plate} = 0$

The needle protrudes from
the perspex plate
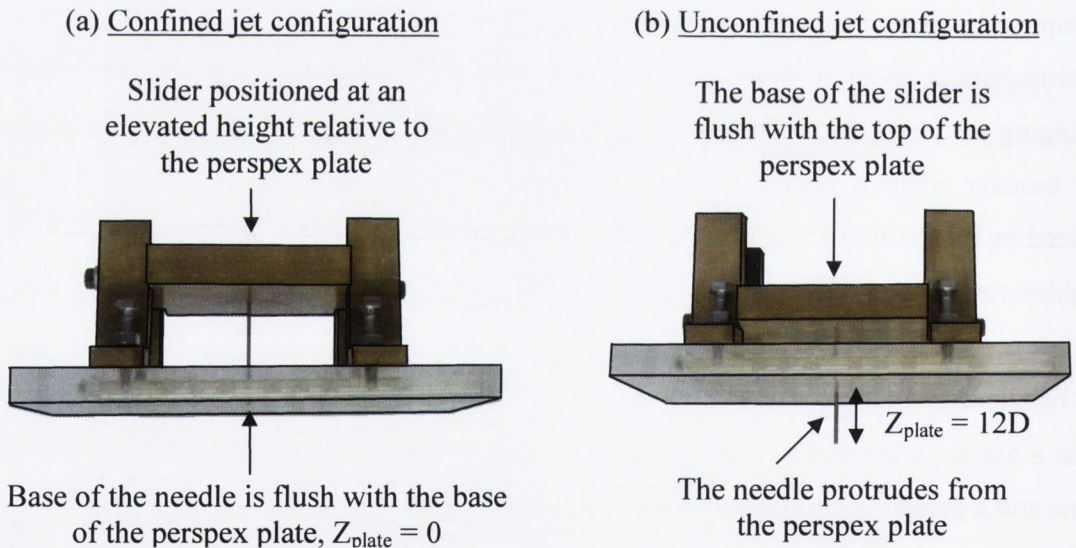
Figure 3.8, The confinement nozzle in both (a) fully confined and (b) unconfined positions.

Eight threaded holes for attaching a
plenum

Track

Slider

Mark from an o-ring used
to seal the slider plenum
interface air tight

Height fixation screw
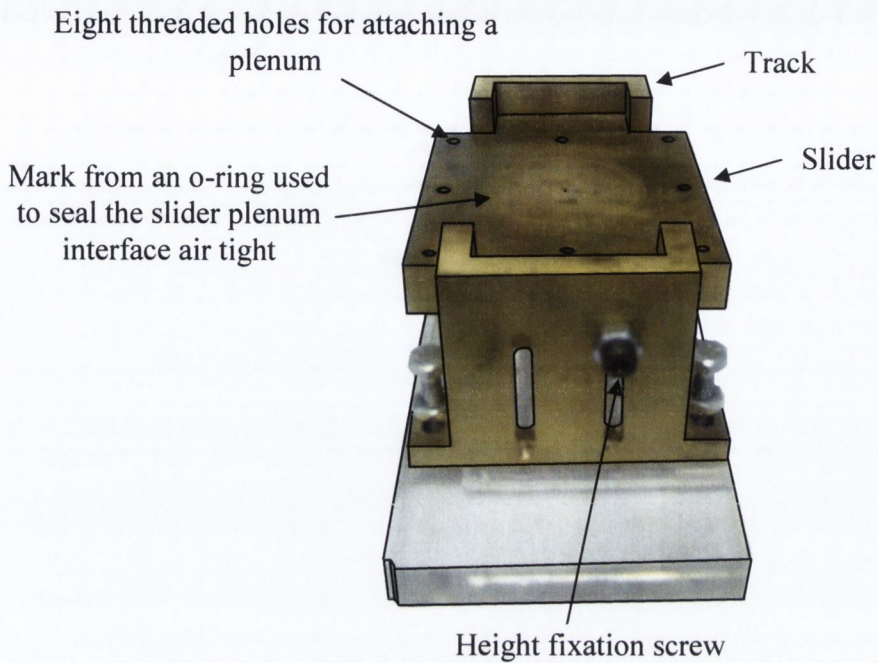
Figure 3.9, A side view of the confinement nozzle.

3.1.2 PLENUM

The plenum in figure 3.10 was designed to supply air to the nozzles, as mentioned in the previous section. The plenum contained 8 through holes. During testing, screws were placed through these 8 holes and tightened into 8 threaded holes that existed at the top of each nozzle plate. The tightening of these screws ensured that an o-ring, placed in a groove at the base of the plenum (figure 3.11) was compressed. Thus an air tight seal was formed in the plenum-nozzle interface. This assured that fluid only exited from the plenum through the holes used to produce the jets. The inner wall of the plenum is 15 mm in diameter as to stagnate the fluid flow and to provide a uniform pressure across the plenum. The largest jet used in this study was the 0.91 mm diameter jet used in the confinement study. As such, the plenum was designed to be 35 times the confinement jet diameter; this is a larger ratio than that used by Beitelmal et al. (2000) who tested a slot jet using a plenum of width 10 times greater than that of the slot jet. Inside the plenum are two measuring probes, as depicted in figure 3.11; (i) a 1.5 mm diameter type-K thermocouple that was connected to an OMEGA CL3512A thermometer and (ii) a pressure tap that was connected to a Digitron 2083P, differential manometer. Measurements from the pressure tap are used to monitor the air tightness of the seal. Thus, when a nozzle is fixed initially to the plenum the system is

checked for leaks using a leak detector. After it has been confirmed that the system is impermeable, the pressures corresponding to the test flow rates are recorded and during testing the pressure is monitored to ensure no leaks develop within the system. The overall plenum is connected to a traversing stage with 3 degrees of freedom, as shown in figure 3.12.
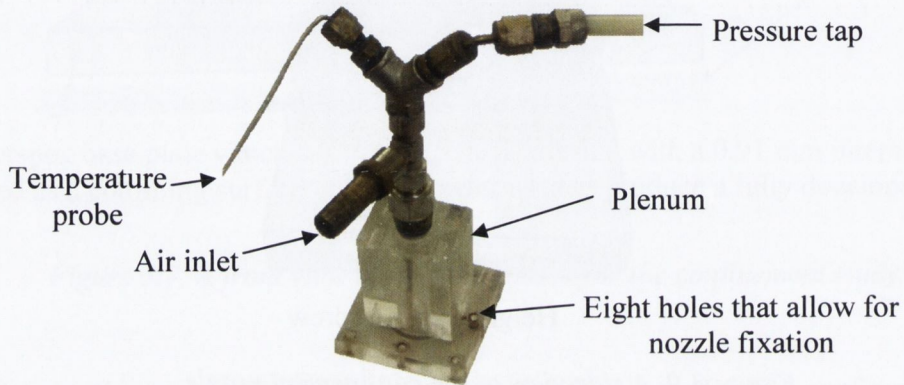
Figure 3.10, The test plenum.
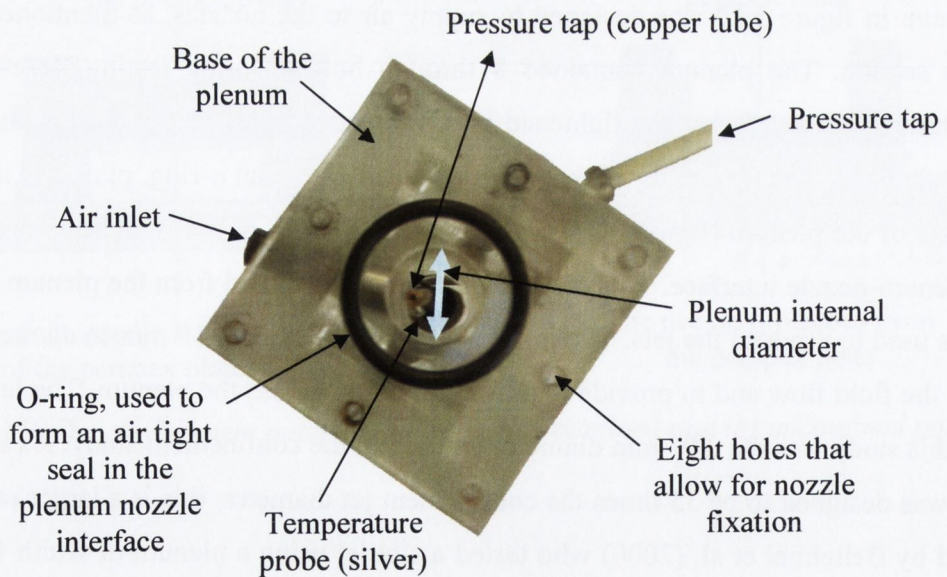
Figure 3.11, The base of the plenum.

3.1.3 TEST SECTION

Once the jets are positioned satisfactorily, i.e. their impingement is in the field of vision of the infrared camera, then a micrometer that was part of a Parker multi-axis 4000 series linear positioner is used to move the plenum in a direction perpendicular to the impingement surface to desired values of nozzle to impingement surface spacings. The Parker positioner is specified with an accuracy of 2 μm per 25 mm and the maximum distance travelled was 4.56 mm. The smallest distance between the nozzle and the impinging surface was 1 jet diameter or 610μm. It was difficult to accurately zero the height of the nozzle onto the impingement surface so the initial height of the jet relative to the impingement surface was calibrated using visual photography. A Cannon IUXS 70 was used to record a picture of the nozzle above the impinging surface at an unknown height 'X', figure 3.13 (a); 'X' was approximately 5 mm. Then, using a micrometer on the traversing stage, the nozzle was accurately elevated 5 mm higher such that the new height of the nozzle was X + 5 mm, figure 3.13 (b). Comparing the two figures allowed for the accurate calculation of X. Once X was known it was possible to accurately adjust the nozzle to impingement spacing.
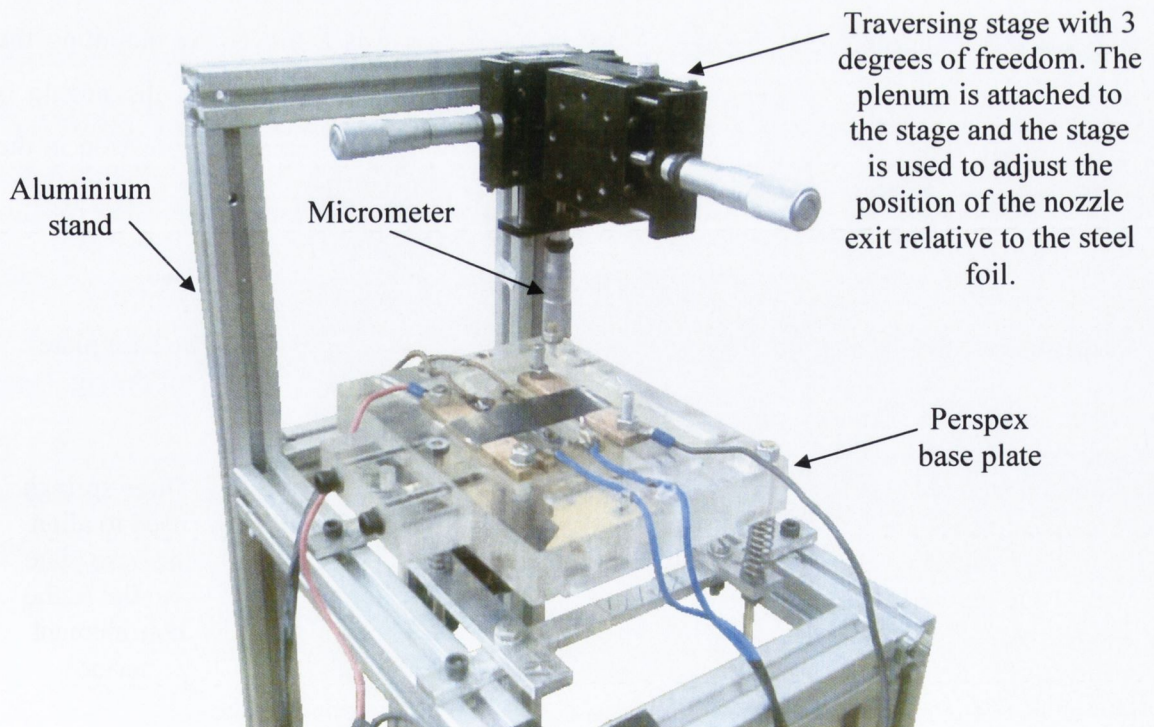
Figure 3.12, The traversing stage in situ.

A red object was placed flush against the rear
side of the nozzle as to focus the camera

The Base of
the perspex
nozzle is
located
between the
two
horizontal
black lines
(numerous
reflections
are visible on
the base)

Side of the
perspex nozzle
(a strip of black
tape was placed
here to make it
easier to
distinguish
between the side
and the base of
the nozzle)

Impingement surface (stainless
steel foil)

Nozzle to impingement
surface distance

Figure 3.13, Calibration of the nozzle to impingement surface spacing.

Prior to carrying out the above procedure of calibrating the nozzle to impingement surface
distance, it was important to ensure that both the confinement surface of the nozzle and the
stainless steel surface were parallel to one another. This was achieved by mounting the
perspex base plate on 3 compressed springs, figure 3.14. Before testing, the nozzle is
positioned in proximity to the impingement surface and the degree of compression in the

Brass rod located
at the centre of
the spring. The
rod was threaded
into the perspex
above and
gripped with a
nut from below

The base plate
of the rig

Three springs
used to align
the base plate
parallel to the
confinement
surface

A fixation nut grips the base of the rod and determines the
extent of compression in the spring above it
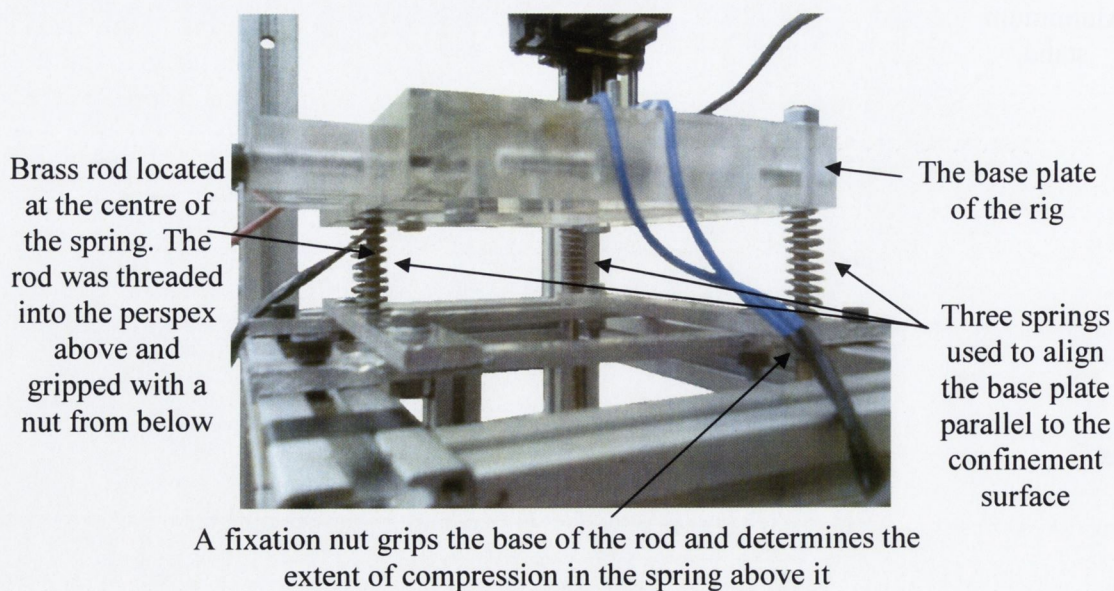
Figure 3.14, The system for adjusting the level of the impingement surface.

three springs is altered by rotating a nut placed beneath each spring. The manipulation of the compression in the springs allows for the parallel alignment of the impingement surface relative to the nozzle.

The impingement surface consisted of a 25 μm thick and 80 mm by 28 mm stainless steel foil (AISI 321 - Fe/Cr18/Ni9/Ti) which may be connected to a Lambda DC power supply capable of supplying 200A at 6V, figure 3.15. As described at the beginning of this chapter, some heated foil tests were carried out in a validation of the overall experimental set-up. When the test plate is heated, the voltage drop across the foil was much less than the voltage supplied by the power supply due to losses in the system such as electrical contact resistance and losses in the power leads. The potential difference across the foil was accurately measured by cutting voltage taps from the test foil, Pan and Webb (1995). The voltage tabs were then soldered onto the blue and brown wires illustrated in figure 3.15. Soldering the wires to the stainless steel was achieved through the use of soldering flux. In the early stages of the project mounting of the impingement surface was achieved by clamping the steel foil with a pair of copper bus bars at each end. Unfortunately this led to non uniform spreading of the current from the bus bars to the foil and the upper bus bar also introduced a level of lateral confinement to the outwash flow. To resolve both issues the 80 mm by 28 mm foil was bonded to two individual copper bus bars using an electrically conductive silver loaded epoxy. Another problem encountered with initial rig designs was drumming of the foil. To overcome the problem a tensioning mechanism was developed for the foil. One of the foil's bus bars was fixed to a rigid stand whilst the other was mounted to a section of the stand which could traverse linearly along a pair of guidance rods; this can be seen in figure 3.15 and more clearly in figure 3.16. Tension was generated in the foil by compressing the springs, located along the guidance rod, for the duration of time it took to cure the foil to the bus bars. Once the foil was cured the springs were released and the springs ensured that the foil remained continuously taut, removing the problem associated with drumming.
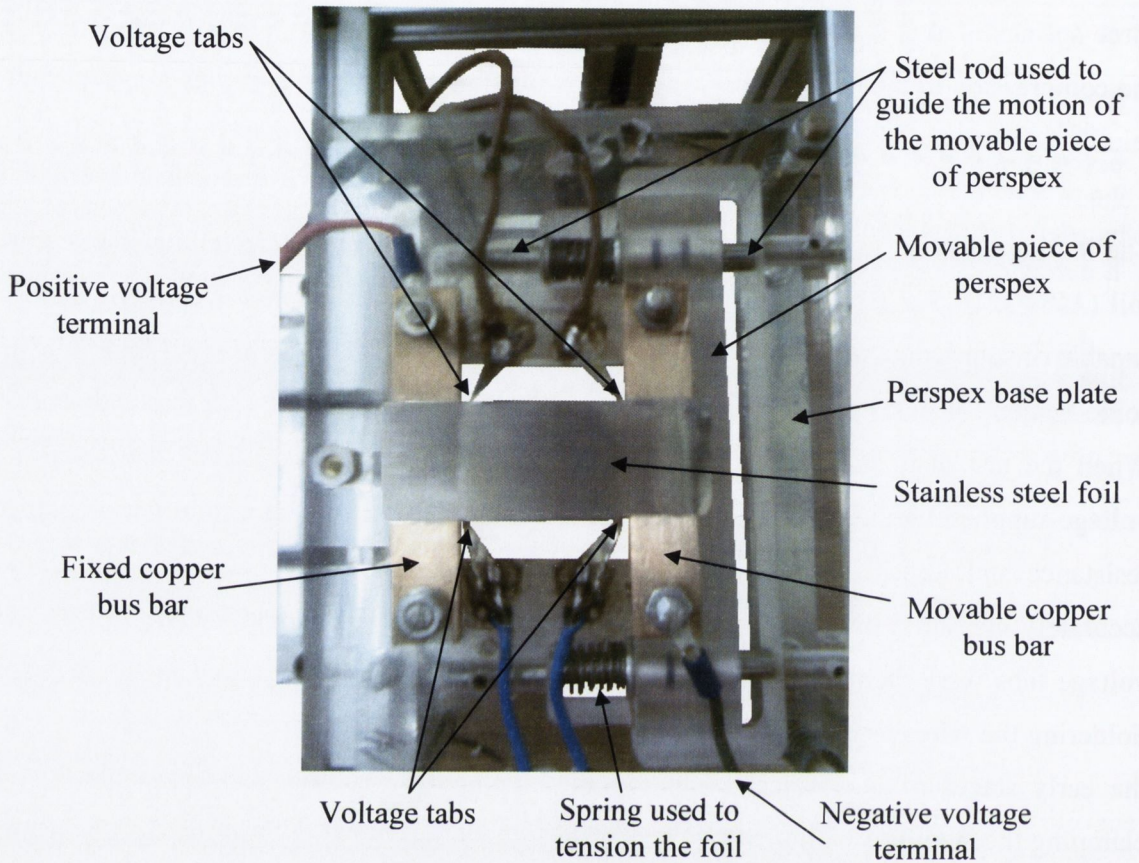
Figure 3.15, Plan view of the impingement surface.
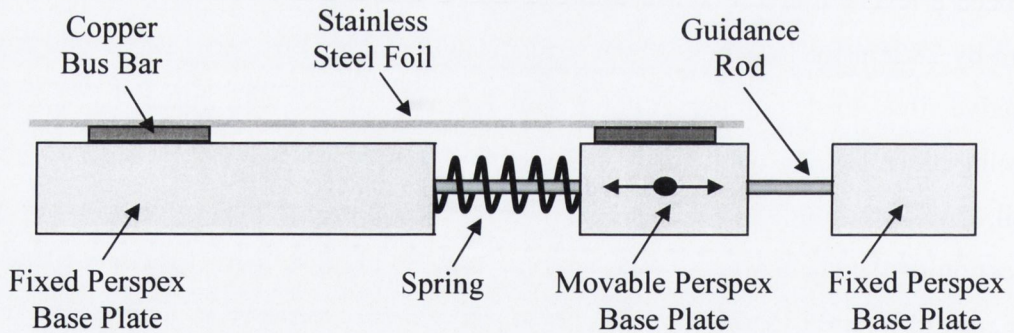
Figure 3.16, The tensioning system used to maintain a taut foil.

During testing the plenum and nozzle were placed above the foil and the jets impinged onto the upper surface of the foil. The thermal imaging camera was placed below the foil as the temperature at the top of the foil was equal to that at the base of the foil. This assumption is correct when the corresponding Biot number is less than 0.01, Astarita and Cardone (2000).

Biot number, $Bi = \dfrac{h \times t_{foil}}{k_{foil}}$, (3.1)

where,

h, heat transfer coefficient, [W m^{-2} K^{-1}]

t_{foil}, thickness of the foil, $(25 \times 10^{-6}$ m)

k_{foil}, conductivity of the foil, (16.3 W m^{-1} K^{-1})

In the current investigation a heat transfer coefficient greater than 6500 W m^{-2} K^{-1} would be required in order for the assumption of negligible temperature difference across the foil to fail. Heat transfer coefficients are not the focus of this investigation, however the heat transfer coefficient reported for the 3 mm diameter jet in the comparative study, figure 3.2, is less than 1000 Wm^{-2} K^{-1}. Using this magnitude as a guide, and accounting for the difference in test diameter and Reynolds number validates the assumption of negligible temperature difference across the foil for this study. During testing the upper surface recovery temperature distribution resulting from jet impingement is recorded indirectly and non-intrusively from the lower surface of the foil via infrared thermography, Patil and Narayanan (2005). To facilitate accurate temperature measurement, the exposed underside area of the foil was covered with a thin layer of matt black paint with an emissivity ε = 0.95. Utilising a FLIR ThermoCam A40 fitted with a close focus lens, IR thermal images were captured to record the temperature distribution of the foil. The total camera viewing area was 15.2 mm by 11.4 mm with a spatial resolution of 47.5 μm and a frame rate up to 50 Hz.

3.1.4 FLOW LOOPS

During operation, dry air was supplied at a line pressure of 1000 kPa to a 100 L air tank, figure 3.17. On the outlet of the tank was a pressure regulator valve which was set to 150 kPa to allow for accurate operation of the test mass flow controller. Air from the tank was supplied to a MKS type 1179A mass flow controller (0-20 LPM ± 1% F.S.). Applying variable voltage (between 0-5 V) to the mass flow controller though the use of a TTi FX2020R power supply allowed for the control of the air flow rate. The relationship between input voltage to the mass flow controller and the flow rate was linear. The output

from the mass flow controller was measured with a multimeter. The air flowing from the mass flow controller was piped to the plenum.
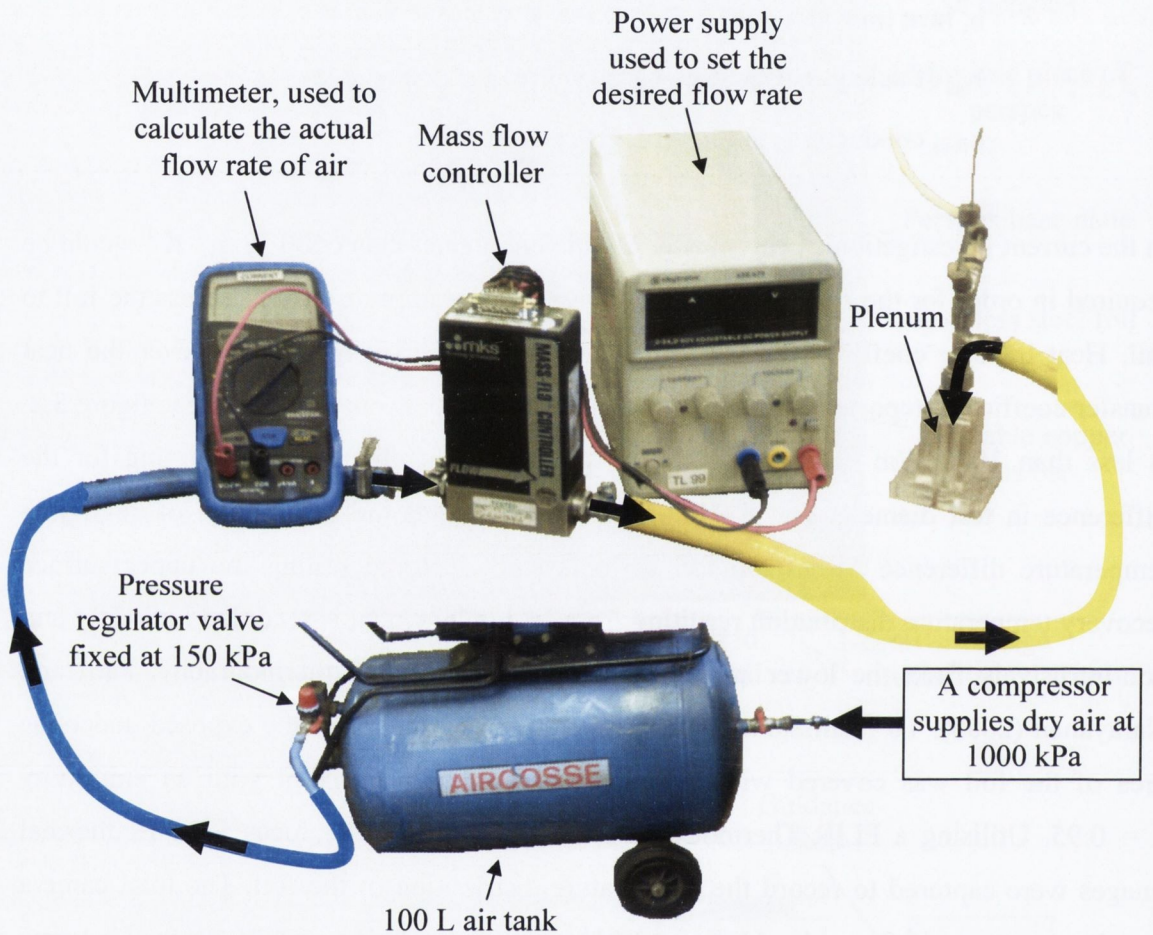
Figure 3.17, Air flow loop.

Contained within the nozzle plate are water channels that collectively function as a heat exchanger; this heat exchanger was designed to maintain the plenum at ambient temperature for future tests involving heated surfaces. The nozzle heat exchanger is described in section 3.1.1 and illustrated in figure 3.3. The inlet and outlet of the water channels were connected to brass fittings, figure 3.4, which were in turn connected to flexible piping as shown in figure 3.18. The coolant water used in the nozzle heat exchanger comes from a reservoir, figure 3.18. Then using a Lowara NTLM34/2 pump, the reservoir water was pumped through a cross flow heat exchanger taken from a 2000 Nissan

Micra. Water exiting the cross flow heat exchanger was at ambient temperature. This water was then passed through the nozzle heat exchanger to maintain the confinement surface at ambient temperature.
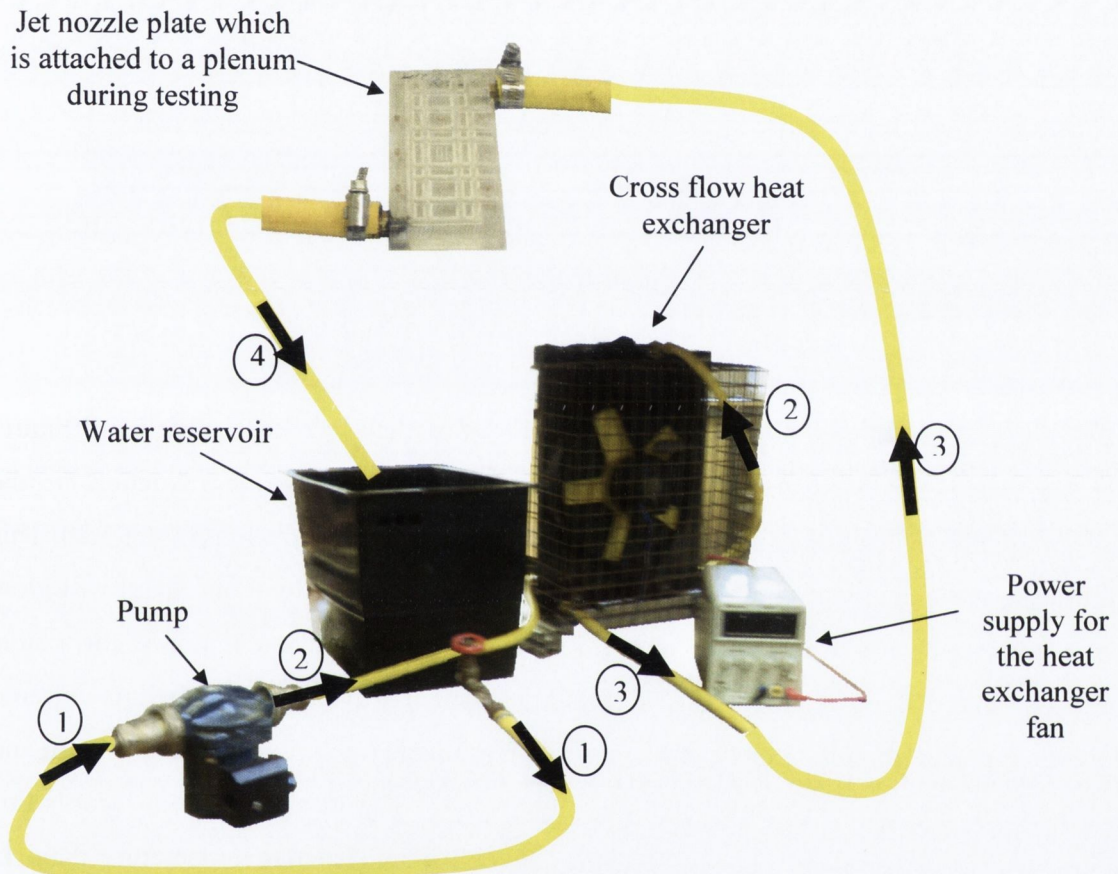
Figure 3.18 Water flow loop (the numbering inside the circles indicates the flow path).

3.1.5 INFRARED THERMOGRAPHY SYSTEM

The infrared spectrum was discovered accidentally by Herschel in 1800. While he was observing the sun, he was searching for an optical filter material to reduce the brightness of the sun's image in telescopes. He noted that different filters allow varying amounts of the sun's heat to pass. Intrigued by this observation he performed Newton's prism experiment, but investigated the heating effect as opposed to visual distribution of intensity in the spectrum. He moved a blackened thermometer through the colours produced by the spectrum and the temperature readings increased from the violet end to the red end. This was already known from findings produced by Landriani in 1777. However, Herschel was

the first to recognize that the point of maximum heat lay outside the visible spectrum in what is known today as infrared wavelengths. The different bands of electromagnetic radiation are shown in figure 3.19. The infrared band lies between that of visible light and microwaves.
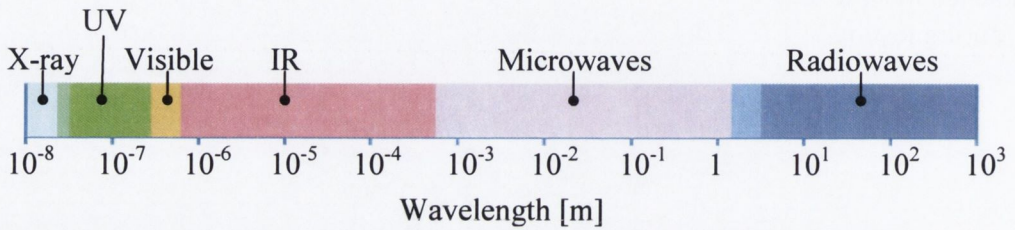
Figure 3.19, The electromagnetic spectrum.

All objects emit infrared radiation, the amount of which increases with temperature. Another phenomenon associated with increasing temperature is the reduction in the wavelength at which a body emits most of its radiative power, as shown in figure 3.20. This shift in the wavelength at which peak radiation occurs explains why a hot metal will glow red and then orange with increased temperature, as it begins to emit radiation in the visible spectrum. There is no unambiguous definition of which wavelengths constitute infrared radiation but according to Daniels et al. (1975) a reasonable interval is between 0.7 μm and 1 mm which lies between visible light and microwaves. The infrared camera records this radiation emitted from the test surface and converts it into spatial temperature data. In general, when radiant energy strikes a surface, part of the radiation is reflected, part is absorbed and part is transmitted. This statement may be characterised as follows,

$$\alpha^* + \rho^* + \tau = 1 \tag{3.2}$$

where,

   α^*, absorptivity

   ρ^*, reflectivity

   τ, transmissivity
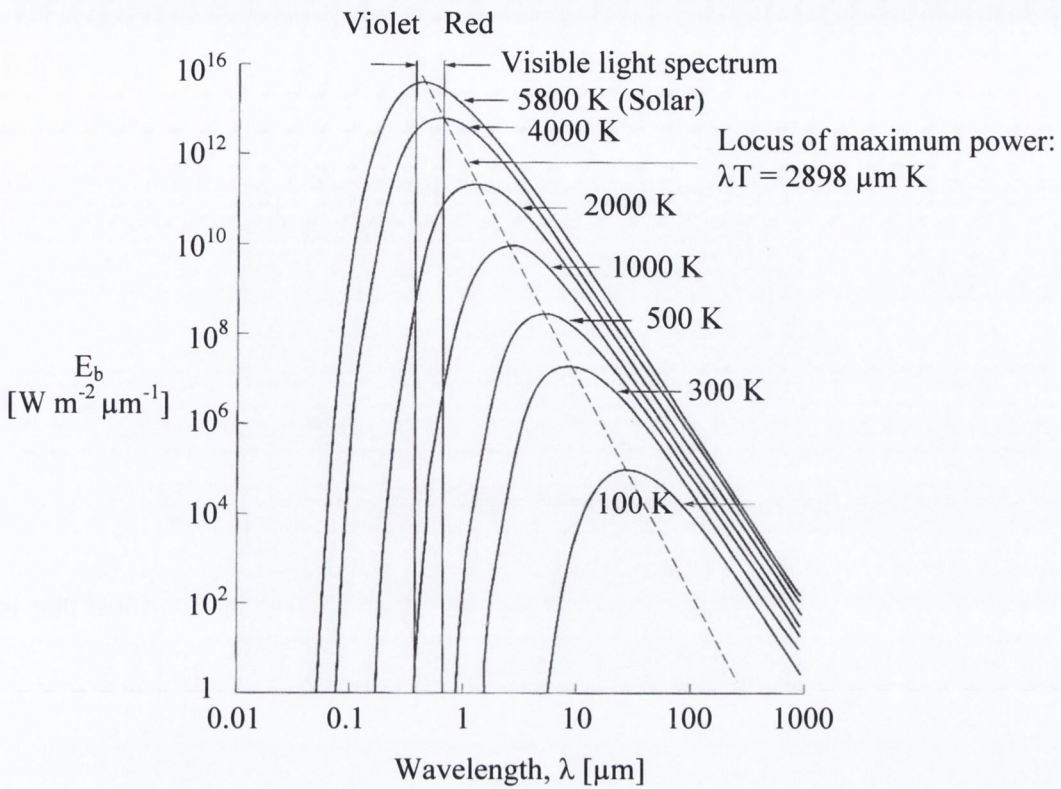
Figure 3.20, Blackbody spectral radiant emittance according to Planck's law, plotted for various absolute temperatures, Çengel (2003).

The following relation is valid if the surface is approximated as a diffuse, grey surface,

$$\alpha^* = \varepsilon \qquad (3.3)$$

where,

ε, the emissivity is the ratio of the emissive power of a body, E, to that of a blackbody, E_b, at the same temperature, T,

$$\varepsilon(T) = \frac{E(T)}{E_b(T)} \qquad (3.4)$$

Using the relationship 3.2 and the fact that most bodies do not transmit thermal radiation (opaque bodies), then equation 3.2 may be restated as:

$$\varepsilon + \rho^* = 1 \tag{3.5}$$

Jozef Stefan in 1879 used experimental measurements made by John Tyndall to show that the total radiant energy emitted from a black body surface per unit area is proportional to the absolute temperature of the body, T, to the fourth power. This relationship was later derived by Ludwig Boltzmann in 1884 from thermodynamic considerations and became known as the Stefan-Boltzmann law, equation 3.6.

$$E_b = \sigma T^4 \tag{3.6}$$

where,

σ, Stefan-Boltzmann constant, 5.67×10^{-8} (W m^{-2} K^{-4})

Equation 3.6 can be modified for evaluation of the emissive power from a surface that is not a black body by using the relationship in equation 3.4.

$$E = \varepsilon \sigma T^4 \tag{3.7}$$

If E could be measured with some instrument the temperature of a black body could be calculated. Unfortunately, it is not E that is measured by the thermographic camera but rather a portion of the thermal radiation defined by the spectral sensitivity of the specific camera. Therefore, each camera must be calibrated and given a relationship between registered thermal radiation and the temperature of the depicted object, Peacock (2006). In this study a Flir ThermoCam A40 with a close focus 50 µm lens is used. It has a spectral range from 7.5 to 13 µm and uses a focal plane array detector that consists of a matrix of 240 by 320 sensors with no common reference temperature. It is therefore necessary to carry out a pixel-by-pixel calibration of the camera, Rainieri and Pagliarini (2002a). The calibration of the IR camera is discussed in the next chapter.

3.2 EXPERIMENTAL PROCEDURES

- The air loop is activated and the system is checked for leaks using a leak detector.

- The jet nozzle is lowered onto the impingement surface and the 3 springs supporting the impingement surface, figure 3.14, are adjusted so that the nozzle and the stainless steel foil are aligned with one another.

- The height of the nozzle above the impingement surface is calibrated as described in section 3.1.3 and desired nozzle heights are established by adjusting a micrometer on the traversing stage.

- A desired value of flow rate and hence Reynolds number is set via the mass flow controller.

- When steady state is reached the temperature of the jet in the plenum and an infrared image of the test surface is recorded. These images are 15.2 mm by 11.4 mm in size.

- In the multi jet study, three different jet configurations are tested; a single jet, a 2×2 in-line jet array and a 3×3 in-line jet array, all of diameter 610µm. For the multiple jet arrays the interjet spacings are altered from 2.5 to 6 jet diameters. Tests are carried out at Reynolds numbers of 5100 and 10500 corresponding to Mach numbers of 0.33 and 0.68 and H/D values of 0.5, 1, 2, 3, 4 and 5.

- For the confinement study this procedure is repeated for a H/D value of 1 and Re values of 7500 and 14400 that correspond to Mach numbers of 0.36 and 0.64, respectively. Nozzle exit to confinement surface spacings, Z_{plate}/D, of 0, 4 and 12 are studied in the investigation into the effects of confinement.

4 DATA ANALYSIS

This study reports recovery temperature and lateral conduction distributions for a number of jet configurations at two Reynolds/Mach number settings. The evaluation of these terms is discussed in this section. The main two measured quantities used in the calculation of Reynolds number and Mach number are the flow rate of the air and the stagnation temperature of the jet measured in the plenum. The temperature of the jet in the plenum is used to estimate the temperature of the jet at the nozzle exit. The analytical procedure used to determine temperature of the jet at the nozzle exit is described. The accuracy of the modified recovery distributions depends on the accuracy of the IR camera, so a pixel-by-pixel calibration is carried out in situ. Due to the large temperature gradients, large magnitudes of the heat flux due to lateral conduction are reported. Methods for estimating magnitudes of lateral conduction heat flux from temperature distributions are highly sensitive to 'noise' in the thermal image. To remedy this a Wiener filter is used in the evaluation of heat flux magnitudes due to lateral conduction. At the end of this section the accuracy of the measurements and the uncertainty of the results reported are presented.

4.1 REYNOLDS AND MACH NUMBERS

In section 2.6 the static temperature, T_{static}, and total temperature, T_{total}, were defined. The dependence of these two terms on one another can be quantified by the isentropic relationship in equation 4.1.

$$T_{static} = \frac{T_{total}}{1 + M^2(\gamma - 1)\Big/2} \tag{4.1}$$

where,

γ, is the ratio of specific heats (for air, $\gamma \approx 1.4$)

As the second term in the denominator becomes non-negligible with increasing M, the temperature of the high speed air in the nozzle can become measurably lower than the

stagnation temperature of the air measured in the plenum, T_{total}. T_{static} at the exit of the nozzle is used in evaluation of the fluid properties which determine the Reynolds number and Mach number, as described in section 2.5. The static air temperature at the nozzle exit is evaluated by using the iterative approach described by Goodro et al. (2007). From the test instrumentation, both the total air temperature, T_{total}, and the volumetric flow rate, Q, of the air are measured. T_{total} is recorded by placing a K type thermocouple at the base of the plenum where it measures the temperature of the stagnated air. Q is recorded from a MKS type 1179A mass flow controller which outputs readings in SLPM (standard litres per minute). For the flow controller standard pressure, $P_{standard}$, is defined as 760 mm Hg and standard temperature, $T_{standard}$, is defined as 0 ^0C. The density of the air at standard conditions, $\rho_{standard}$, is evaluated from the ideal gas equation;

$$\rho_{standard} = \frac{P_{standard}}{R * T_{standard}} \qquad (4.2)$$

where,

R^*, is the gas constant (for air, $R^* = 286.9 \text{ J kg}^{-1} \text{ K}^{-1}$)

This value of density is then used to work out the mass flow rate of the air, $\dot{m}$, equation 4.3.

$$\dot{m} = \rho_{standard} Q \qquad (4.3)$$

Then a value of the static temperature of the air at the nozzle exit is estimated, $T_{nozzle\ exit}^*$; the air temperature in the plenum is used as an initial estimate. Fluid properties at this estimated static temperature were used to evaluate the Mach number, M, of the air at the nozzle exit.

$$\rho_{nozzle\ exit} = \rho_{standard} \left(\frac{T_{standard}}{T_{nozzle\ exit}^*} \right)^{\frac{1}{\gamma-1}} \qquad (4.4)$$

$$u_{\text{nozzle exit}} = \frac{\dot{m}}{\rho_{\text{nozzle exit}} \, A_{\text{cross section}}} \qquad (4.5)$$

where,

$A_{\text{cross section}}$, is the cross sectional area of the nozzle.

$$c_{\text{nozzle exit}} = \left(\gamma R * T_{\text{nozzle exit}}*\right)^{0.5} \qquad (4.6)$$

$$M_{\text{nozzle exit}} = \frac{u_{\text{nozzle exit}}}{c_{\text{nozzle exit}}} \qquad (4.7)$$

This value of Mach number is then substituted into equation 4.1 and the validity of the estimated air temperature at the nozzle exit is checked. Based on this result new estimates of the air temperature at the nozzle exit were made and this process of estimating the temperature, calculating the corresponding Mach number and checking the accuracy of the estimate using the isentropic relationship is repeated until the estimated temperature satisfies equation 4.1. $T_{\text{nozzle exit}}$ is then used to calculate the fluid properties required to evaluate Reynolds number and the corresponding Mach number.

4.1 RECOVERY FACTOR

As discussed in section 2.6, directing a high speed jet onto an unheated ambient surface may produce a non-uniform surface temperature distribution due to mixing and recovery effects. Also, the jet may be much cooler than ambient, due to compressibility effects, as outlined above. The method commonly used for obtaining the adiabatic wall temperature, $T_{a,w}$, is outlined by Meola et al. (1995) and Meola and Carlomagno (2004). It involves recording the temperature distribution resulting from a jet impinging onto a surface with zero heat flux i.e. an insulated surface. This method was carried out in the current investigation but unlike tests carried out by Meola, the resulting unheated wall temperature distribution, $T_{u,w}$, demonstrated temperature gradients sufficiently high to induce lateral conduction within the foil. As a result, $T_{u,w} \neq T_{a,w}$ in the current investigation. Some studies present $T_{a,w}$ in the non-dimensional form of the recovery factor. The definition of the

recovery factor R has been modified in the current investigation, equation 4.8, as $T_{u,w} \neq T_{a,w}$.

$$R = 1 + \frac{T_{u,w} - T_{total}}{u_{nozzle\ exit}^2 / 2C_P} \qquad (4.8)$$

The values of T_{total} and $u_{nozzle\ exit}$ are discussed in the previous section. The distribution of $T_{u,w}$ is obtained by taking thermal images of the jets impinging onto the test foil, an example of which is shown in figure 4.1. As R is defined in terms of $T_{u,w}$ instead of $T_{a,w}$ lateral conduction has an influence on the recovery factor distributions reported. The significance of lateral conduction for R is that it decreases the absolute values of maxima and minima in the recovery factor distributions as heat is conducted from warm regions to cool regions. As will be discussed in more depth, the spatial fluctuations in temperature seen in these images have a severe impact on the analysis of the heat transfer within the foil since seemingly small scatter in the temperature field can have a disproportionately large impact on the evaluation of the corresponding 2nd spatial derivative distribution associated with the temperature field. These derivatives are important as they are used in the calculation of heat conducted within the foil, which is considered in the next section.
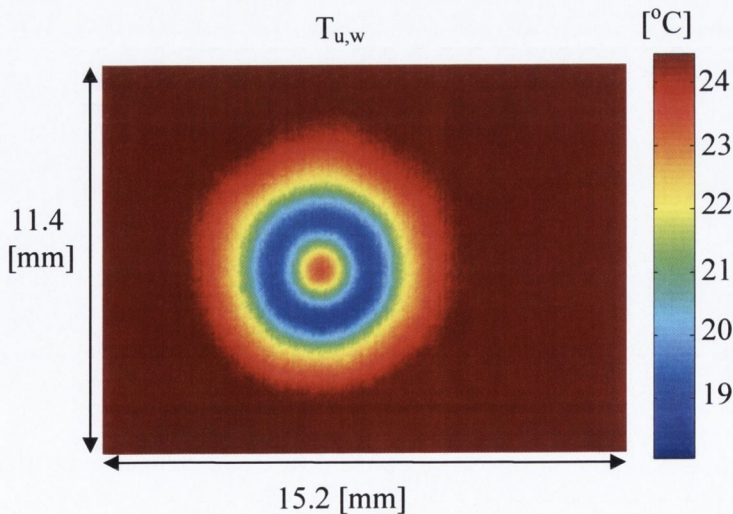
Figure 4.1, Infrared images recorded for a single 910 μm diameter confined jet impinging onto an unheated surface with Re = 14400, M = 0.64 and H/D = 1.

4.2 LATERAL CONDUCTION

In the case of an ohmically heated thin foil it is often reasonable to assume a constant heat flux boundary condition. However, as discussed by Patil and Narayanan (2005) and others, the constant heat flux boundary condition may, in certain circumstances, no longer hold true. For the case where the impingement jet diameter is very small, large temperature gradients occur over a small surface area, causing heat to flow laterally by molecular diffusion. The magnitude of the local heat flux due to lateral conduction can be of the same order of magnitude as the heat flux generated by resistive heating. Patil and Narayanan (2005), who tested a 125 μm diameter single jet, reported q''_{lc} magnitudes five times greater than the heat flux generated in the foil. This demonstrates that conjugate heat transfer becomes increasingly more important at small scales and complicates the analysis significantly compared with large diameter jet impingement. Conjugate heat transfer refers to a heat transfer process involving an interaction of conduction within a solid body and the convection from the solid surface to fluid moving over the solid surface, Jahangeer et al. (2007). Whether or not the magnitude of lateral conduction is significant can be indicated through the evaluation of a non-dimensional term developed by Hetsroni et al. (1996). They used a heated thin foil technique to study wall temperature fluctuations in a turbulent channel flow. In their study they noticed temperature heterogeneity or thermal spots and wished to know whether or not these thermal spots were small enough to result in lateral conduction within the foil. They assumed their foil to be insulated on one side and they assumed both radiation and natural convection losses were relatively small. With these assumptions they analytically developed the relationship given in equation 4.9. When this relationship is satisfied the effects of lateral conduction are insignificant.

$$\frac{4k_{foil}t_{foil}}{h_{average}d^2} << 1 \qquad (4.9)$$

where,

d, represents the diameter of the spot of large temperature difference, which emerged due to the turbulence/wall interaction, Hetsroni et al. (1996). For this study the jet diameter was used for d.

$h_{average}$, is the average convective heat transfer coefficient over the spot.

- 66 -

This criterion is used to indicate if the effects of lateral conduction are significant for the current investigation. As h values corresponding to the R values reported here are unknown, values taken from the comparative study shown in figure 3.2 are used; H/D = 4, Re = 20000, k_{foil} = 16.3 W m^{-1}K^{-1}, t_{foil} = 25 μm, D = 3 mm and $h_{stagnation}$ ≈ 1 000 W m^{-2} K^{-1} leads to an approximate value of 0.18 for the term on the left hand side of equation 4.9. This term is inversely proportional to the square of the jet's diameter, so this indicates that conduction effects will be significant for the 610 μm diameter recovery temperature distributions. Therefore in order to understand heat transfer in such a study the magnitudes of conduction with the foil must be quantified first. Stafford et al. (2009) performed tests using a similar set up to the current investigation: an IR camera and a thin foil coated with a thin layer of paint. They defined an equation that accounted for lateral conduction in both the foil and paint layer, equation 4.10. Evaluation of the Biot number confirms that the paint layer is sufficiently thin to neglect temperature differences across its thickness. The conductivity of the paint, k_{paint}, was not available from the manufacturer. However, findings from Raghu and Philip (2006) suggested a k_{paint} value of 1.38 W m^{-1} K^{-1} for matt black paint coating. The thickness of the stainless steel found without paint, t_f, was measured at various locations using micrometer and was found to be 25 μm. After the foil was painted the thickness of the paint layer, t_p, was evaluated, using a micrometer, to be 15 μm.

$$q''_{lc} = \left(k_{foil}t_{foil} + k_{paint}t_{paint}\right)\left(\frac{\partial^2 T_{u,w}(x,y)}{\partial x^2} + \frac{\partial^2 T_{u,w}(x,y)}{\partial y^2}\right)$$ (4.10)

where,

q''_{lc} , heat flux transferred due to lateral conduction within the foil and paint.

k_{foil}, conductivity of the foil (k_{foil} = 16.3 W m^{-1} K^{-1})

Patil and Narayanan (2005), used a method for calculating q''_{lc} resulting from a single axisymmetric jet impinging onto a foil. Their method involved radial averaging of the temperature distribution about the centre of the jet and then curve fitting this distribution using curve fitting software, Tablecurve 2D. The software calculates the derivatives from the curve fit which allows for the calculation of the distribution of heat flux due to lateral

conduction using equation 4.10 in polar form. This method of calculating temperature derivatives is only valid for axisymmetric temperature distributions and has limited accuracy, so the method described by Patil and Narayanan (2005) is not feasible to use for analysing results in the current investigation. However, the possible use of advanced curve fitting software such as Tablecurve 3D to generate derivatives corresponding to the infrared temperature distributions is investigated. The temperature distribution shown in figure 4.2 (a) is inputted into Tablecurve 3D. The curve fitting software then produces a corresponding temperature fit, figure 4.2 (b), and also solves for the second partial derivatives of the temperature distribution in the X and Y direction, allowing for the heat flux due to lateral conduction, equation 4.10, to be solved, figure 4.2 (c).
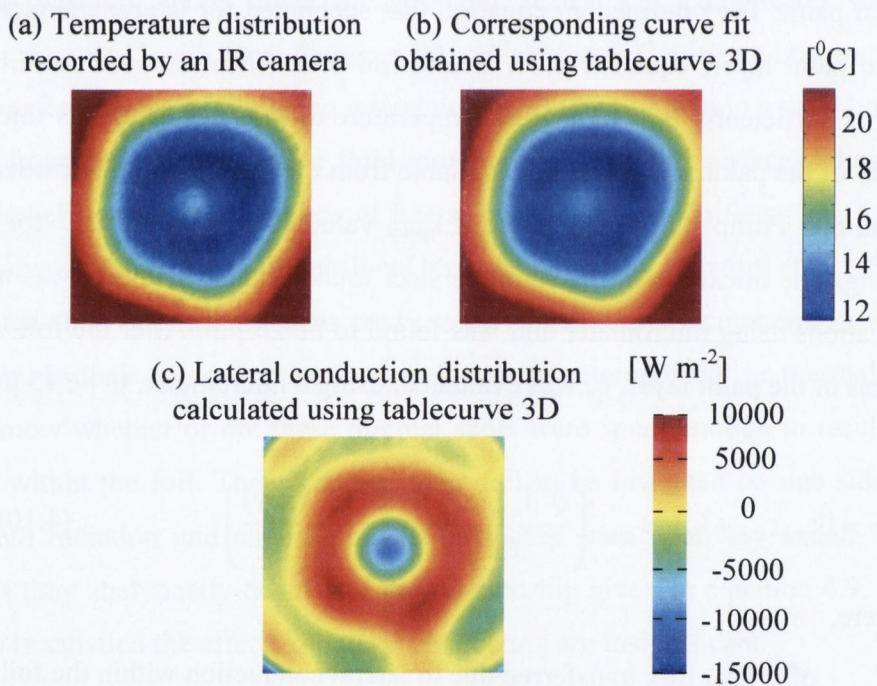
Figure 4.2, Data recorded for a single 610 μm diameter jet with, Re = 10500, M = 0.68 and H/D = 0.6 and analysed using Tablecurve 3D. The size of each image is 3.2 D by 3.2 D, where D is the jet diameter.

The temperature distribution in figure 4.2 (a) was repeatedly studied in Tablecurve. Each study used a different amount of data surrounding the centre of the jet: one image looked at a large amount of data surrounding the jet, another image only looks at the central region of

the jet. The corresponding lateral conduction distributions are given in figure 4.3. One can see that as the range of the temperature distribution about the jet's centre decreases the negative magnitudes of the lateral conduction at the centre of the jet decreases. This occurs because the smaller data set generates a better temperature fit at the centre of the jet. The next step in this study was to look in detail at the centre of the jet. This was achieved by looking at a 0.9 D×0.9 D region, as shown in figure 4.4. First of all a detailed temperature fit was made using Tablecurve, the left hand side of figure 4.4 (b). The problem with this fit is that it is too detailed as it picks up on the noise in the recorded temperature distribution and thus gives a meaningless solution to the lateral conduction distribution. A second temperature fit was carried out, the right hand side of figure 4.4 (b). This time a smoother fit was chosen in Tablecurve 3D but some of the values of the fit outside the region of interest went towards infinity. This affected the second derivatives in the region of interest and thus the resulting lateral conduction distribution is not realistic. The inconsistent results associated with using Tablecurve 3D make it an unattractive method for solving for lateral conduction in the current investigation.
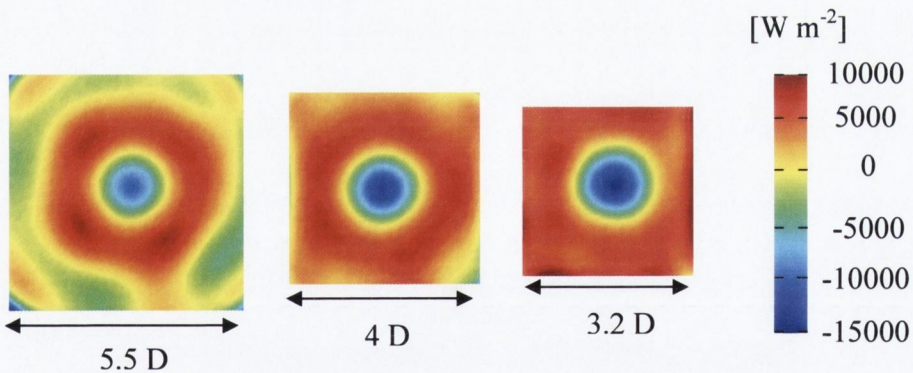
Figure 4.3, Lateral conduction distributions evaluated using various ranges of temperature data from figure 4.2 (a) and Tablecurve 3D.

As an alternative to Tablecurve data processing, a numerical finite difference method was carried out using Matlab, appendix D, to solve for the temperature laplacian, $\Delta T = \partial^2 T/\partial x^2 + \partial^2 T/\partial y^2$. Using the 3 point central difference formula, equation 4.10 was rewritten as equation 4.11. The temperature distribution in figure 4.5 (a) is used along with the finite difference formula to produce the heat flux due to lateral conduction distribution in figure 4.5 (b).
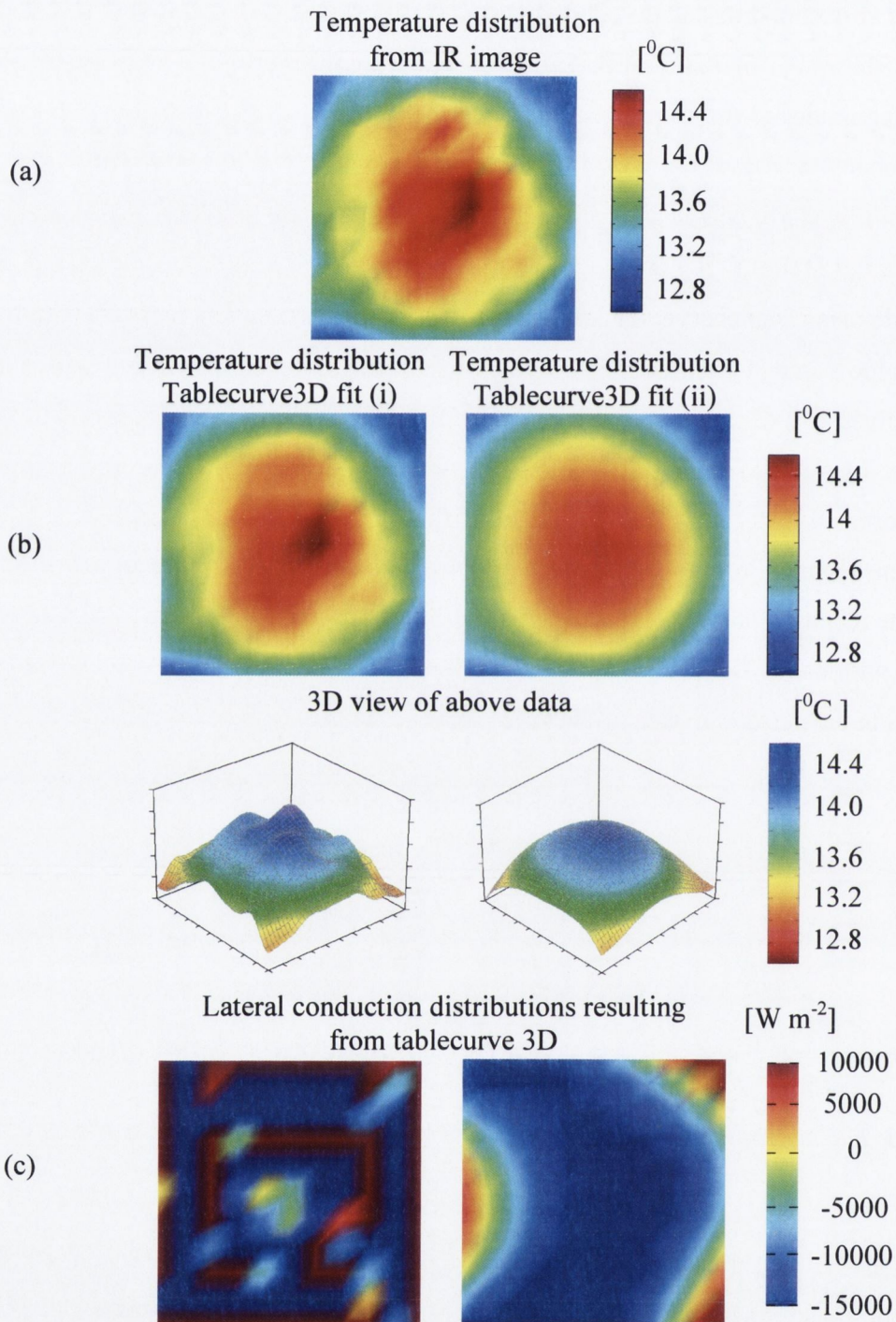
Figure 4.4, (a) The central region of the temperature distribution shown in figure 4.2 (a)
(b) The corresponding temperature distributions after being curve fitted using Tablecurve
3D to (i) a cosine series bivariate order 10 curve and (ii) a Chebyshev X,Y bivariate
polynomial order 5 curve. (c) The corresponding lateral conduction distributions evaluated
from Tablecurve 3D. The size of each image is 0.9 D×0.9 D where D is the jet diameter.

(a)   (b)

IR temperature data   [^{0}C]   Heat flux due to lateral conduction   [W m^{-2}]
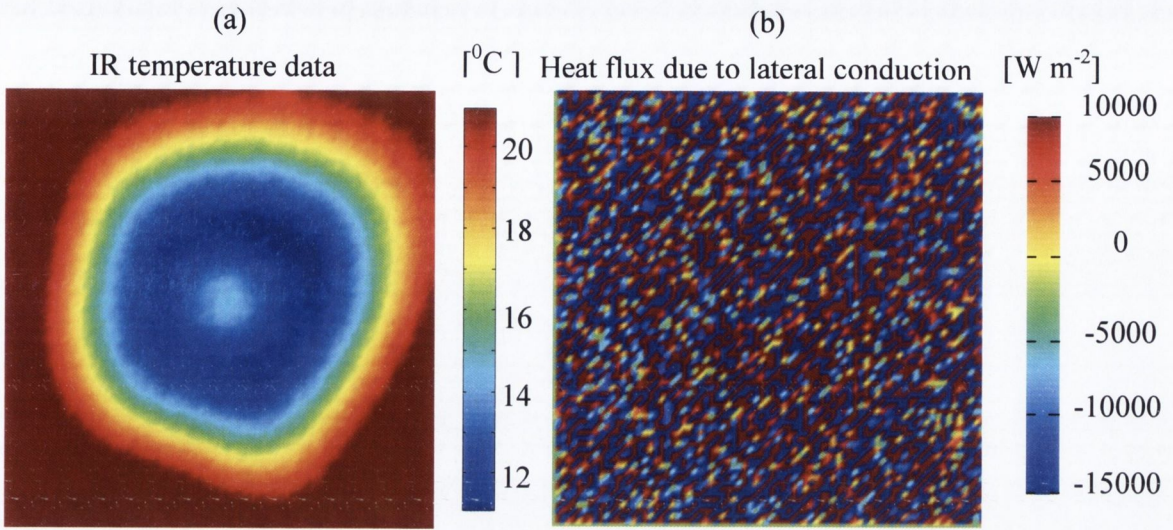
Figure 4.5, (a) The central region of the temperature distribution shown in figure 4.2 (a)
The corresponding lateral conduction distribution evaluated using equation 4.11. Each
image is 3.4 D×3.4 D, where D is the jet diameter.

$$q''_{lc}(i,j) = \left(k_{foil}t_{foil} + k_{paint}t_{paint}\right)\left(\frac{T(i+1,j) + T(i-1,j) + T(i,j+1) + T(i,j-1) - 4T(i,j)}{dx^2}\right)$$

(4.11)

where,

      i and j, are indices corresponding to individual pixel

      dx, is the length of an individual square pixel (dx = dy = 47.5 x 10^{-6} m)

The lateral conduction distribution in figure 4.5 (b) demonstrates the failure of this method to evaluate q''_{lc}. The reason this method fails is due to the seemingly small temperature fluctuations evident in figure 4.5 (a). When the 2nd derivative of this temperature distribution is evaluated these fluctuations dictate the resulting shape of the q''_{lc} distribution. To resolve this problem, different filtering and curve fitting techniques were considered such as the Wiener filter, the thin plate smoothing spline and Fourier analysis. An extensive study of the different filtering techniques showed the Wiener filter and the thin plate smoothing spline to achieve best fits. The use of the spline method is limited as the spline function in Matlab can only handle a limited number of data points (~5k) and the function

requires a large amount of processing time. For these reasons, the Wiener filter is used as the filtering technique for the evaluation of magnitudes of lateral conduction in the current study. This filter is discussed more in the next section.
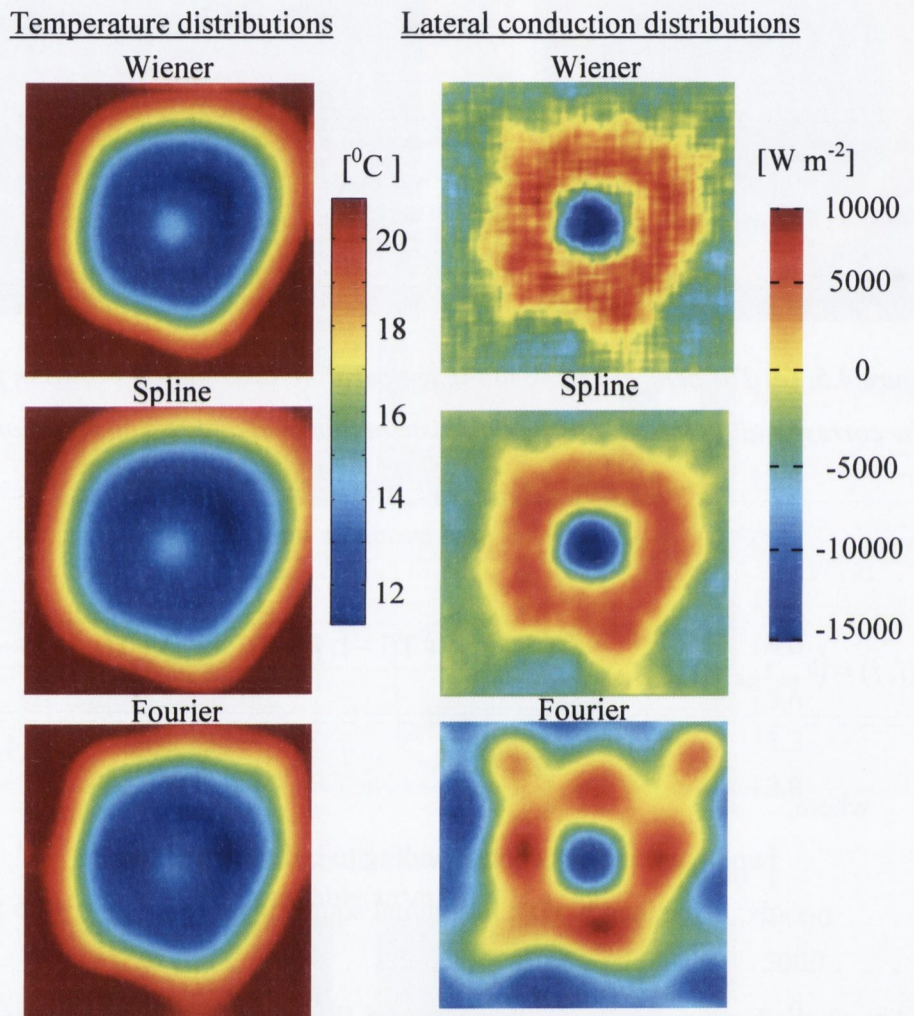
Figure 4.6, The left hand side of this image shows the effect of using various techniques to filter noise from the temperature data shown in figure 4.5 (a). The right hand side of this image shows the various corresponding heat flux due to lateral conduction distributions evaluated using the finite difference method. Each image is 3.4 D ×3.4 D in size.

4.3 WIENER FILTER, EXPERIMENTAL CALIBRATION AND UNCERTANTY

In order to maximise the accuracy of the results reported in this thesis, the IR camera is calibrated in situ and noise within the temperature data is removed through the use of the Wiener filter.

4.4.1 WIENER FILTER

The Wiener filter was developed by Norbert Wiener, Wiener (1949). Its objective is to filter out noise that has corrupted a signal; it does so using a statistical approach. Rainieri and Pagliarini (2002b) recognised the Wiener filter as a powerful tool to overcome the ill-posed nature of the inverse heat conduction problem. They investigated the use of several numerical filters and identified the Wiener filter to be the optimal filter in order to remove the undesired noise from experimental temperature maps to be used in the solution of the inverse heat conduction problem. The reasoning for this is its ability to tailor itself to the local noise level in the signal which enables enhanced smoothening of data when compared to other filtering techniques. The function 'wiener2' was used in the Matlab environment. Details of the function can be found in the image processing toolbox in the Matlab user's guide (1998). The filter uses a pixelwise adaptive Wiener method based on statistics estimated from a local neighbourhood of each pixel. For a successful application of this technique it is necessary to adjust the range of action of the filter, defined by the size of the pixel's neighbourhood, according to the noise level present in the signal. The neighbourhoods, sized N*-by-M* pixels, are used to estimate the local image mean and standard deviation, as defined by equations 4.12 and 4.13.

$$\mu* = \frac{1}{N*M*} \sum_{n1,n2 \in \eta} a(n_1, n_2) \qquad (4.12)$$

$$\sigma**^2 = \frac{1}{N*M*} \sum_{n1,n2 \in \eta} a^2(n_1, n_2) - \mu*^2 \qquad (4.13)$$

where,

a, the matrix to be filtered

n_1, n_2, indices of matrix a located in η

N*, M*, size of the local neighbourhood η

η, the N*-by-M* local neighbourhood of each pixel in the matrix a

μ*, local mean around a pixel,

$\sigma**^2$, local variance around a pixel,

The restored two-dimensional signal b is then estimated as,

$$b(n_1, n_2) = \mu* + \frac{\sigma**^2 - v^2}{\sigma**^2} (a(n_1, n_2) - \mu*)$$ (4.14)

where,

v^2, the variance of the noise.

The necessity of a finite neighbourhood around each pixel causes the technique to fail in the region close to the domain boundaries; these regions have been omitted from the results.

The optimal values of both N* and M* vary depending on the magnitude of the rate of change of the temperature gradients in the x and y direction. Figure 4.7 shows a horizontal cross section of pre-filtered temperature data recorded by the infra red camera. These data are shown in x and y coordinates in figure 4.5 (a). The temperature distribution is filtered using the Wiener filter with varying neighbourhood sizes. Using a low neighbourhood value of 3 seems to produce the best fit but the temperature data are still quite noisy which is not suitable for evaluation of the lateral conduction. The larger neighbourhood value of 15 causes over smoothing of the data and thus the magnitude of the local maximum and minima are dampened and their absolute values are decreased respectively. A neighbourhood value of N* = M* = 9 is chosen to be optimal for the current study and this value is used for the results presented in chapter 5.
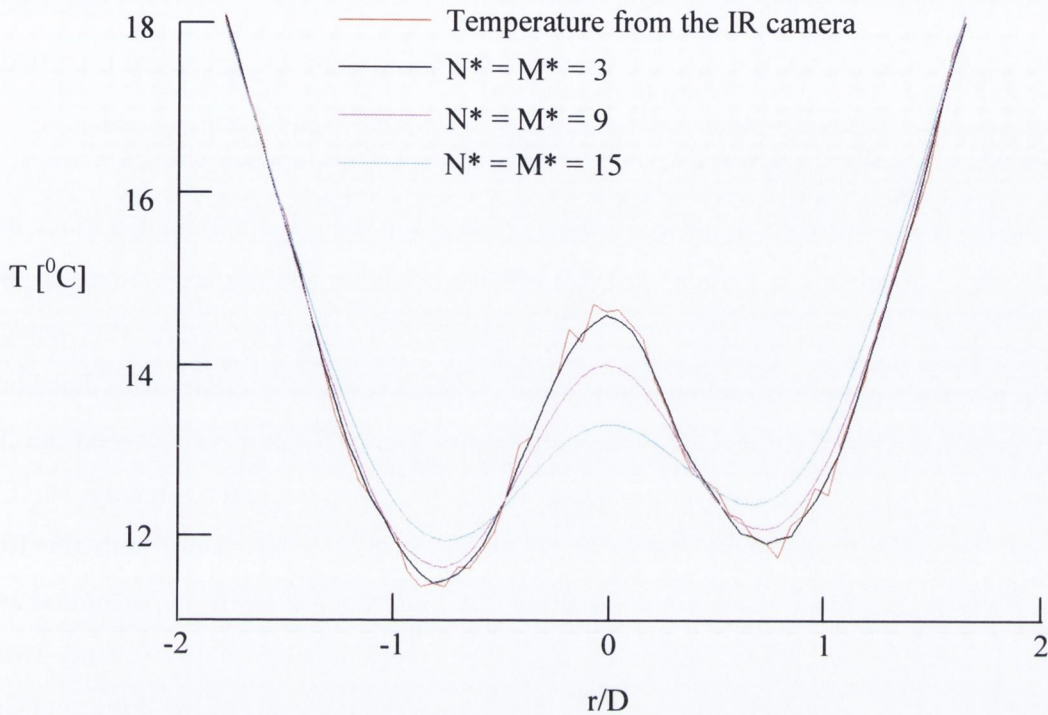
Figure 4.7, The effect of varying the neighbourhood of the Wiener filter.

4.4.2 CALIBRATION

Traditional infrared cameras used a single sensor and essentially rotated a prism to sequentially record the energy emitted by the object over an entire field of view. In the current study a FLIR ThermoCam A40 fitted with a close focus lens with a resolution of 50 μm is used. The A40 camera is equipped with focal plane array technology (FPA) and the camera detector is made up of a matrix of sensors that allow the entire field of view to be recorded by the camera at the same time, without the use of any scanning mechanism. FPA technology has lead to the enhancement of spatial resolution, reduced acquisition time and increased image quality and contrast. However, one of the set backs with FPA cameras is the lack of an internal temperature reference, to which the signal can continuously be compared; this leads to non-uniformity in the outputs from the matrix of sensors. The accuracy and sensitivity of the ThermoCam A40 reported by the manufacturers FLIR is ± 2 ^{0}C (see Appendix B.1 for calibration cert), which is quite large for the current investigation. However, Rainieri and Pagliarini (2002) who tested over a temperature range

from 10 ^{0}C to 70 ^{0}C found that by using the Wiener filter and preparing different calibration curves for each individual sensor a maximum estimated uncertainty of 0.18 ^{0}C could be obtained. In the current investigation a pixel-by-pixel calibration of the IR camera is carried out.

The IR camera is calibrated in situ by mounting a water bath onto the impinging surface in such a way that the water is in contact with the foil. The water is continuously stirred so as to maintain uniform water temperature. The temperature of the water within the sealed water bath was monitored via a pre-calibrated and certified resistance temperature detector (RTD) which is used as a reference for the calibration. The calibration was carried out 3 times by varying the water temperature from 10 ^{0}C to 50 ^{0}C in approximately 10 ^{0}C increments and simultaneously recording the temperature of the foil using both the IR camera and the RTD. Then for each individual pixel a linear regression fit is performed as shown in figure 4.8, and the regression fit is quantified by equation 4.15. Seventy two thousand pixels were calibrated and each pixel has its own unique value of M, slope, and C, y-intercept; these values are shown in figure 4.9. The accuracy of the camera was then determined by looking at how much each temperature point in figure 4.8 deviated from the calibration curve; all 15 temperature points for each of the 72000 pixels were considered and the overall standard deviation of the camera was found. The accuracy of the camera relative to the RTD probe was calculated to be 0.11 ^{0}C. (Note: accuracies are quoted at 95% confidence). Between 0 ^{0}C and 50 ^{0}C the maximum uncertainty of the RTD is 0.18 ^{0}C (see calibration certificate in Appendix B.2), so the actual uncertainty of the reported temperatures in this thesis is 0.21 ^{0}C. The uncertainty of the other experimental measuring devices is given at the end of this section in Table 4.1.

$$T_{RTD} = M \times T_{IR\ Camera} + C \qquad (4.15)$$

where,

T_{RTD}, temperature read by the resistance temperature detector [^{0}C]

$T_{IR\ Camera}$, temperature read by the infra red camera [^{0}C]

Temperature data used for calibrating an individual pixel
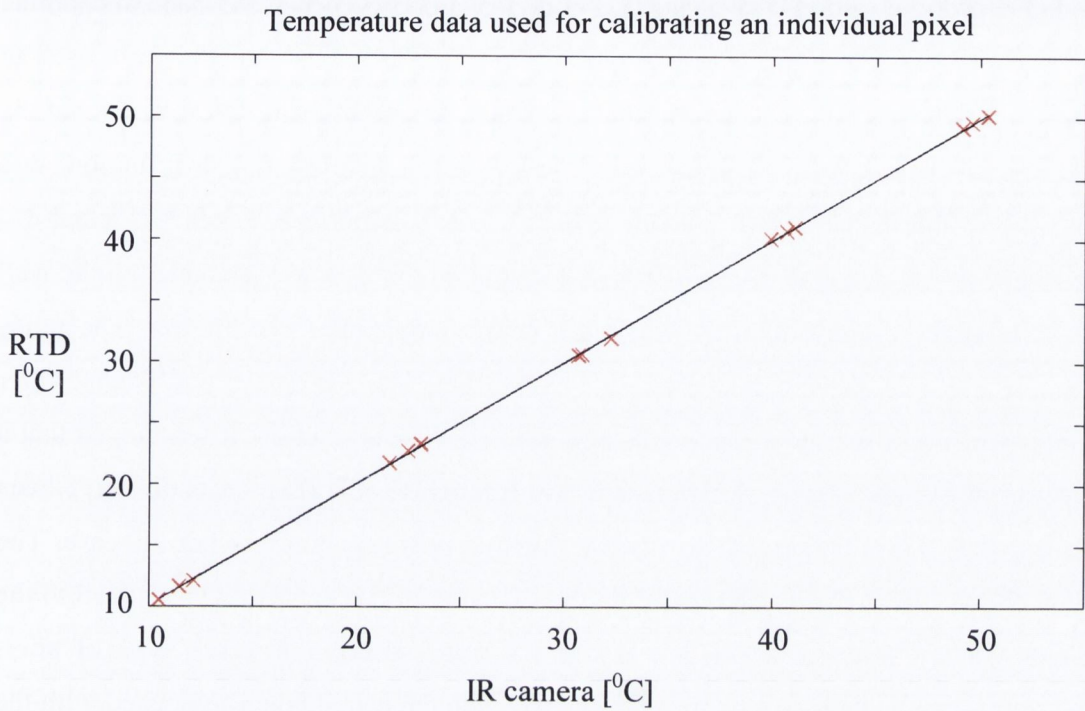
Figure 4.8, Calibration curve for an individual infra red camera pixel.
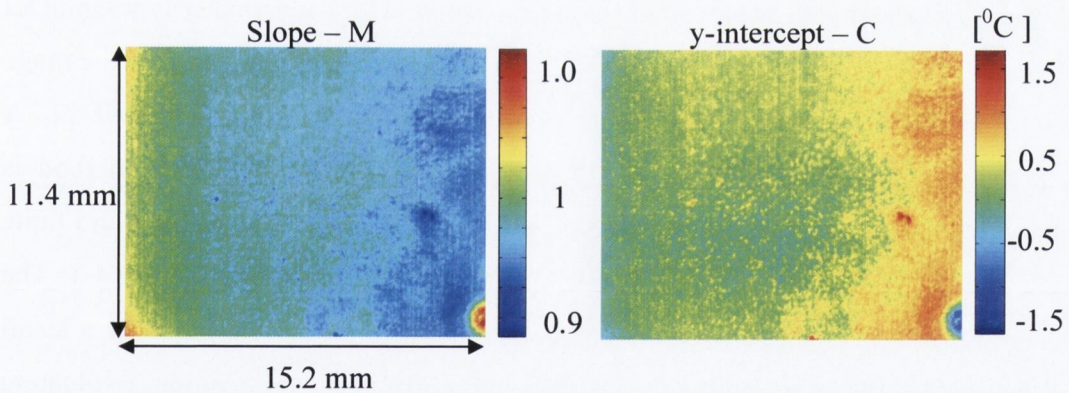
Figure 4.9, Values of slope, M, and the y-intercept, C, used in equation 4.15, for each of the individual pixels.

4.4.3 UNCERTAINTY

Quantifying the level of uncertainty in the heat flux due to the lateral conduction is not possible in this investigation as noisy temperature distribution recorded by the IR camera is filtered twice before q''_{lc} is evaluated. Rainieri and Pagliarini (2002b) refer to the Wiener filter as an optimal technique to overcome the ill-conditions of the inverse problem but they

do not indicate the uncertainty associated with the technique. Efforts were made to examine the accuracy of the filtering process. A well defined mathematical function was used to produce a well defined temperature distribution. The temperature distribution resembled the temperature distribution of a single jet. Then a corresponding q''_{lc} distribution was evaluated from the mathematical function. This q''_{lc} distribution represented the actual q''_{lc} distribution corresponding to the temperature distribution. Noise was then added to the well defined temperature distribution to produce a noisy temperature distribution. The noisy temperature distribution was then used along with the finite difference and wiener filter method, described in section 4.3, to evaluate a filtered q''_{lc} distribution. It was hoped that a comparison of the actual q''_{lc} distribution to the filtered q''_{lc} distribution could have been used to quantify the accuracy of the filtering method however this was not the case. The accuracy of this comparison was limited by the selection of the noise that was added to the temperature distribution, i.e. a different accuracy was estimated for each type of noise applied to the signal. As it was not possible to replicate the actual noise associated with the IR camera this comparison failed. To gain an indication of the accuracy of the Wiener filter method, a comparative analysis is carried out on the single 610 µm diameter impinging jet with Re = 10 500, M = 0.68 and H/D = 0.6. This particular case is chosen, as over the range of tests studied, this particular test demonstrates the largest absolute magnitudes of q''_{lc}. A cross section of q''_{lc} evaluated using the Wiener filter and finite difference method is compared to a q''_{lc} distribution evaluated using Tablecurve 2D. The Wiener filter and finite difference method is the method used in this thesis and is described in section 4.3. The Tablecurve 2D method is chosen for the comparison as using the software, over a small range of data points, allows for and accurate calculation of the q''_{lc} distribution. Evaluating q''_{lc} using Tablecurve 2D involves taking a temperature cross section and curve fitting it using the Tablecurve 2D software. The first and second partial derivates of the temperature distribution with respect to radial distance from the jet's centre are calculated using the software. These partial derivatives are then used along with equation 4.11 to evaluate the q''_{lc} distribution, figure 4.7. This figure shows the two methods to be comparable. The largest difference between the two methods is at the jet's stagnation point where q''_{lc} evaluated using the Wiener filter is ~21% less than the value of q''_{lc} evaluated using Tablecurve2D. This discrepancy is caused by the unavoidable over smoothening that is associate with the Wiener filter, section 4.4.1.

For the purpose of uncertainty calculation, each measurement is denoted by x_i and the uncertainty in the measurement w_i. The result of a calculation using these measurements is denoted by Z and the uncertainty in the calculated result is denoted by w_z. The uncertainty w_z is calculated using the method of Kline and McClintock (1953), using the following equation,

$$w_z = \sqrt{\left(\sum_{i=1}^{n} \left[\frac{\partial Z}{\partial x_i} w_i \right]^2 \right)} \qquad (4.16)$$

The maximum experimental uncertainties are summarised in Table 4.2.
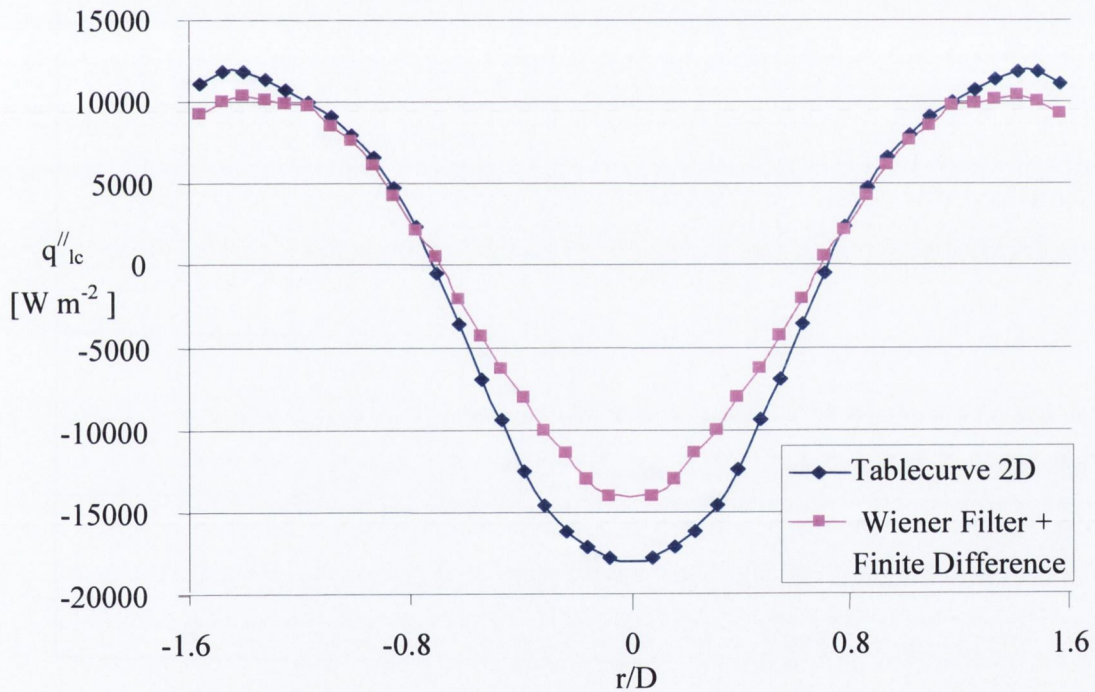
Figure 4.10, A comparison of lateral conduction distributions evaluated using (i) the 2D curve fitting software Tablecurve 2D and (ii) using the Wiener filter + the finite difference method.

Table 4.1, Measurement error.

Parameter (Make, Type)	Error
Temperature (FLIR ThermoCam A40)	$\pm 0.21\ ^0C$
Air Volumetric Flow Rate (MKS Type 1179A Mass-Flow Controller 0-20 SLPM, see Appendix B.3 for calibration cert)	$\pm 1\ \%$ FS
Nozzle to Impingement Surface Spacing, H Two sources of error existed in calculating this parameter; (i) The distance traversed (Paker Hannifin Daedal Micrometer) (ii) Zeroing the Nozzle to Impingement Surface Spacing, section 3.1.3 (Canon Digital IXUS 70)	± 0.00008 in/in travelled ± 0.021 mm
D (Tool Maker Mitutoyo 30X Microscope with Micropak)	$\pm 4.3\%$
S (Tool Maker Mitutoyo 30X Microscope with Micropak)	$\pm 3.3\%$

Table 4.2, Calculated uncertainty in main parameters.

S/D	H/D	Re	R
$\pm 5.4\ \%$	$\pm 8.5\ \%$	$\pm 4.4\ \%$	$\pm 8.8\ \%$

5 RESULTS

This chapter contains a description and discussion of the results obtained in the current investigation. Results in this section are presented in terms of recovery factor, R, and heat flux due to lateral conduction, q''_{lc}. Due to the large amount of data studied only a selection of the distributions are presented in this section, however, the temperature distributions corresponding to all tests studied can be found in appendix C.

In the literature, the recovery factor of an impinging jet is defined as the ratio of the actual (measured) rise in temperature of the jet as it impinges onto a surface to the ideal rise in temperature of the fluid that is decelerated as the jet approaches the surface. The standard definition of the recovery factor is discussed in section 2.6 however the definition of recovery factor is modified for the current study. The modified definition of the recovery factor is discussed in section 2.6 and section 4.2. The recovery factor used in this study is defined as follows:

$$R = \frac{T_{u,w} - T_{static}}{T_{total} - T_{static}} = 1 + \frac{T_{u,w} - T_{total}}{u^2/2C_P} \qquad (5.1)$$

where,

$T_{u,w}$, is the temperature distribution resulting from the impingement of a jet onto an unheated wall, [K]

T_{static}, is the jet's static temperature, equation 4.1, [K]

T_{total}, is the jet's total temperature, [K]

u, is the exit velocity of the jet, [m s^{-1}]

C_p, is the specific heat capacity, [kJ kg^{-1} K^{-1}]

For high subsonic Mach number jet impingement the distribution of the recovery factor is non-uniform due to compressibility effects. The presence of vortical structures also influences the shape of the recovery factor distributions, Fox et al. (1993). This non-uniformity in R is of interest as the heat transfer from high Mach number jets is dependent

on it. Findings from the literature report the recovery factor to be independent of Re, but dependent on H/D and r/D, Goldstein et al. (1986). They also show, for a single jet, a minimum in the recovery factor distribution occurs for H/D $\leq$ 4. Meola and Carlomagno (2004) found this minimum to occur at r/D $\approx$ 1.2. Recovery values greater than unity have been reported at the stagnation point for larger H/D values.

High speed and small scale jet impingement onto a thin metal foil gives rise to a conjugate heat transfer problem, as described in section 2.8. Thus, the non-uniform temperature distribution in the foil, resulting from convection from the jet, causes significant lateral conduction within the foil. In turn, the conduction within the foil alters the thermal condition of the surface onto which the jet impinges, which in turn has an influence on the convection process. Much study has been carried out into the convective heat flux resulting from an impinging jet, but most of these investigations try to ensure that lateral conduction is negligible, so that the effects of q''_{conv} can be studied explicitly. Although this may simplify the experimental testing, in many practical cooling applications the effects of q''_{lc} are desirable as it can act as a heat spreader. An obvious case would be cooling of electronic components. Lallave et al. (2007), who studied impinging jets on a rotating disk, varied the thermal conductivity of the disk. They found higher conductivity materials to maintain a more uniform temperature distribution at the solid fluid interface as a result of increased conduction effects. Stafford et al. (2009) showed how much lateral conduction increases with increasing plate thickness. The current study aims to contribute to knowledge in this area by focussing on the heat flux due to lateral conduction distribution generated within an unheated surface as a result of high speed and small scale jets impinging onto it. In particular the influence of varying multiple impinging jet parameters on the lateral conduction distribution is investigated. The lateral conduction distributions shown in this study correspond to recovery factor distributions also shown. As discussed in section 2.8, the negative q''_{lc} regions correspond to warm temperature regions, these regions have negative q''_{lc} magnitudes as heat is conducted from these warm regions to cooler regions. Similarly cool temperature regions correspond to positive q''_{lc} regions as heat is conducted into these cool regions.

In this chapter the distributions of recovery factor, R, and lateral conduction heat flux, q''_{lc}, resulting from ambient air jets impinging onto an unheated thin foil surface are presented and the effects of different parameters on these terms are investigated. The parameters studied are nozzle to impingement surface spacing, H, interjet spacing, S, jet population, Reynolds number, Re, and confinement level, Z_{plate}. In the following subsections, each of the parameters are investigated over the following non-dimensional parameter ranges; H/D = 0.6, 1, 2, 3, 4 and 5, S/D = 2.5, 4 and 6, Re = 5100 and 10500 (for the multiple jet study), Re = 7500 and 14400 (for the confinement study), and Z_{plate}/D = 0, 4 and 12. This chapter initially focuses on the effects of confinement, then the characteristics of a single jet are explored and finally the interactions of multiple jets in different jet array configurations are studied.

5.1 CONFINEMENT

Much of the research to date in the area of impinging jet heat transfer has concentrated on unconfined jets but space constraints associated with the implementation of this heat transfer technology in small compact electronic devices has led to interest in confined impinging jet geometries. Choo and Kim (2010) found the thermal performance of the confined jet was 20–30% lower than that of the unconfined jet for a fixed flow rate. A possible explanation for this variation in thermal performance of the two different jet configurations may be taken from the findings of San et al. (1997). They investigated the effects of varying the width of the heated impingement plate, W, on local Nusselt numbers for small diameter jets and found that increasing the surface heating width results in lower stagnation Nusselt numbers. They attributed this phenomenon to flow recirculation. As confined geometries are commonplace for small diameter jets at low jet to plate spacings, it was decided to investigate the effects of confinement on the recovery factor. The rig used for investigation of the effects of flow confinement is described in section 3.1.1. It consists mainly of a confinement surface and a needle that can gradually protrude from the confinement surface. Tests were carried out with a 910 μm diameter jet at H/D = 1, at confinement levels, Z_{plate} = 0D, 4D and 12D and at Reynolds numbers of 7500 and 14400 corresponding to Mach numbers of 0.36 and 0.64. The recovery factor distributions for these tests are shown in figure 5.1 and figure 5.2. Note that Z_{plate} = 0D and 12D corresponds

to maximum and minimum confinement respectively. Figure 5.1 shows full recovery factor distributions, the size of the images is indicated by the scale at the top left of the image. Each surface plot in figure 5.1 contains a coloured dashed line. The colour of the line indicates the level of confinement, Z_{plate}, and cross sectional recovery factor distributions corresponding to these lines are shown in the Cartesian plots in figure 5.2. The main finding from figure 5.2 is that recovery factor is virtually independent of the level of confinement, over the range of parameters studied. Other interesting trends are visible in this figure but to avoid repetition these same trends will be discussed later for the 610 μm diameter single jet in section 5.2. Due to the small scale of the impinging jets studied temperature gradients within the foil are sufficiently large to generate heat fluxes due to lateral conduction, q''_{lc}, within the foil. Distributions of q''_{lc} corresponding to the recovery data in figure 5.1 and figure 5.2, are shown in figure 5.3 and figure 5.4. Figure 5.4 shows that the magnitudes of heat flux due to lateral conduction at the lower Reynolds number values of 7500 are small compared to the magnitudes associated with q''_{lc} values for the Re = 14400 tests. As a result, the effects of noise are more evident at lower Reynolds number values. Nonetheless, the trends seen in the q''_{lc} distributions for both the Reynolds numbers are similar despite the effects of noise being less significant at the higher Reynolds number; on this basis, most of the discussion in this chapter focuses on the q''_{lc} distributions for the large Reynolds number tests solely as the trends seen for the lower Re tests are similar. Once again the trends seen in the q''_{lc} distributions in figure 5.3 and figure 5.4 are also seen for the single 610 μm diameter jet and so the discussion of these trends can be found in section 5.2.
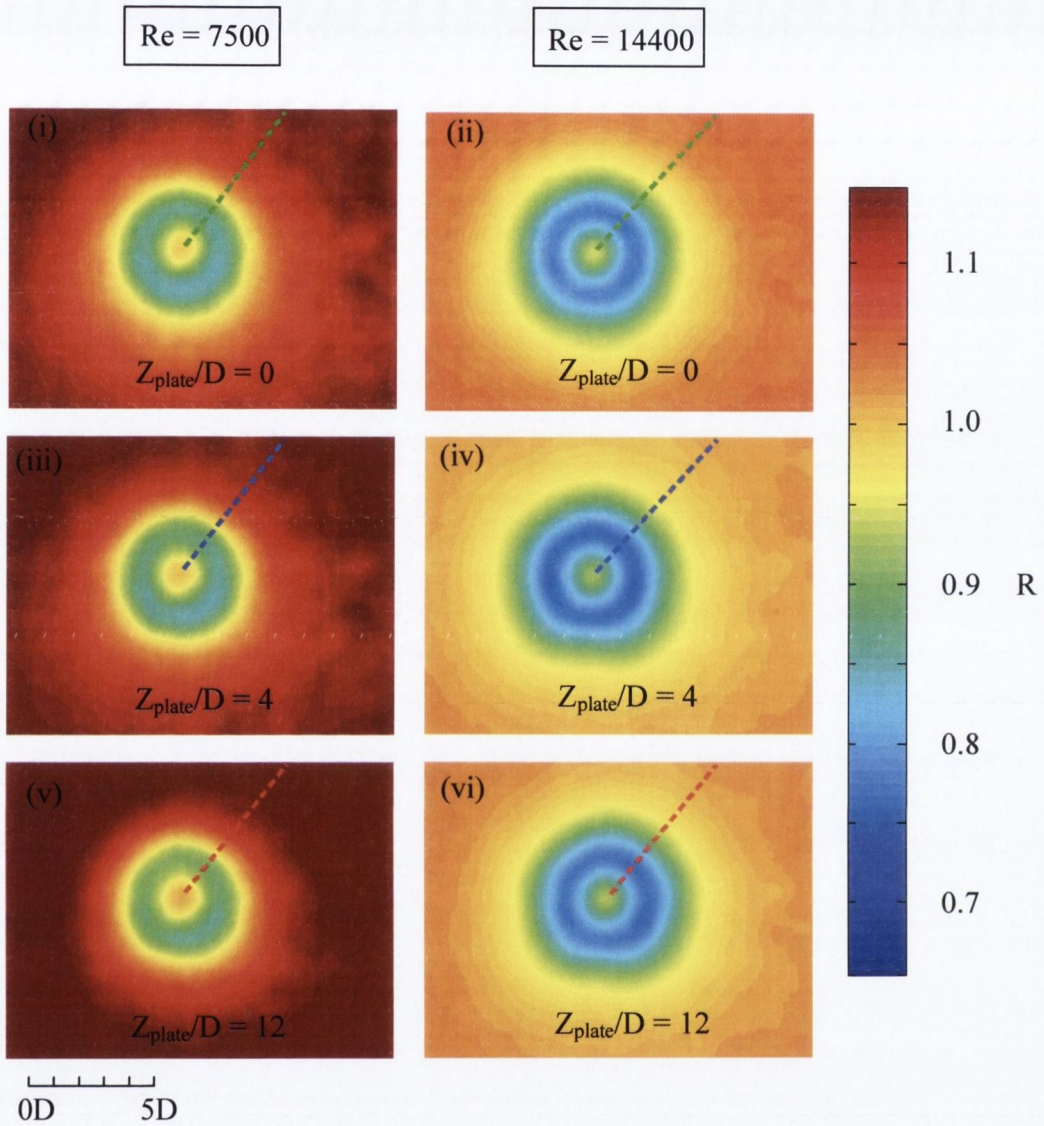
Figure 5.1, Recovery factor distributions resulting from a single 910 μm diameter jet at various confinement levels, Z_{plate}, and at Re values of 7500 and 14400.
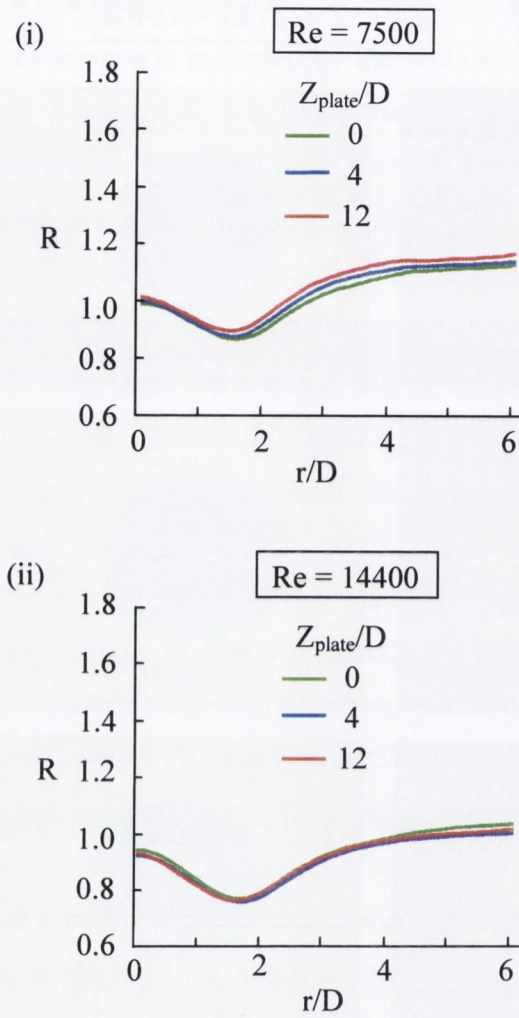
Figure 5.2, Cross sections of recovery temperature distributions corresponding to a single 910 μm diameter jet at various confinement levels, Z_{plate}, and at Re values of 7500 and 14400.
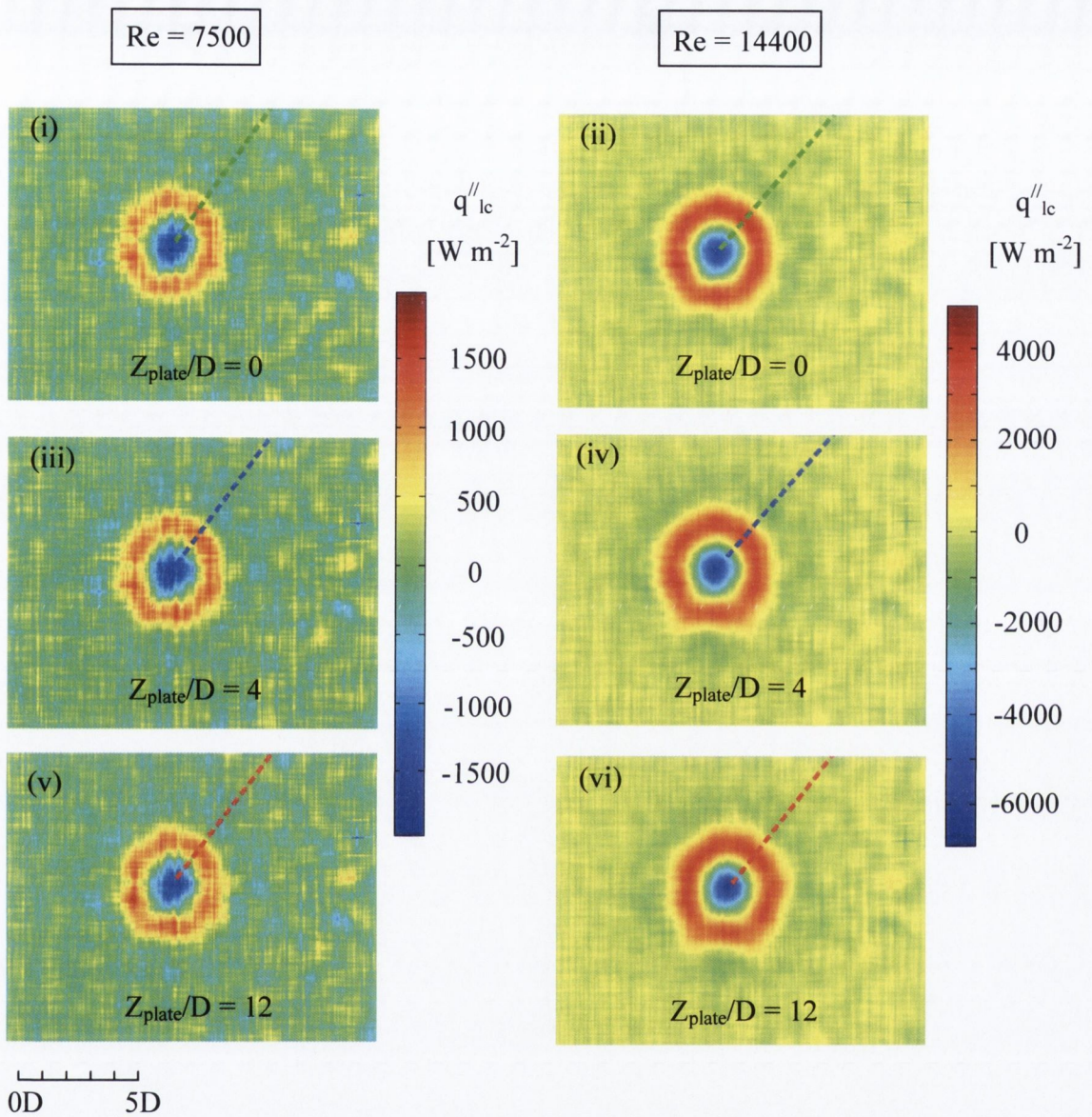
Figure 5.3, Lateral conduction distributions corresponding to a single 910 μm diameter jet at various confinement levels, Z_{plate}, and at Re values of 7500 and 14400.

(i)

Re = 7500

(ii)

Re = 14400
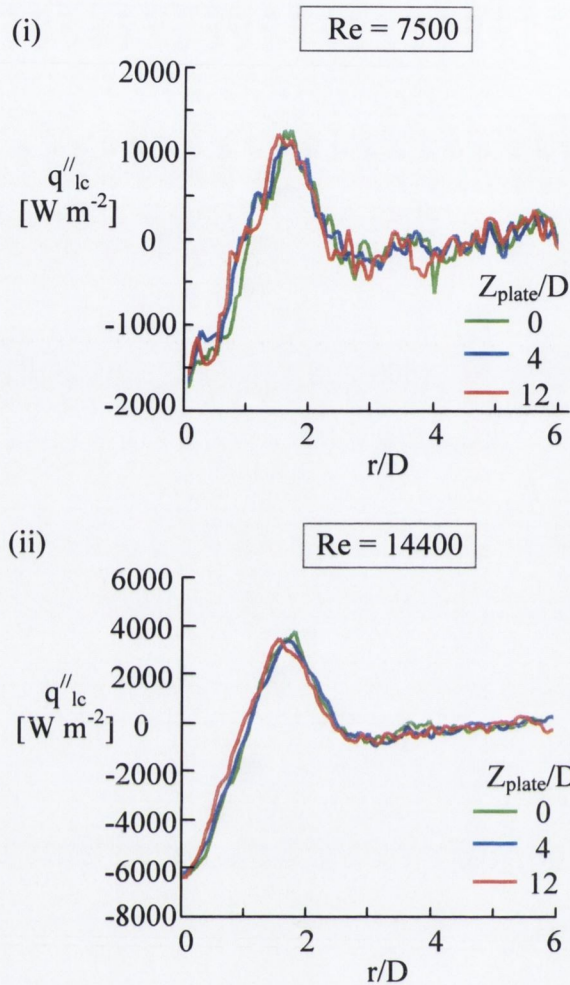
Figure 5.4, Cross sectional lateral conduction distributions corresponding to a single 910 µm diameter jet at various confinement levels, Z_{plate}, and at Re values of 7500 and 14400.

5.2 SINGLE JET

The single jet study is performed on a 0.61 mm diameter jet. The data recorded for this jet are independent of the crossflow effects seen in the multiple jet studies. As a result these results are later used to interpret the effects of crossflow from multiple jet interactions. Firstly the effects of H/D on R are studied by fixing the jet Reynolds number and varying H/D through values of 0.6, 1, 2, 3, 4 and 5. This is done for a Reynolds number of 5100, shown in figure 5.5 and then for a Reynolds number of 10500, detailed in figure 5.6. The value of Z_{plate} is fixed at zero for this study. The effect of nozzle to impingement surface spacing on recovery factor is found to be significant for all the jet configurations studied

which is consistent with the findings of Goldstein et al. (1986). The general trend observed is that as H/D is increased the recovery factor is also increased, so lower values of H/D result in a cooler surface. Furthermore, it is found that changing H/D alters the shape of the recovery distribution. Recovery factor distributions at all H/D values show a local maximum at the jet's stagnation point and demonstrate a minimum at an annulus surrounding the jet's centre, figure 5.6. The minimum may be attributed to the vortical flow structures that are discussed in chapter 2. Thus, Meola and Carlomagno (2004) noted the occurrence of this minimum at r/D = 1.2; however, in the current investigation this minimum is evident at r/D ≈ 1.4. The slight difference in this location for the two tests may be as a result of different nozzle exit conditions. The minima in the recovery factor distributions show lowest magnitudes at small nozzle to plate spacings. At H/D = 0.6 the temperature gradients at these minima are steepest [figure 5.6 (vii)] and consequently large amounts of heat are removed from this region; as indicated by the maximum magnitude of lateral conduction in figure 5.8 (vi). As H/D increases the minima in the recovery factor distribution at r/D = 1.4 become less apparent due to the break down of the primary vortical rings at larger H/D values, Fox et al. (1993). The decrease in this temperature minima leads to a decrease in the maximum value of q''_{lc}.

Looking at the recovery factor distribution for H/D = 0.6, figure 5.6 (vii), one can see that the temperature gradients at radial locations on either side of r/D of 1.4 look similar, which suggests that the amount of heat moving from the warm region of r/D < 1.4 into the cool region of r/D = 1.4 is the same as the amount of heat moving from the warm region r/D > 1.4 into the cool region of r/D = 1.4. However, the area of the warm region of r/D < 1.4 is much less than the area of the warm region of r/D > 1.4. This means that q''_{lc} values are much less for r/D < 1.4 than for r/D > 1.4. Figure 5.8 (vii) shows that q''_{lc} for r/D < 1.4 decreases to a negative magnitude of -15000 Wm^{-2}, while for r/D > 1.4 the lowest value of q''_{lc} is -1500 Wm^{-2}. The ability of the jet to remove 15000 Wm^{-2} from the stagnation point region demonstrates the great potential for the use of this conjugate heat transfer method in the cooling of localised hot spots in electronic components. At the centre of the jet, r/D = 0, the recovery factor is a local maximum and increasing H/D to around 4 causes the stagnation point recovery to become an absolute maximum, which agrees with the findings of Goldstein et al. (1986). At small H/D spacings two negative regions are present in the

q''_{lc} distribution: a primary negative region at the jet's centre and a secondary negative zone located away from the jet's centre. However, as H/D increases the secondary negative region diminishes and this region eventually disappears at H/D = 4.

The occurrence of the local maximum at the jet's centre is caused by temperature recovery as the jet is stagnated. Another contributing factor to this maximum at the jet's centre may be energy separation, in respect of which Fox et al. (1993), figure 2.20, discussed how a vortex produced in the jet's shear layer can produce warm fluid near the core of the jet. Looking at the different recovery distributions in figure 5.5 one can see that at H/D = 0.6 and H/D = 1, figure 5.5 (i) and (ii), the cooling that occurs at the local minimum is quite localised whereas for H/D > 1 the cooling effect at the recovery factor minimum is spread out over a larger area. As H/D is increased the jet has more pre-impact interaction with the surroundings. Keeping in mind the jet's static temperature is reduced when the fluid is moving at such high velocities, the more the jet interacts with the relatively warm ambient air the warmer the jet will become. Beyond r/D ≈ 4.4 the change in temperature gradients with respect to radial distance is quite small, figure 5.6 (vii) and so the lateral conduction distribution for r/D > 4.4 is at a constant value of approximately zero (neglecting noise). The far field recovery temperature of the jets placed at larger H/D spacings is generally greater than the recovery temperature of the jets placed nearer to the surface. This may occur as a result of the amount of heating/cooling that occurred in the earlier development of the jet. At the edge of the distributions shown in figure 5.5 and 5.6 the magnitudes of recovery, R, are still increasing with r/D, which is consistent with trends seen by Goldstein et al. (1986). Goldstein et al. (1986) also noticed that the recovery factors at large r/D values converged to unity and reported R to be independent of Re. Figure 5.9 shows measured recovery factors for H/D values of 1 and 5 and Reynolds numbers of 5100 and 10500. The recovery factor of the larger Reynolds number jet approaches unity for large Re values. However, at lower Reynolds numbers the recovery factor is larger than unity. The general shape of the recovery distribution at different Reynolds numbers is similar. Even still, the recovery factor for the low Reynolds number jet is always higher than that for the high Reynolds number jet. It is expected that the offsets in recovery distribution at different Re values are largely caused by the increased significance of the numerator in equation 5.1 at lower Re values. This may be explained by noting that the errors associated with the

temperature measurements from the IR camera and the plenum thermocouple are 0.21 ^{0}C and 0.18 ^{0}C, chapter 4. A temperature difference of 0.39 ^{0}C in equation 5.1 corresponds to recovery factor values of 1.05 and 1.014 for Re values of 10500 and 5100. These magnitudes give an indication of how the recovery factor associated with the lower speed jet is more sensitive to temperature error than the recovery factor values evaluated at the larger temperatures.
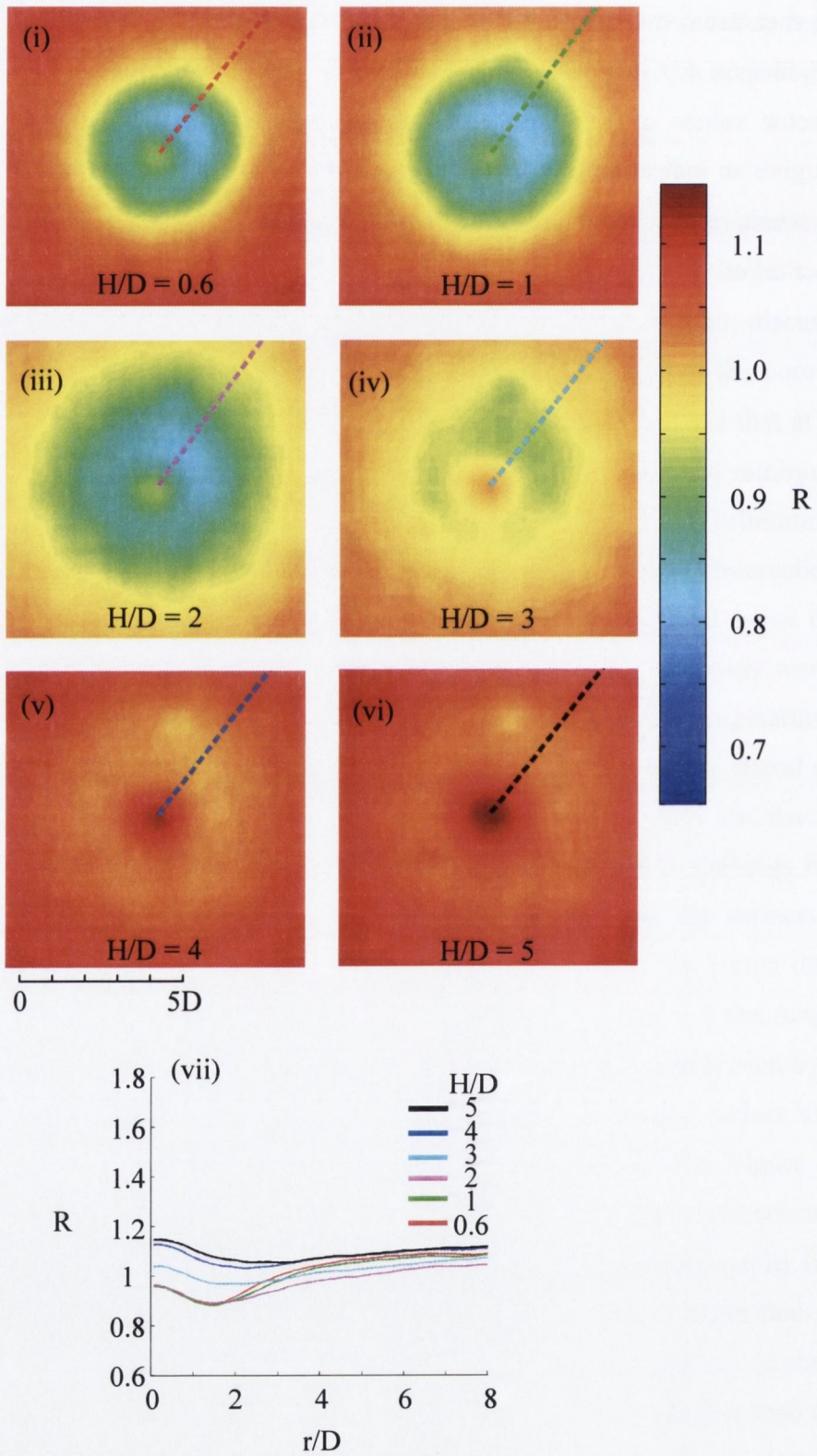
Figure 5.5, The effects of H/D on recovery factor for a single 610 µm diameter jet at Re = 5100.

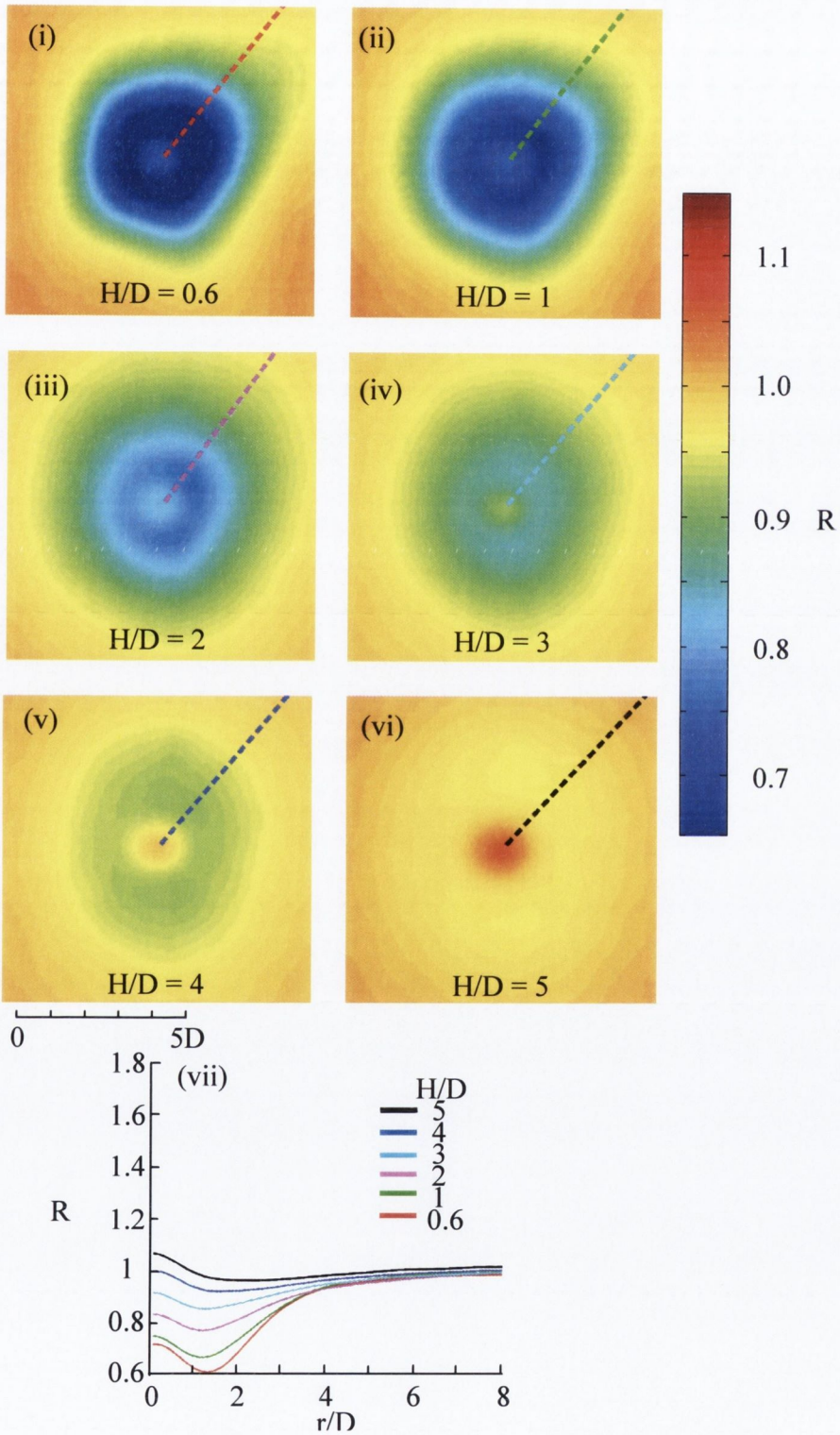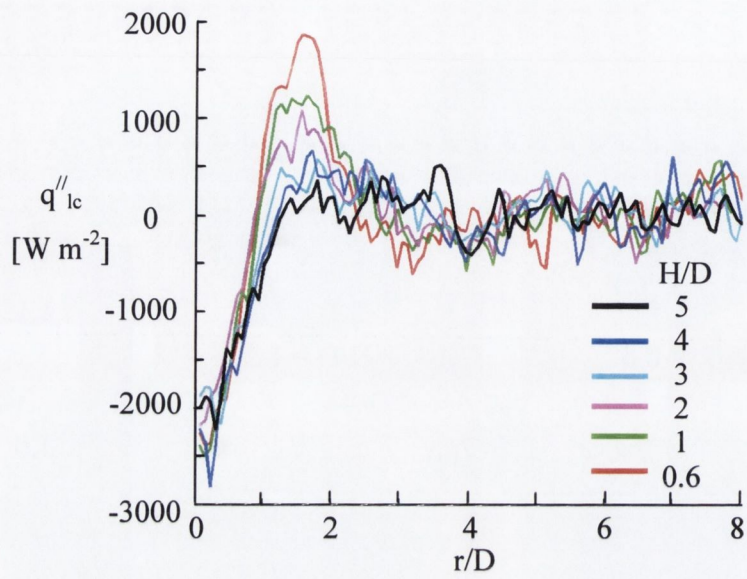*Figure 5.6, The effects of H/D on recovery factor for a single 610 μm diameter jet at Re = 10500.*

Figure 5.7, Lateral conduction distributions corresponding to the recovery factor data in figure 5.5 (vii).
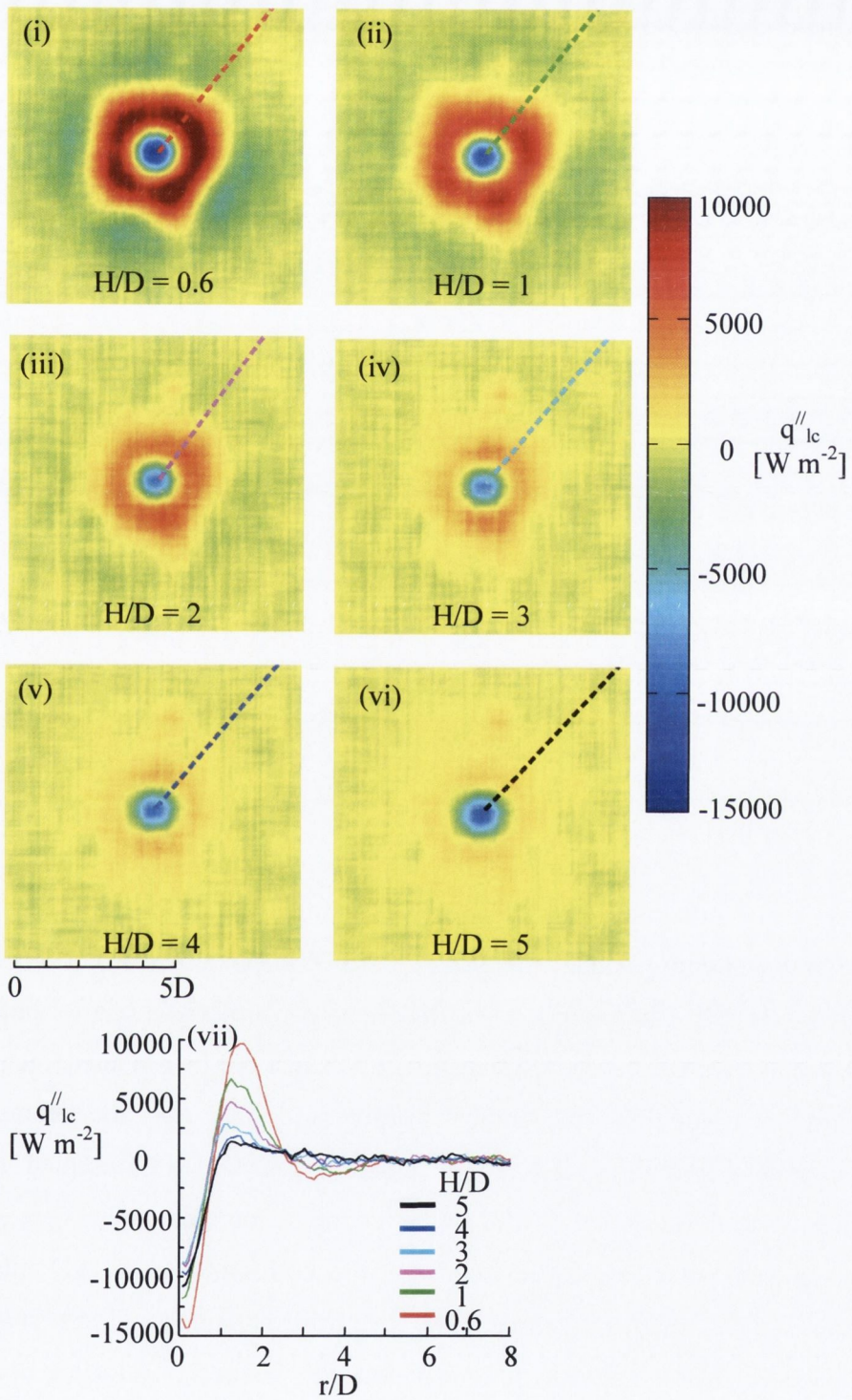
Figure 5.8, The effects of H/D on lateral conduction for a single 610 μm diameter jet at Re = 10500. The distributions shown in this figure correspond to the temperature distributions shown in figure 5.6.
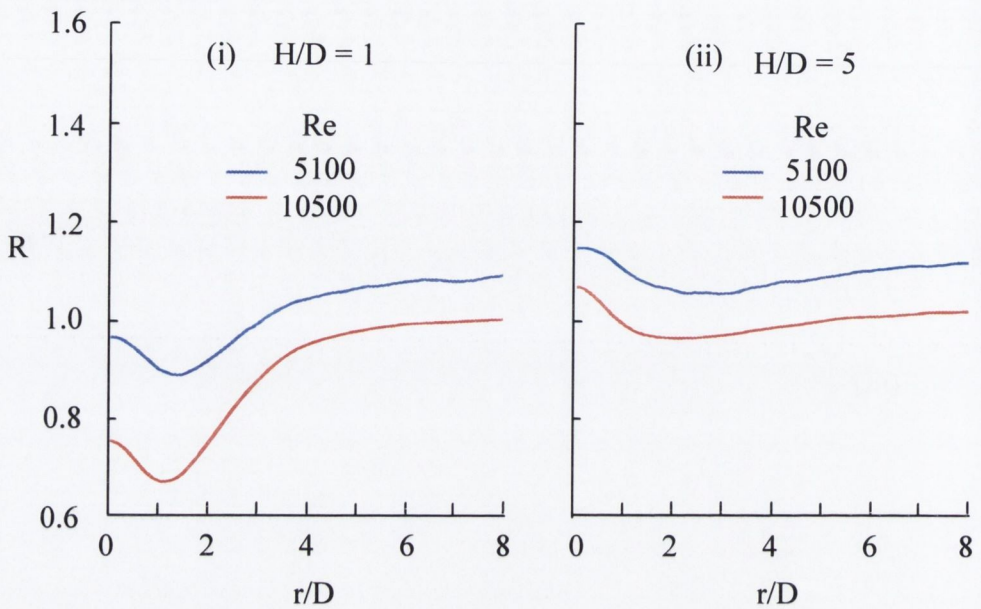
Figure 5.9, Recovery factor distributions corresponding to temperature data in figures 5.5 and figure 5.6.

5.3 MULTIPLE JETS

The recovery factor distributions associated with multiple jets differ from those seen for a single jet due to multiple jet interactions, as described in section 2.4.2. In this section the effects of H/D, Re, S/D and number of jets on R and q''_{lc} are considered for both, 2×2 and 3×3 jet arrays. Jet centre to centre spacings of 2.5, 4 and 6 are investigated, meaning that 6 different array configurations are studied. Further information on the geometry of the nozzles is contained in section 3.1.1. The results in this section are presented in a slightly different manner to those shown for the single jet and as more parameters are studied, for ease of comparison of the results, only surface plots corresponding to H/D values of 1, 3 and 5 are shown. (A full index of temperature plots corresponding to all tests studied can be found in appendix C.) Furthermore, common scales for recovery factor are used over the entire range of data presented. The results are shown at the end of this section as follows; at a Reynolds number of 5100, the results are shown for the 2×2 jet configuration in figure 5.10 and figure 5.11, and the 3×3 array jet configuration results are presented in figure 5.14 and figure 5.15. At Re = 10500, the results are shown for the 2×2 jet configuration in figure

5.12 and figure 5.13, and for the 3×3 array jet configuration results are presented in figure 5.16 and figure 5.17. The centre of each array configuration is located at r/D = 0 on the cross sectional plots. In the 2×2 jet array configuration no jet exists at r/D = 0. As r/D is increased the cross sectional distributions pass through a single stagnation point associated with the top right jet in the 2×2 array configuration. The geometrical centre of this top right jet is indicated by the vertical dashed line in the cross sectional distributions. The cross sectional distributions associated with the 3×3 jet array, figure 5.15, show two stagnation points. The central jet is located at r/D equal to zero and the geometrical centre of the peripheral jet is once again indicated by the dashed vertical line.

Two values of Reynolds numbers were investigated for the multiple jets study; Re = 5100 and Re = 10500. A comparison of the cross sectional distributions for the 2×2 array configuration at the two Re values is achieved by comparing distributions in figure 5.11 to distributions in figure 5.13. Some small variations exist between the two sets of data and will be discussed later in this section. Generally the two sets of distributions are quite close to being indistinguishable; signifying that R is independent of Re. Investigating the effects of Reynolds number for the 3×3 array configuration is achieved by comparing figure 5.15 to figure 5.17. Distributions for both the Re = 5100 and Re = 10500 tests show similar trends, but as is the case for the single jet, some of the recovery factor distributions for the Re = 5100 tests have higher values than for the Re = 10500 tests. It is expected that this offset that occurs between the recovery factor distributions at the different Reynolds numbers is due to the increased sensitivity of R to temperature error at low speeds, as discussed in section 4.1. The magnitudes of lateral conduction heat flux for the multiple jets are similar to the magnitudes seen for the single jet. For the multiple jet study at the Reynolds number of 5100, noise is once again quite evident in the q''_{lc} distributions, as can be seen from figure 5.18. The effect of Reynolds number is considered by comparing the cross sectional distributions at Re = 5100 shown in figure 5.18 with the cross sectional distributions at Re = 10500 shown in figures 5.20 and 5.22. This comparison indicated similar findings to the single jet study; the magnitudes of q''_{lc} for the Re = 10500 tests are approximately three times the magnitudes shown for the Re = 5100 test but similar trends are seen when distributions at the two Re values are compared to one another, suggesting

q''_{lc} can be scaled with Re. As similar trends exist for both Re values this discussion mainly focuses on heat flux due to lateral conduction for the Re = 10500 tests.

Examination of the recovery factor distributions in these figures indicates that some of the distributions are non-symmetric. Thus, considering the left hand side of figure 5.14 one can see that at H/D = 1, figure 5.14 (i) and at H/D = 5, figure 5.14 (vii), the figures show good symmetry; however, this symmetry is not as evident at H/D = 3, figure 5.14 (iv). These variations in symmetry may be caused by small variations in the nozzle geometries that results in more rapid development of some jets compared to others at various H/D levels. This trend can be seen more clearly by observing individual jets in figure 5.14. The top left jet in figure 5.14 (iv) shows a similar recovery factor to the top left jet in figure 5.14 (vii) whilst the recovery factor for the bottom right jet in figure 5.14 (iv) resembles more the bottom right jet in figure 5.14 (i). Thus, as H/D is increased from a low value the disappearance of the recovery minimum surrounding a jet and the increase of the recovery maximum at a jet's stagnation point occurs more rapidly in some jets than in others.

For a single jet a local maximum in recovery factor occurs at the geometrical centre of the jet and a cool annulus is located around the centre of the jet. The associated heat flux due to lateral conduction distributions demonstrated a minimum at the jet's stagnation point and an annulus of high heat flux surrounding the centre of the jet. These general characteristics were observed for all the individual jets in the array study, though multiple jet interactions altered the recovery factor and heat flux due to lateral conduction distributions for the array data. Looking at the cross sectional array distributions, one of the most noticeable observations is that the maximum in the recovery temperature, and the minimum lateral conduction value, that is associated with the stagnation point of a peripheral jet, occurs at r/D values greater than the geometric centre of the peripheral jet. (The geometrical centres of the peripheral jets are denoted by a dashed vertical line). For the 2×2 array, figure 5.11 (i), (ii) and (iii) shows the occurrence of the peripheral jet's stagnation point beyond the geometrical centre of the jets. This finding is consistent with the findings of Goldstein and Timmers (1982) who noticed that the maximum heat transfer coefficients of peripheral jets did not occur at the geometric centres of the jets due to cross flow. Looking at the recovery distributions in figure 5.11, one can see that the offset distance between the local maximum

recovery factor and the geometrical centre of a peripheral jet increases with increasing S/D and the offset difference is relatively independent of H/D for Re = 5100. As Re is increased to 10500 for the 2×2 array, figure 5.13, this offset distance is once again independent of H/D for the jet centre to centre spacing of 2.5. However, as S/D is increased to 6, the offset distance now increases with increasing H/D, which is expected as the cross flow resulting from higher Reynolds number jets is stronger and with increasing H/D values there is more interaction between the pre-impact jet and the surrounding fluid in cross flow. For the 3×3 jet array at Re = 5100 and Re = 10500, figure 5.15 and figure 5.17, the offset does not follow exact trends but the general trend is that the offset is independent of H/D up to H/D = 3 and for greater H/D values the offset distance increases. The occurrence of an increase in the offset distance for the 3×3 jet array at increased H values for Re = 5100 may be attributed to the increased cross flow effect caused by the larger number of jets in the configuration as the offset distance in the 2×2 jet array for Re = 5100 was independent of H/D.

As stated earlier for a single jet, a cool temperature annulus is formed around the high temperature region associated with the jet's stagnation point as a result of compressibility effects and the formation of vortical structures surrounding a jet. These cool regions are evident in the recovery factor distributions from multi jet arrays; however multiple jet interactions alter the symmetry of these cool regions surrounding individual jets contained within an array. Looking at all the recovery factor distributions for the 2×2 array configuration, at Re = 5100, in figure 5.10, it is evident that the S/D = 6 spacing distributions resembles most closely the recovery factor distributions of a single jet, as the S/D = 6 distribution is mostly symmetric about its stagnation point. (The stagnation point is considered as the point close to the jet's geometric centre where the local maximum in recovery factor occurs.) With the S/D = 6 distributions, the recovery temperatures are slightly non-symmetric as the temperature minima in the inner region of the array are lower than the temperature minima at the other region, figure 5.11 (iii). The heat fluxes due to lateral conduction distribution that corresponds to recovery factor distributions in figure 5.13 (iii) are shown in figure 5.19 (iii). The effects of slightly lower recovery temperatures at the inner region of the array cause larger magnitudes of q''_{lc} at the inner maximum of the q''_{lc} distribution compared to the outer maximum of the q''_{lc} distribution. As S/D is

decreased to S/D = 4 the effects of multiple jet interactions are increased and a warm region occurs between the centres of multiple jets as a result of the collision of the wall jets from neighbouring jets. This collision results in the generation of a secondary stagnation region between the jets; this can be seen in figure 5.10 (ii) at the centre of the jet array configuration for the 2×2 array at H/D = 1 and at a Reynolds number of 5100. The effects of varying H/D for these test parameters can be seen in figure 5.11 (ii). In these recovery temperature distributions, a minimum occurs either side of the stagnation point but the temperature minimum for r/D values greater than the jet's stagnation point is always less than the temperature minimum towards the centre of the jet configuration. This occurs as the flow in the centre of the jet array is stagnated more with the collision of the wall jets and the interaction with the outwash flow. This warmer region at the centre of the jet array also occurs for the 2×2 array at the higher Reynolds number of 10500. The heat flux due to lateral conduction for the 2×2 array at Re = 10500 and S/D = 4 once again shows larger magnitudes of lateral conduction in the central region of the jet compared to lateral conduction magnitudes at r/D values greater than the jet's stagnation point. Also at low H/D values the warm region at the centre of the array creates a negative heat flux region of larger absolute value than for the S/D = 6 test. The smallest S/D value studied is 2.5. Looking at the 2×2 array for Re = 5100, at H/D = 1 and at various S/D values, figure 5.10 (i), figure 5.10 (ii) and figure 5.10 (iii), one can see that at both S/D = 4 and at S/D = 6 an interaction zone exists between any two adjacent jets. In this zone the wall jets collide and secondary stagnation region is set up. Also at S/D = 4 and at S/D = 6, each of the individual jets has its own distinguishable cool annulus surrounding the jets stagnation point, but for S/D = 2.5 the cool circular annuli of the neighbouring jets overlap and result in regions that are cooler than seen for the S/D = 4 and S/D = 6 tests. Looking at figure 5.11 one can see that the warm region at r/D = 0 occurs for the various values of S/D at H/D = 0.6 but its magnitude of recovery factor is 0.85 whereas the other R values at r/D = 0 for S/D = 4 and 6 are closer to 1. The reason for this reduction in R is due to the amount of heat flux been removed as a result of the warm region at the centre of the array being enclosed by a cool temperature plate, figure 5.10 (i). This trend is also seen for the Re = 10500 test and the corresponding heat flux due to lateral conduction distribution in figure 5.20 (i) shows a negative q''_{lc} value at r/D = 0 that is almost double that seen for the S/D = 4 test. Considering all the recovery factor distributions in figure 5.11 and 5.13, one can observe

that at r/D = 0 and at H/D = 0.6 a warm region occurs. At this location the wall jets from the 4 jets collide which result in an upwash flow, figure 2.14. The stagnation of the wall jets in this region leads to the increase in temperature. After the wall jets collide the flow seeks to move upward, Geer (2003), but at low H/D values there is more restriction to the movement of the flow upward which retards the velocity of the flow in the collision region further allowing for greater temperature recovery. This may be the reason why R initially decreases at r/D = 0 as H/D is increased from 0.6 to 2 and then R increases at r/D = 0 for H/D > 2, which is evident at all S/D values studied for the 2×2 jet array.

For the 3×3 array configuration the centres of two jets are present within the cross sectional distributions shown; the central jet of the array arrangement is located at r/D = 0 and the geometric centre of a peripheral jet is denoted by a vertical dashed line. As such, the collision of the wall jets occurs between the stagnation points of the two jets. Surrounding the recovery factor of the peripheral jets at S/D = 6 are two temperature minima. The relationship between these two minima for the Re = 5100 and the Re = 10500 tests, figure 5.15 and figure 5.17 is that at low H/D values, the local minimum occurring at the outer side of the peripheral jet has a lower value than the minimum occurring at the inner side of the peripheral jet. However, as H/D is increased to a value of 2, the two minima are approximately equal. As H/D is increased further the minimum on the inside of the peripheral jet exceeds the minimum on the outside of the peripheral jet. In the heat flux due to lateral conduction cross sectional distributions for the Re = 10500, the 3×3 jet arrays with S/D = 6, the inner maximum is greater than the other maximum for all H/D values studied. This occurs as the inner q''_{lc} maximum is close to the warm region located between the centres of multiple jets. This warm region results from the collision of the wall jets from two neighbouring jets. The location of the maximum recovery temperature associated with the collision of the wall jet region for the S/D = 6 jets at the two Reynolds number values, figure 5.15 (iii) and figure 5.17 (iii), is closer to the peripheral jet than to the central jet. The location of this recovery maximum is relatively constant with variation of H/D values from 5 to 2, but for H/D < 2, the position this maximum is shifted further towards the peripheral jet. This shift in temperature maximum is attributed to cross flow. The q''_{lc} values associated with this warm temperature region is entirely negative. Comparing the stagnation recovery temperature of the central jet to the stagnation recovery of the

peripheral jet at S/D = 6 and Re = 5100, figure 5.15 (iii) shows that the recovery factor at the peripheral jet is larger than the recovery factor at the centre jet. However, when Re is increased to 10500 the trend is reversed; the stagnation recovery factor of the centre jet is greater than the stagnation recovery factor of the peripheral jet for all H/D values. For the S/D = 4 and 2.5 jets the recovery factor at the stagnation point of the central jet is generally lower than the recovery factor at the stagnation point of the peripheral jet for low H/D values. For such cases more heat is removed by lateral conduction for the central jet than for the peripheral jet. These trends seen for R and q''_{lc} are reversed for larger H/D values where the stagnation recovery factor of the central jet is greater than the stagnation recovery factor of the peripheral jet and also the stagnation q''_{lc} value of the central jet is greater than the q''_{lc} value of the peripheral jet indicating that more heat is removed from the peripheral jet.
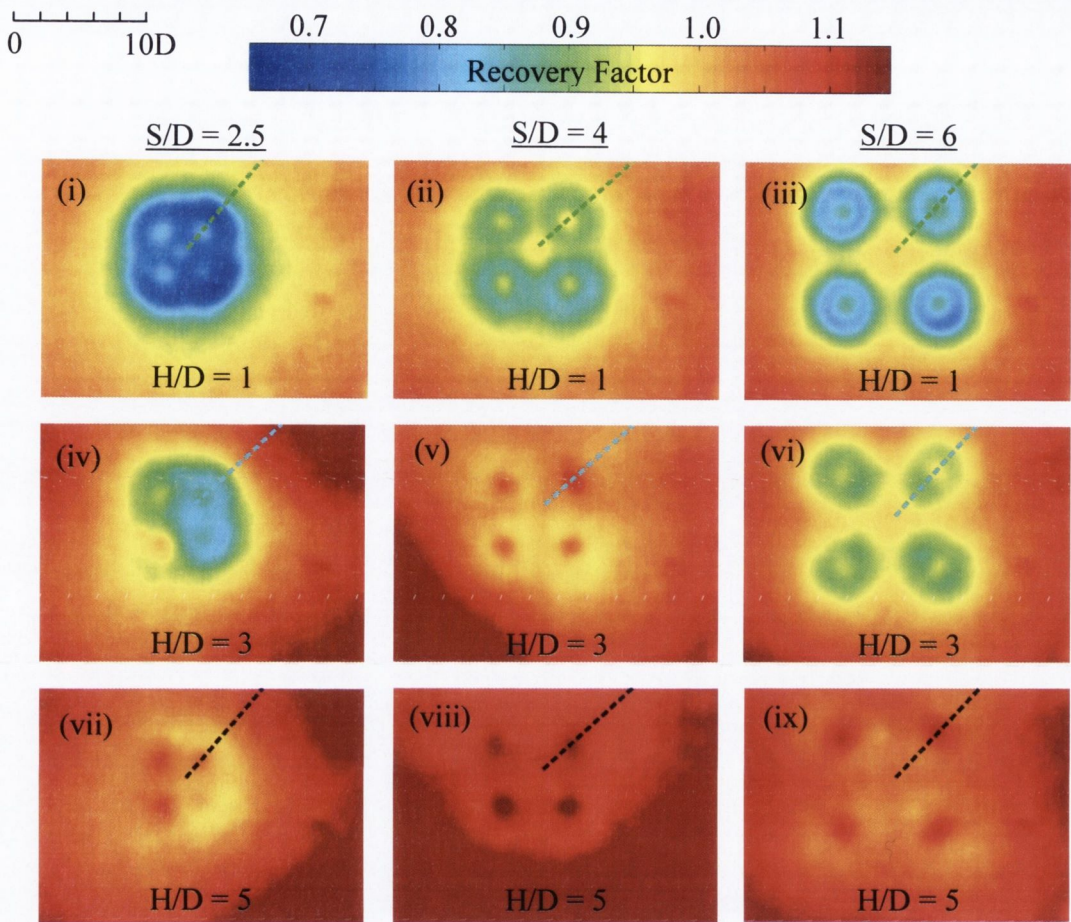
Figure 5.10, Recovery factors for a 2×2, 610 µm diameter jet array configuration at Re = 5100, H/D = 1, 3 and 5 and S/D = 2.5, 4 and 6.

Figure 5.11, Cross sections of recovery factor distributions for a 2×2, 610 μm diameter jet array configuration at Re = 5100, H/D = 0.6, 1, 2, 3, 4 and 5 and S/D = 2.5, 4 and 6.

Figure 5.12, Recovery factor distributions for a 2×2, 610 μm diameter jet array configuration at Re = 10500, H/D = 1, 3 and 5 and S/D = 2.5, 4 and 6.

Figure 5.13, Cross sections of recovery factor distributions for a 2×2, 610 µm diameter jet array configuration at Re = 10500, H/D = 0.6, 1, 2, 3, 4 and 5 and S/D = 2.5, 4 and 6.

Figure 5.14, Recovery factor distributions for a 3×3, 610 μm diameter jet array configuration at Re = 5100, H/D = 1, 3 and 5 and S/D = 2.5, 4 and 6.
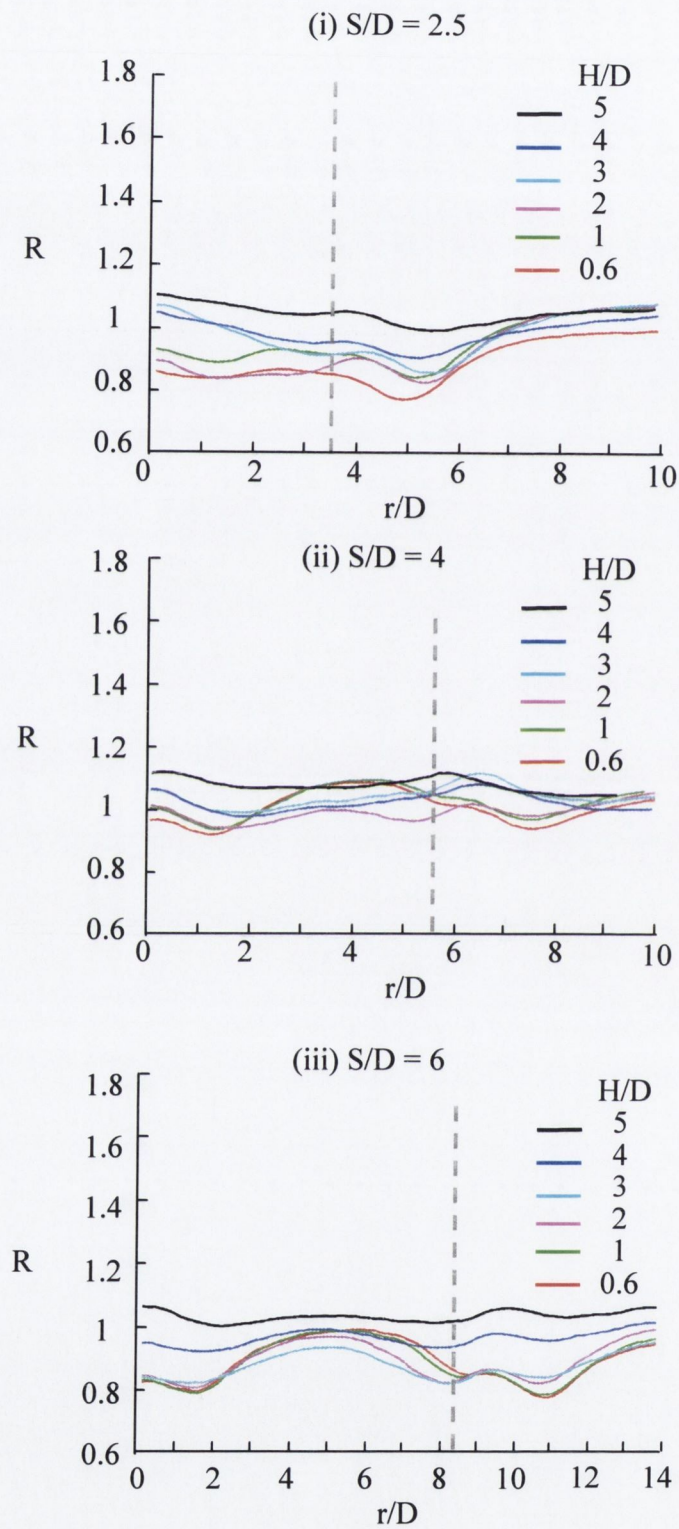
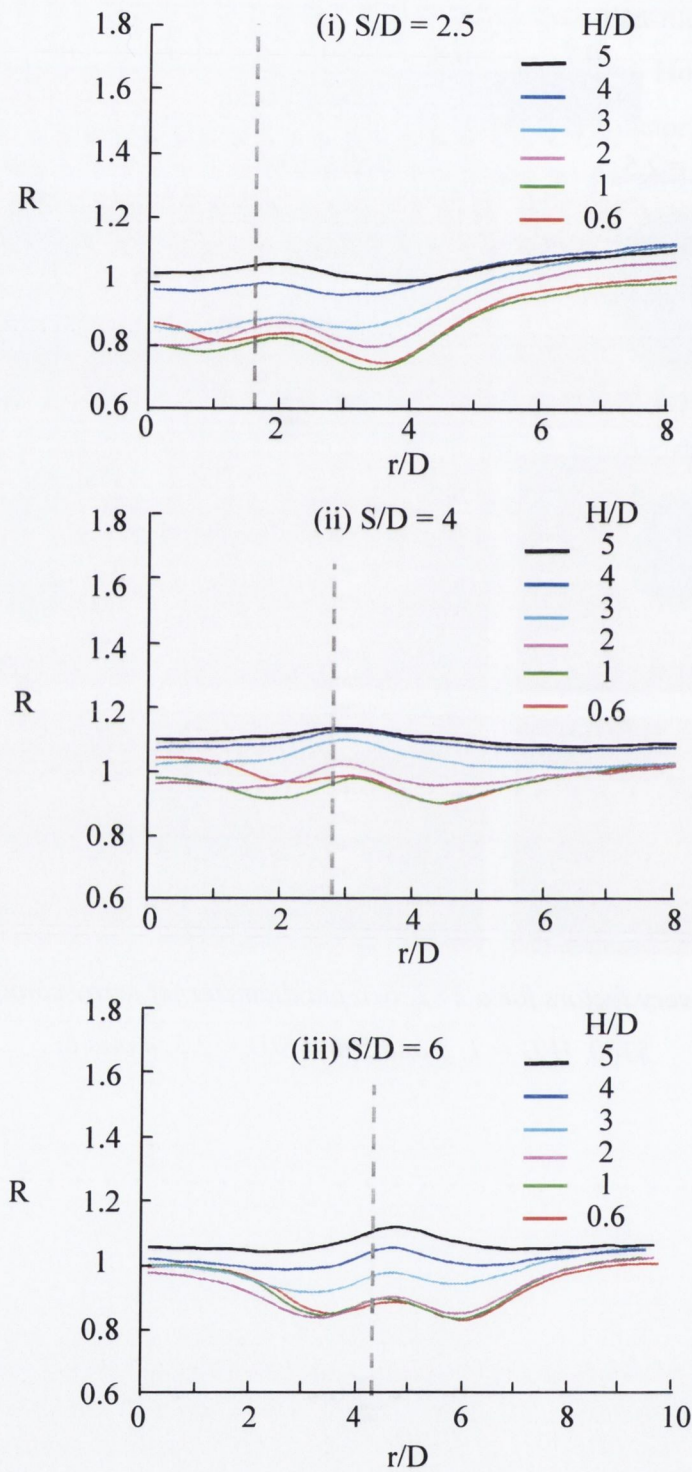*Figure 5.15, Cross sections of recovery factor distributions for a 3×3, 610 μm diameter jet array configuration at Re = 5100, H/D = 0.6, 1, 2, 3, 4 and 5 and S/D = 2.5, 4 and 6.*
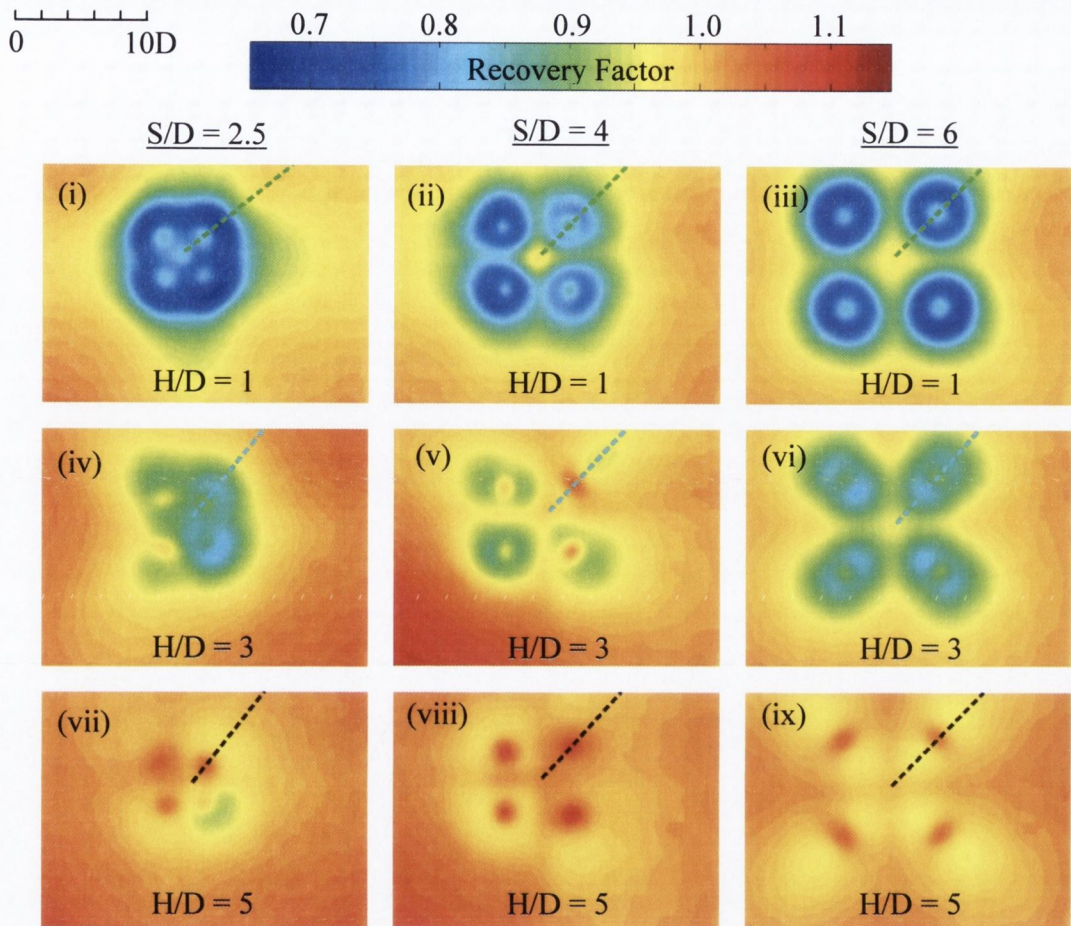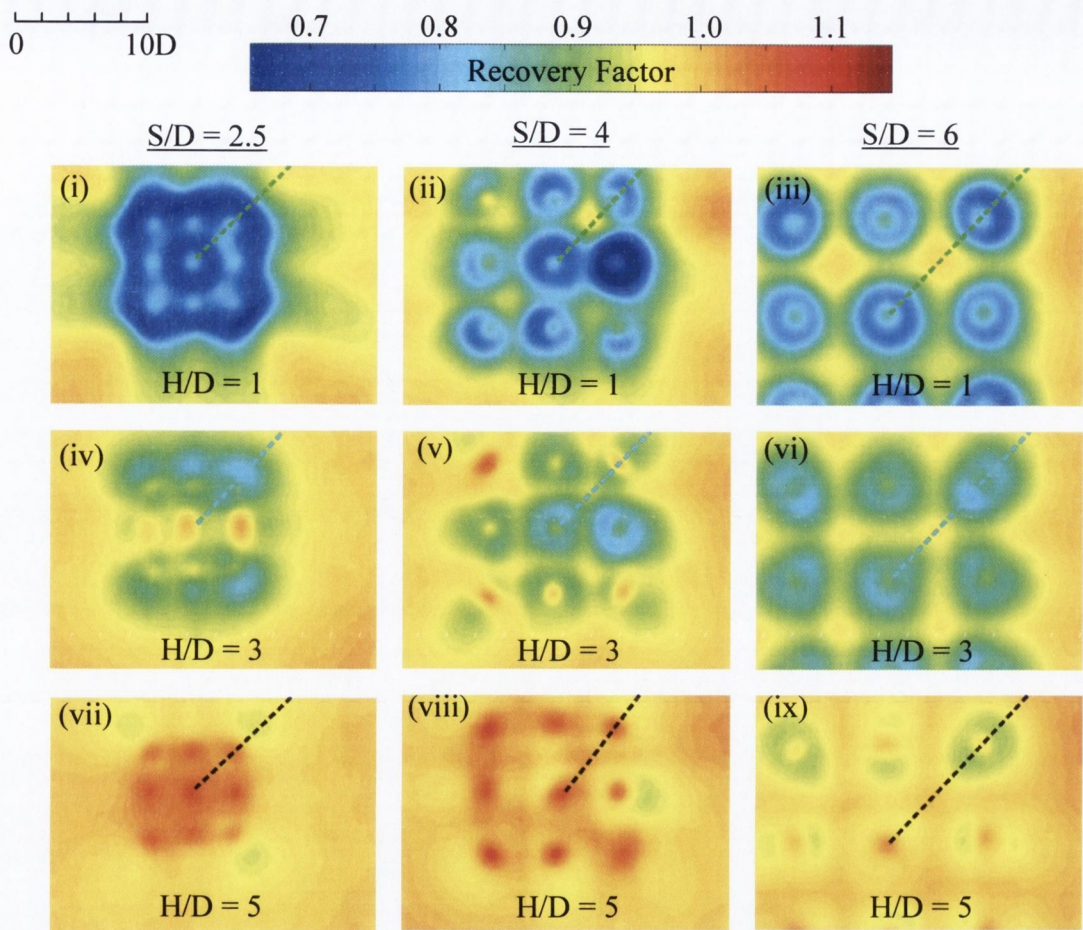
Figure 5.16, Recovery factor distributions for a 3×3, 610 μm diameter jet array configuration at Re = 10500, H/D = 1, 3and 5 and S/D = 2.5, 4 and 6.
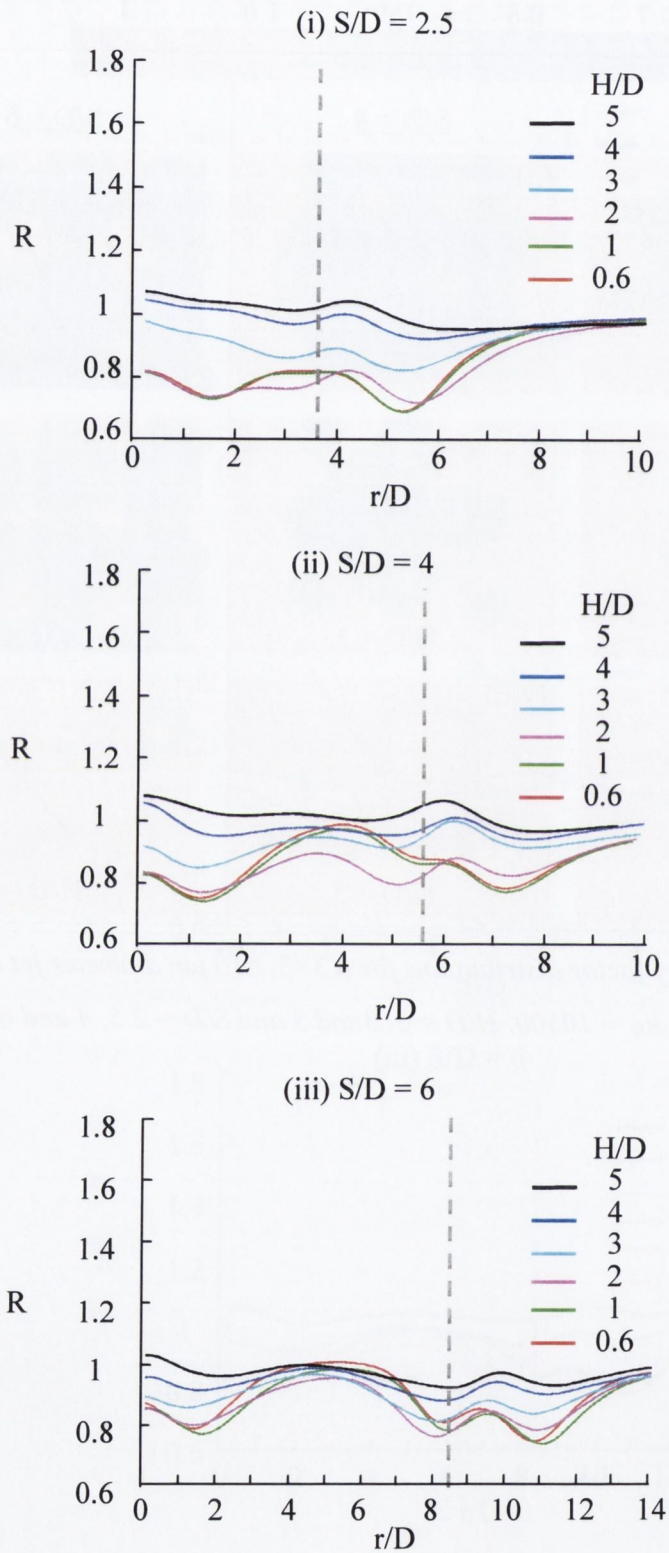
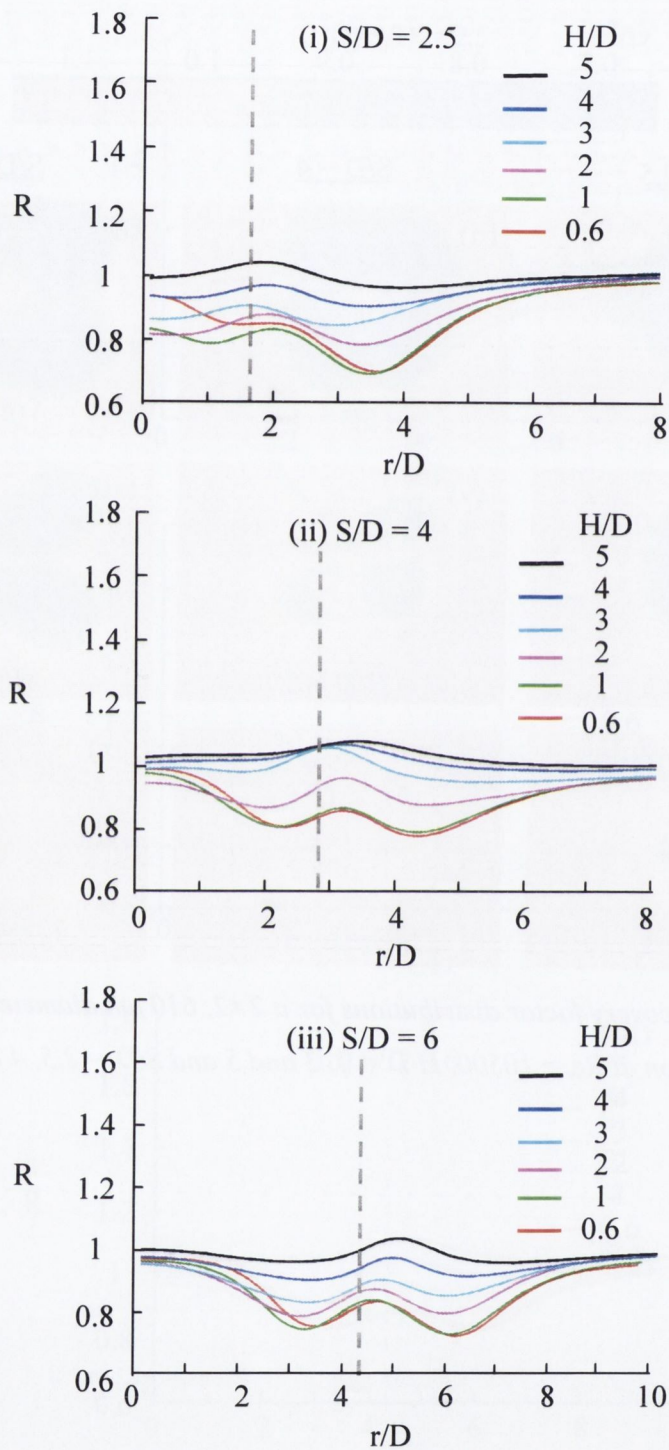*Figure 5.17, Cross sections of recovery factor distributions for a 3×3, 610 μm diameter jet array configuration at Re = 10500, H/D = 0.6, 1, 2, 3, 4 and 5 and S/D = 2.5, 4 and 6.*
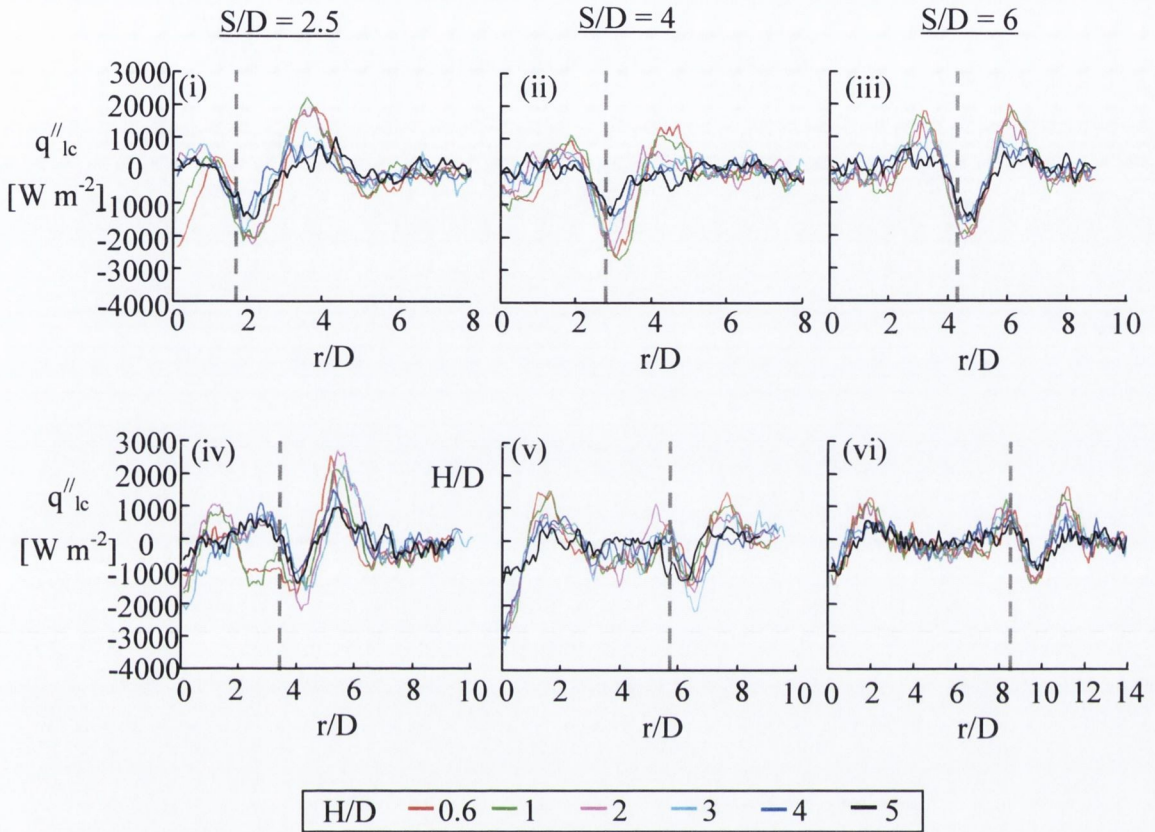
Figure 5.18, (i),(ii) and (iii) Cross sections of lateral conduction distributions for a 2×2, 610 μm diameter jet array configuration at Re = 5100, H/D = 0.6, 1, 2, 3, 4 and 5 and S/D = 2.5, 4 and 6. (iv), (v) and (vi) show tests carried out for the same parameters on a 3× 3
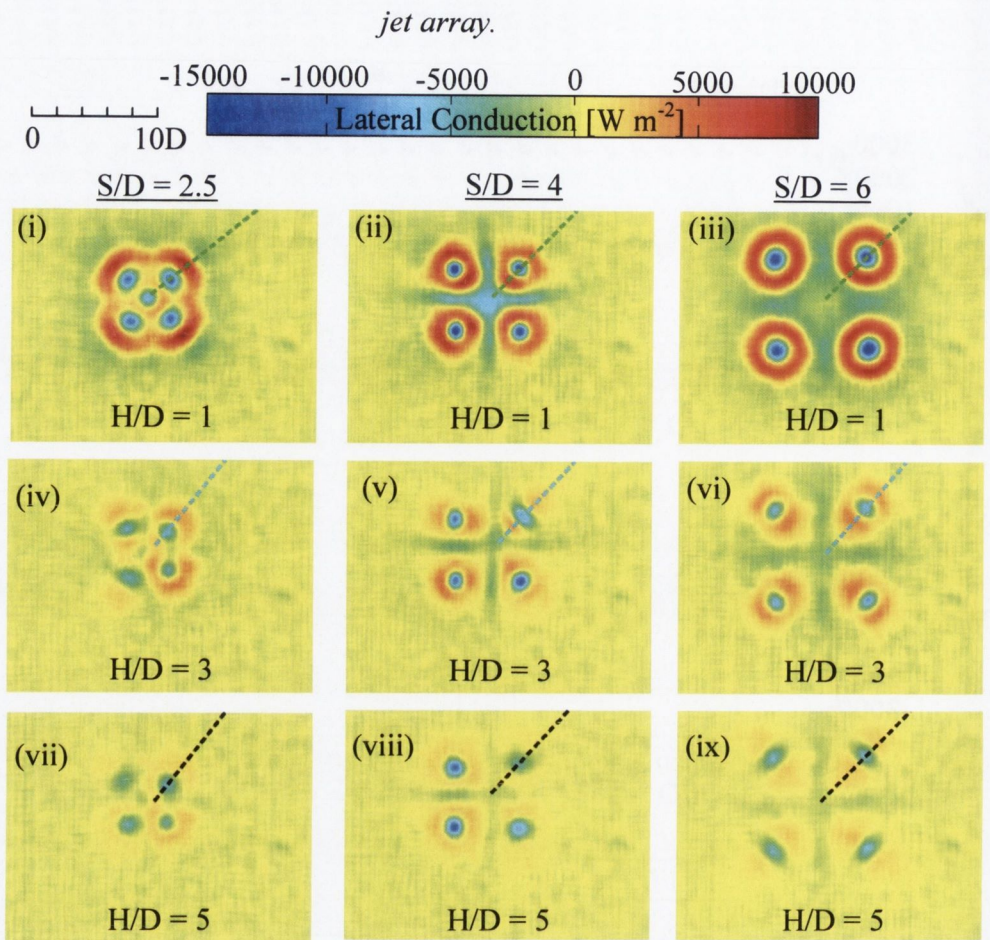
Figure 5.19, Lateral conduction for a 2×2, 610 μm diameter jet array configuration at Re = 10500, H/D = 1, 3 and 5 and S/D = 2.5, 4 and 6. The distributions shown in this figure correspond to the recovery factor distributions shown in figure 5.12.
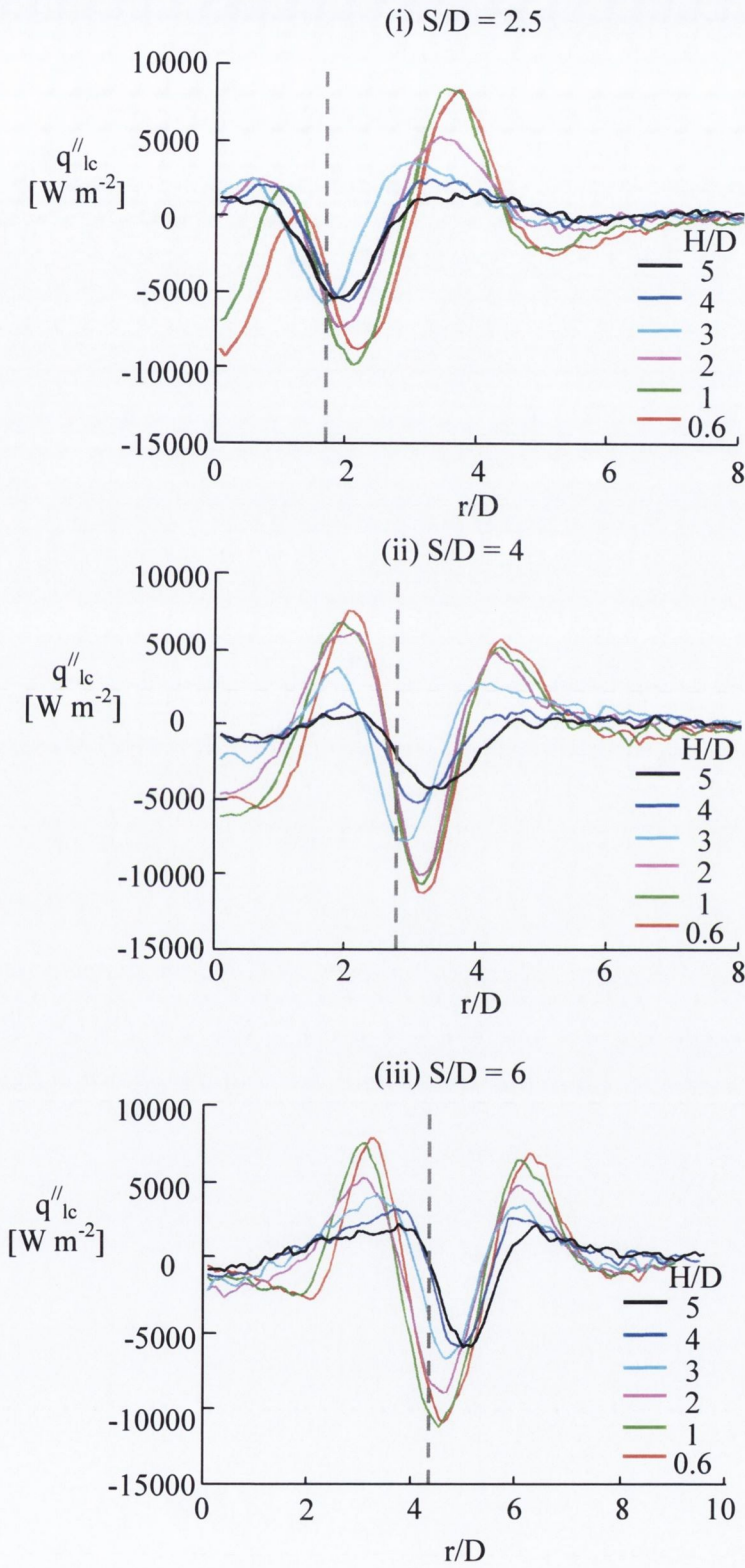
Figure 5.20, Cross sections of lateral conduction distributions for a 2×2, 610 μm diameter jet array configuration at Re = 10500, H/D = 0.6, 1, 2, 3, 4 and 5 and S/D = 2.5, 4 and 6.

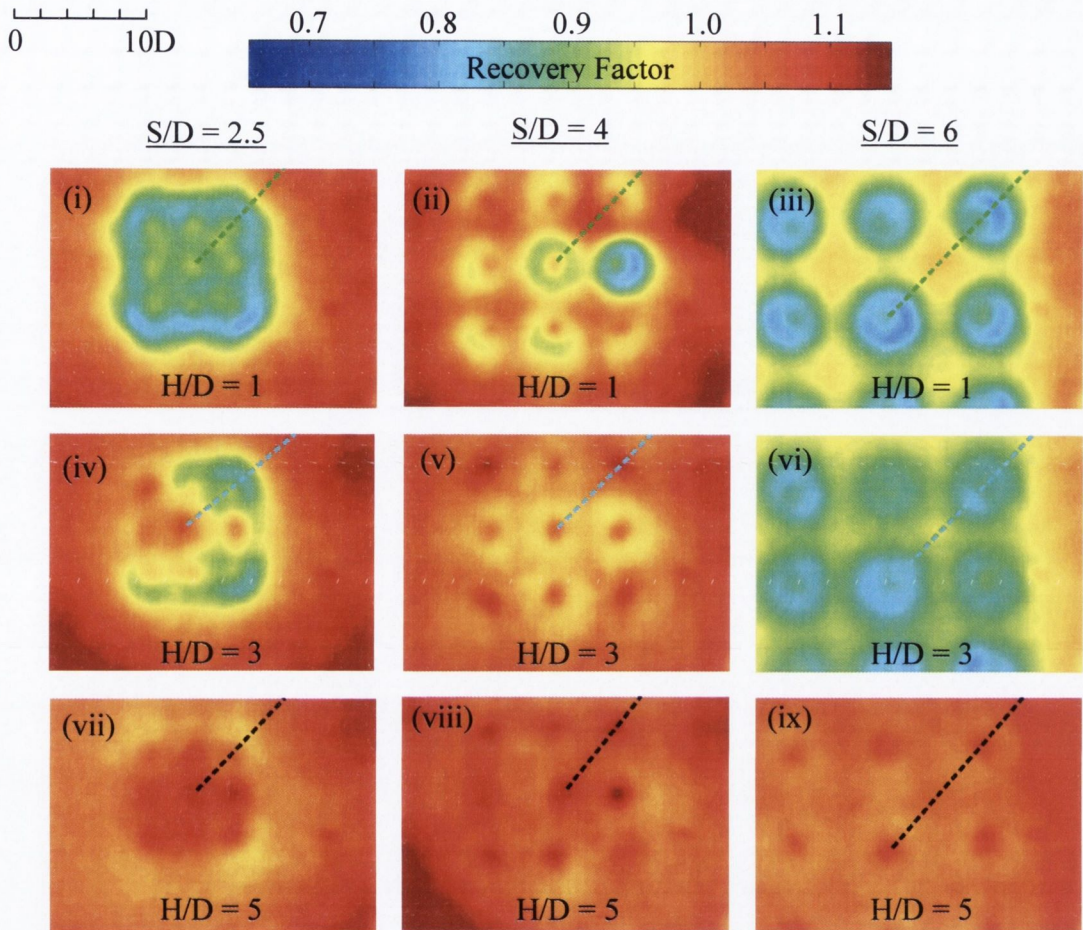*Figure 5.21, Lateral conduction distributions for a 3×3, 610 μm diameter jet array configuration at Re = 10500, H/D = 1, 3, and 5 and S/D = 2.5, 4 and 6. The distributions shown in this figure correspond to the temperature distributions shown in figure 5.16.*
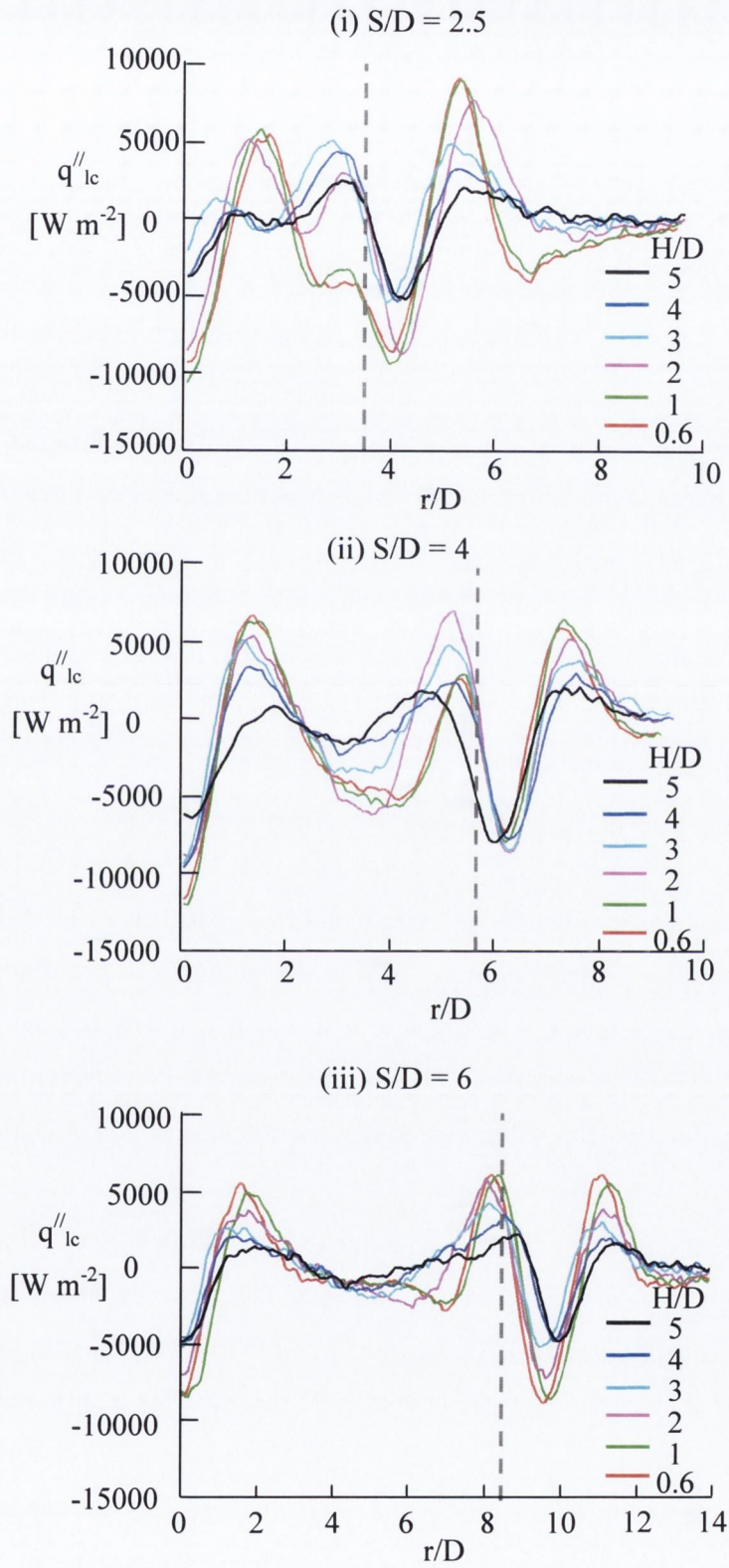
Figure 5.22, Cross sections of lateral conduction distributions for a 3×3, 610 μm diameter jet array configuration at Re = 10500, H/D = 0.6, 1, 2, 3, 4 and 5 and S/D = 2.5, 4 and 6.

6 CONCLUSIONS

6.1 CONCLUSIONS
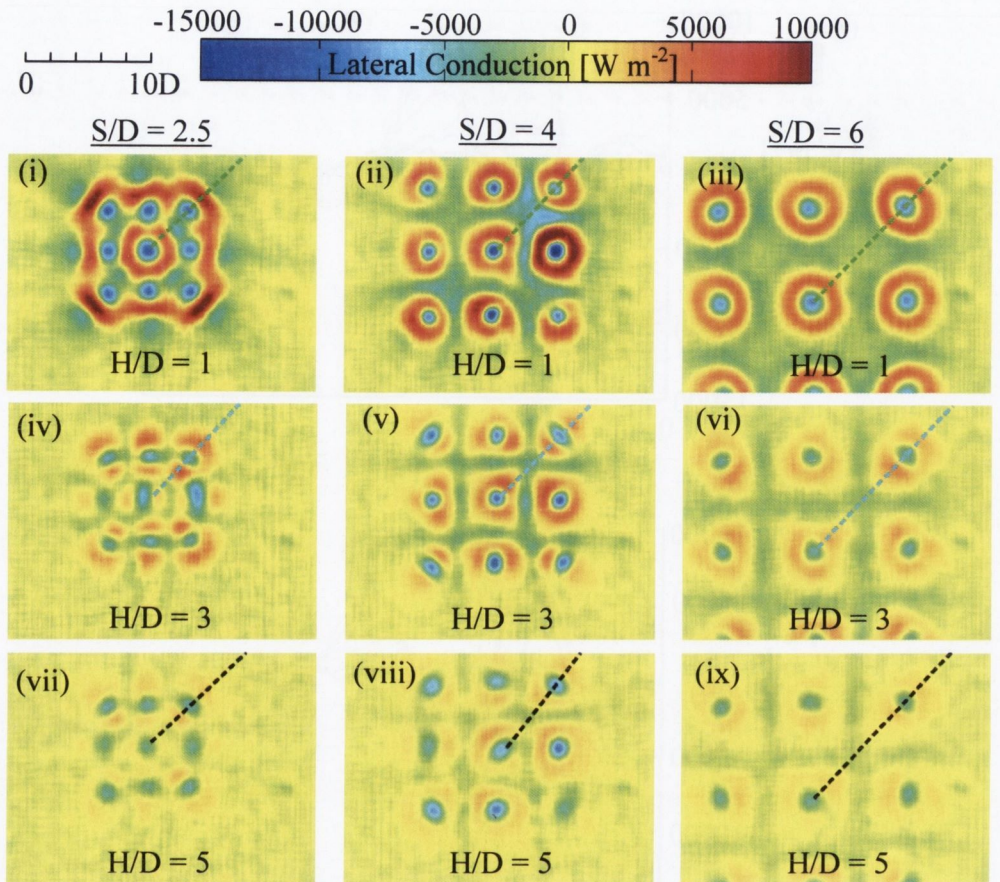
This investigation sets out to differentiate between microjet impingement and its large scale counterpart by paying particular attention to compressibility and conjugate heat transfer effects. Small diameter jets give rise to higher Mach numbers than larger diameter jets at the same Reynolds numbers. When a jet at high Mach number impinges onto an unheated surface it causes a non-uniform temperature distribution to occur on the surface. For small diameter jets the temperature gradients associated with this temperature distribution can be large enough to induce lateral conduction within the foil. This study examines and quantifies these effects in terms of recovery factor, R, and heat flux due to lateral conduction, q''_{lc}, distributions. The specific jet configurations investigated are a single jet, a 2×2 in-line jet array and a 3×3 in-line jet array; all jets are of 610 μm diameter. Experiments were performed using a thin stainless steel foil and infrared thermography at H/D = 0.6, 1, 2, 3, 4 and 5, S/D = 2.5, 4 and 6 and Re = 5100 and 10500 (Mach number of 0.36 and 0.68). A second study was also carried out using a 910 μm diameter jet to study the effects of flow confinement resulting from the small gap between the nozzle plate and the impingement surface. Reynolds number of 7500 and 14400 (Mach number of 0.36 and 0.64) were investigated at H/D = 1 and at confinement levels of 0 D, 4 D and 12 D.

- Results for the single 610 μm diameter jet showed the effect of nozzle to impingement surface spacing on recovery factor to be significant. R generally increases with increasing H/D. At low H/D, the recovery distributions show a local maximum at the jet's stagnation point and demonstrate a minimum at an annulus surrounding the jet's centre at r/D ≈ 1.4. For r/D > 1.4 the surface temperature approaches ambient temperature. As H/D is increased the surface temperature at the jet's centre increases and for H/D of around 4 the stagnation point recovery factor becomes an absolute maximum. Also, as H/D increases the minimum in recovery at r/D ≈ 1.4 becomes less pronounced. The temperature gradients corresponding to this

minimum are quite pronounced at low jet to plate spacing, and so the cold annulus conducts heat away from the surrounding zone.

- The magnitudes of lateral conduction are approximately 5 times greater for the Re = 10500 jet compared to the Re = 5100 jet. Local q''_{lc} distributions show an absolute minimum at the jet's centre surrounded by an absolute maximum at r/D ≈ 1.4. At low H/D values a secondary minimum in the q''_{lc} distribution occurs at larger r/D values. At H/D = 0.6 this minimum is approximately 10% of the primary minimum. The secondary minimum vanishes as H/D values are increased to values greater than 3.

- Recovery factor distributions for the multiple jets demonstrated similar trends to the single jet with a local maximum at the stagnation point which is surrounded by a cool region. However the shape of the recovery distribution for an array jet differs from that for a single jet due to multiple jet interactions. For peripheral array jets the local maximum associated with the jet centre is found to occur away from the geometrical centre of the jet. This offset distance is found to generally increase with increasing Reynolds number and increasing number of jets. Between multiple jets a secondary stagnation region is formed, resulting from the collision of wall jets from neighbouring jets. The location of the secondary stagnation region for the 3×3 jet array is closer to the peripheral jet than to the centre jet. The absolute magnitudes of lateral conduction increase as H/D values decrease.

- Finally the effects of confinement were investigated for a nozzle exit to plate spacing of one jet diameter. Tests were conducted for confinement levels, Z_{plate}, = 0D, 4D and 12D where Z_{plate}/D = 0 corresponds to maximum confinement; jet Reynolds numbers of 14400 and 7500 were used. The results obtained showed recovery factor to be independent of levels of confinement over the range of parameters studied.

This research gives a great insight into the temperature distributions that result from large Mach number jets and how various parameters affect these temperature distributions. This investigation also offers novel information on the magnitudes of lateral conduction that can be achieve from multiple jet impingement. The use of conjugate heat transfer demonstrates potential for hot spot cooling of electronic devices, as lateral conduction allows for heat flux to be shifted away from warm regions.

6.2 RECOMMENDATIONS FOR FURTHER WORK

The current research has lead to the development of an experimental facility and data analysis technique capable of acquiring information from impinging micro jets. The research to date has been limited to an unheated impingement surface. Further work is needed to expand the current study to look at jet cooling characteristics for a heated foil and to determine convective heat transfer coefficients, h. Distributions of h may be traditionally calculated from carrying out just two tests on both a heated and an unheated foil surface but more recently researchers, Fenot et al. (2005), have used a linear regression method to calculate h. This method involves fixing impinging jet parameters, varying the heat flux of the impingement surface, recording temperature distributions and then using linear regression to evaluate local heat transfer coefficient and local adiabatic temperature distributions. Findings from the current investigation demonstrated recovery factor to be independent of the level of confinement but a further study of the effects of varying levels of confinement on the temperature distribution resulting from a heated impingement surface would be interesting. San et al. (1997) showed that varying the width of the heated impingement plate has an influence on local Nusselt numbers as increasing the surface heating width results in lower stagnation Nusselt numbers. They attributed this phenomenon to flow recirculation so it is expected that varying the level of confinement in a hot test will affect recirculation and thus have an effect on the corresponding temperature distributions. Due to the small scale of this study flow visualisation would be difficult but such a study would reveal useful information. The recovery and lateral conduction study may also be expanded to cover a 4×4 jet array and different array configurations such as staggered arrays.

REFERENCES

Arjocu, S. C. and Liburdy, J. A., Near Surface Characterization of an Impinging Elliptic Jet Array, Transactions of the ASME – Journal of Fluids Engineering, 121, pp. 384–390, 1999

Asheghi, M., Microscale Heat Transfer, article from Electronic Cooling, was published 1th of July, 2007

Ashforth-Frost S. and Jambunathan K., Effect of Nozzle Geometry and Semi-Confinement on the Potential Core of a Turbulent Axisymmetric Free Jet, International Communications in Heat and Mass Transfer, Vol. 23 (2), pp. 155-162, 1996

Ashforth-Frost, S, Jambunathan, K. and Whitney C.F., Velocity and Turbulence Characteristics of a Semi-Confined Orthogonally Impinging Slot Jet, Experimental Thermal and Fluid Science, Vol. 14, pp. 60–67, 1997

Astarita, T. and Cardone G., Thermofluidynamic Analysis of the Flow in a Sharp 1800 Turn Channel, Experimental Thermal and Fluid Science, Vol. 20 (3-4), pp. 188-200, 2000

Barata, J. M. M. and Durao, D. F. G., Laser-Doppler Measurements of Impinging Jet Flows Through a Crossflow, International Proceedings of the 11th International Symposium on Applications of Laser Techniques to Fluid Mechanics, Lisbon, 2002

Baydar E., Confined Impinging Air Jet at Low Reynolds Numbers, Experimental Thermal and Fluid Science, Vol. 19, pp. 27–33, 1999

Baydar, E. and Ozmen, Y., An Experimental and Numerical Investigation on a Confined Impinging Air Jet at High Reynolds Numbers, Applied Thermal Engineering, Vol. 25 (2-3) , pp.409-421, 2005

Baydar, E. and Ozmen, Y., "An experimental investigation on flow structures of confined and unconfined impinging air jets," Heat Mass Transfer, Vol. 42, pp. 338–346, 2006

Behnia, M.S., Parneix, S., Shabany, Y. and Durbin, P., Numerical Study of Turbulent Heat Transfer in Confined and Unconfined Impinging Jets, International Journal of Heat Fluid Flow, Vol. 20, pp. 1-9, 1999

Beitelmal, A.H., Saad, M.A. and Patel, C.D., The Effect of Inclination on the Heat Transfer between a flat Surface and an Impinging Two-Dimensional Air Jet, International Journal of Heat and Fluid Flow, Vol. 21, pp. 156-163, 2000.

Benedict, Fundamentals of Temperature, Pressure, and Flow Measurements, Wiley, New York, ISBN: 0-471-06561-7, 1977

Beskok, A. and Karniadakis, G.E., Simulation of Heat Transfer and Momentum Transfer in Complex Microgeometries, Journal of Thermophysics Heat Transfer, 8 (4), pp. 647-655, 1994

Brevet, P., Dejeu C., Dorignac, E., Jolly, M. and Vullierme, J.J., Heat Transfer to a Row of Impinging Jets in Consideration of Optimization, International Journal of Heat and Mass Transfer, Vol. 45, pp. 4191–4200, 2002

Brevet, P., Dorignac, E. and Vullierme, J.J., Mach Number Effect On Jet Impingement Heat Transfer, Annals New York Academy of Sciences, Vol. 934, pp. 409-416, 2001

Brignoni, L.A. and Garimella, S.V., Effects of Nozzle-inlet Chamfering on Pressure Drop and Heat Transfer in Confined Air Jet Impingement, International Journal of Heat and Mass Transfer, Vol. 43, pp. 1133-1139, 2000

Can, M., Etemoglu, A. B. and Avci, A., Experimental Study of Convective Heat Transfer Under Arrays of Impinging Air Jets from Slots and Circular Holes, Heat Mass Transfer, Vol. 38, pp.251–259, 2002

Çengel, Y.A., Heat Transfer, 2nd Edition, ISBN: 0-07-115150-8, p. 567, 2003

Cheng, T.C., Chiou, P.H. and Lin T.F., Visualization of Mixed Convective Vortex Rolls in an Impinging Jet Flow of Air through a Cylindrical Chamber, International Journal of Heat and Mass Transfer, Vol. 45, pp. 3357–3368, 2002

Chua, L.P., Yu, S.C.M. and Li, H.S., Flow Visualization and Preliminary Measurements of a Confined Jet with and without Target, International Communications in Heat and Mass Transfer, Vol. 27, pp. 191–200, 2000

Chung, Y.M. and Luo, K.H., Unsteady Heat Transfer Analysis of an Impinging Jet, Journal of Heat Transfer, Vol. 124 (6), pp. 1039-1048, 2002

Colucci, D.W. and Viskanta, R., Effect of Nozzle Geometry on Local Convective Heat Transfer to a Confined Impinging Air Jet, Experimental Thermal Fluid and Science, Vol. 13 (1), pp. 71-80, 1996

Daniels, E., Fagerlund, E., Glansholm, D., Hartmann, B. Kleman, B., and Lindberg P., FOA orienterar om infraröd teknik, 1975

Didden, N., and Ho, C.M., Unsteady Separation in a Boundary Layer Produced by an Impinging Jet, Journal of Fluid Mechanics, Vol. 160, pp. 234-256, 1985

Elison, B. and Webb, B.W., Local Heat Transfer to Impinging Liquid Jets in the Initially Laminar, Transitional, and Turbulent Regions, Journal of Heat and Mass Transfer, Vol. 37 (8), pp.1207-1216, 1994

Fabbri, M. and Dhir, V.K., Optimized Heat Transfer for High Power Electronics Cooling using Arrays of Microjets, Journal of Heat Transfer, Vol. 127 pp. 760–769, 2005

Fenot, M., Vullierme, J.J., and Dorignac, E., Local Heat Transfer due to Several Configurations of Circular Air Jets Impinging on a Flat Plate with and without Semi-confinement, International Journal of Thermal Sciences, Vol. 44 (7), pp. 665-675, 2005

Fitzgerald, J.A., An Experimental Investigation of the Flow Field in a Confined and Submerged Impinging Jet, Thesis (M.S. in Mechanical Engineering), University of Wisconsin, Milwaukee, 1997

Fitzgerald, J.A. and Garimella, S.V., A Study of the Flow Field of a Confined and Submerged Impinging Jet International Journal of Heat Mass Transfer, Vol. 41, pp. 1025–1034, 1998

Fox, M.D., Kurosaka, M., Hedges, L., ans Hirano, K., The Influence of Vortical Structures on the Thermal Fields of Jets, Journal of Fluid Mechanics, Vol. 255, pp. 447-472, 1993

Gardon, R. and Akfirat, J.C., The Role of Turbulence in Determining the Heat Transfer Characteristics of Impinging jets, International Journal of Heat and Mass Transfer, Vol. 8, pp.1261–1272, 1965

Gardon, R. and Cobonpue, J., "Heat Transfer between a Flat Plate and Jets of Air Impinging on it," International Developments in Heat Transfer, Proceedings 2nd International Heat Transfer Conference, ASME, New York, pp. 454–460, 1962

Garimella, S.V. and Rice, R.A., Confined and Submerged Liquid Jet Impingement heat transfer, ASME Journal of Heat Transfer, Vol. 117, pp.871-877, 1995

Garimella, S.V., Advances in mesoscale thermal management technologies for microelectronics, Microelectronics Journal, Vol. 37 (11), pp. 1165-1185, 2006

Garimella, S.V. and Schroeder, V.P., Local Heat Transfer Distributions in Confined Multiple Air Jet Impingement, Journal of Electronic Packaging, Vol. 123 (3), pp.165–172, 2001

Garimella, S.V., Heat Transfer and Flow Fields in Confined Jet Impingement, Annual Review of Heat Transfer, Vol. 11, pp. 413-494, 2000

Geers, L.F.G., Multiple Impinging Jet Arrays: an Experimental Study on Flow and Heat Transfer, PhD thesis, Delft University of Technology, 2003

Giralt, F., Chia, C.J. and Trass, O., Characterization of the Impingement Region in an Axisymmetric Turbulent Jet, Ind. Eng. Chemistry Fundamentals, Vol. 16 (1), pp. 21–28, 1977

Glauert, M. G., The Wall Jet, Journal of Fluid Mechanics, Vol. 1 (6), pp.625-643, 1956

Goldstein, R.J., Behbahani, A.I. and Kieger Heppelmann, K., Streamwise Distribution of the Recovery Factor and the Local Heat Transfer Coefficient to an Impinging Circular Air Jet, International Journal of Heat and Mass Transfer, Vol. 29 (8), pp. 1227-1235, 1986

Goldstein, R.J., and He, B., Energy Separation and Acoustic Interaction in Flow Across a Circular Cylinder, Journal of Heat Transfer, Vol. 123 (4), pp. 682-687, 2001

Goldstein, R.J., and Seol, W.S. Heat Transfer to a Row of Impinging Circular Air Jets Including the effects of Entrainment, International Journal of Heat and Mass Transfer, Vol. 34 (8), pp. 2133-2147, 1991

Goldstein, R.J. and Timmers, J.F., Visualization of Heat Transfer from Arrays of Impinging Jets, Int. J. of Heat and Mass Transfer, Vol. 25, pp. 1857-1868, 1982

Goodro, M., Park, J., Ligrani, P., Fox M. and Moon, H.K., Effects of Mach Number and Reynolds number on Jet Array Impingement Heat Transfer, International Journal of Heat and Mass Transfer, Vol. 50 (1-2), pp. 367-380, 2007

Han, B. and Goldstein, R.J., Instantaneous Energy Separation in a Free Jet—Part II. Total Temperature Measurement, International Journal of Heat and Mass Transfer, Vol. 46, pp. 3983-3990, 2003

Harvey, J. K. and Perry, F. J., Flowfield Produced by Trailing Vortices in the Vicinity of the Ground, AIAA Journal, Vol. 9 (8), pp. 1659-1660, 1971

Hestroni G., Rozenblit R. and Yarin L.P., A Hot-foil Infrared Technique for Studying the Temperature Field of a Wall, Meas. Sci. Technol. Vol. 7, pp. 1418–27, 1996

Hollworth, B.R. and Dagan, L., Arrays of Impinging Jets With Spent Fluid Removal Through Vent Holes on the Target Surface. Part 1: Average Heat Transfer, ASME J. Eng. Power, Vol. 102, pp. 994–999, 1980

Hollworth, B. R. and Gero, L. R. Entrainment Effects on Impingement Heat Transfer: Part II - Local Heat Transfer Measurements, ASME Journal of Heat Transfer, Vol. 107, pp. 910-915, 1985

Hrycak, P., Lee, D.T., Gauntner, J.W., and Livengood, J. N. B., Experimental Characteristics of a Single Turbulent Jet Impinging on a Flat Plate, National Aeronautics and Space Administration, NASA TN D-5690, 1970

Huber, A.M. and Viskanta R., Effect of Jet-Jet Spacing on Convective Heat-Transfer to Confined, Impinging Arrays of Axisymmetrical Air-Jets, International Journal of Heat and Mass Transfer, Vol.37 (18), pp. 2859-2869, 1994a

Huber, A. M. and Viskanta, R., Impingement Heat Transfer with a Single Rosette Nozzle, Experimental Thermal and Fluid Science, Vol. 9, pp. 320–329, 1994b

Ichimiya, K. and Hosaka, N., Experimental Study of Heat Transfer Characteristics due to Confined Impinging Two-Dimensional Jets, Experimental Thermal Fluid and Science, Vol. 5, pp. 803–807, 1992

Ichimiya, K. and Yamada, Y., "Three Dimensional Heat Transfer of a Confined Circular Impinging Jet with Buoyancy Effects," ASME J. Heat Transfer, Vol. 125, pp. 250–256, 2003

Incropera, F.P., Liquid Cooling of Electronic Devices by Single-Phase Convection, Wiley Interscience, ISBN: 0-471-15986-7, 1999

Jahangeer, S., Ramis, M.K., and Jilani, G., Conjugate Heat Transfer Analysis of a Heat Generating Vertical Plate, International Journal of Heat and Mass Transfer, Vol. 50 (1-2), pp. 85-93, 2007

Jen, T. C. and Lavine, A. S., A Variable Heat Flux Model of Heat Transfer in Grinding: Model Development, ASME Journal of Heat Transfer, Vol. 117, pp.473-478, 1995

Kataoka, K., Impingement Heat Transfer Augmentation due to Large Scale Eddies, Heat Transfer, Proceeding of the 9th International Heat Transfer Conference, Vol. 1, pp. 255–273, 1990

Kline, S.J. and McClintock, F.A., Describing Uncertainties in Single Sample Experiments, Mech. Eng., pp. 3-8, 1953.

Lasance, C.J.M. and Simons, R.E., Advances In High-Performance Cooling For Electronics, Electronic Cooling, (Nov. 2005) Vol. 11, pp. 22–39, 2005

Lallave, J.C., Rahman, M.M., Kumar, A., Numerical Analysis of Heat Transfer on a Rotating Disk Surface under Confined Liquid Jet Impingement Journal of Heat and Fluid Flow, Vol. 28, pp.720-734, 2007

Lee, P., Choi, H. and Lee, S., The Effect of Nozzle Height on Cooling Heat Transfer from a Hot Steel Plate by an Impinging Liquid Jet, Iron and Steel Institute of Japan International Journal, Vol. 44 (4), pp.704-709, 2004a

Lee, D.H., Song, J. and Chan Jo, M.C., The Effects of Nozzle Diameter on Impinging Jet Heat Transfer and Fluid Flow, J. Heat Transfer, (Aug. 2004), Vol. 126 (4), pp. 554-557, 2004b

Lee, J. and Lee, S.J., The Effect of Nozzle Configuration on Stagnation Region Heat Transfer Enhancement of Axisymmetric Jet Impingement International Journal of Heat Mass Transfer, Vol. 43 (18), pp. 3497–3509, 2000a

Lee, J. and Lee, S.J., The Effect of Nozzle Aspect Ratio on Stagnation Region Heat Transfer Characteristics of Elliptic Impinging Jet, International Journal of Heat and Mass Transfer, Vol. 43, pp. 555-575, 2000b

Lepicovsky, J., The Role of Nozzle Exit Boundary Layer Velocity Gradient in Mixing Enhancement of Free Jets, Proceedings of the 3rd ASCE/ASME Mechanics Conference, La Jolla, CA, July 9-12, (A90-45252 20-34), New York, American Society of Mechanical Engineers, pp. 41-47, 1989

Lienhard, J.H., Liquid Jet Impingement, Annual Review of Heat Transfer, Begell House, New York, Vol. 6, chpt. 4, pp. 199-270, 1995

Lienhard (V), J.H. and Lienhard (IV), J. H., Velocity Coefficients for Free Jets from Sharp Edged Orifices, ASME Journal of Fluids Engineering, Vol. 106, pp.13-17, 1984

Limaye, M.D., Vedula, R.P., and Prabhu, S.V., Local Heat Transfer Distribution on a Flat Plate Impinged by a Compressible Round Air Jet, International Journal of Thermal Sciences, Draft Manuscript, Manuscript Number: THESCI-D-09-00739, 2010

Lin Y.F. and Sheu M.J., Interaction of Parallel Turbulent Plane Jets, AIAA journal ISSN 0001-1452 CODEN AIAJAH, Vol. 29 (9), pp. 1372-1373, 1991

Livingood, J. N. B. and, Gauntner, J. W., Heat Transfer Characteristics of a Single Circular Air Jet Impinging on a Concave Hemispherical Shell, NASA Technical Report, Report Number: E-7462; NASA-TM-X-2859, 1973

Lupton, T.L., Murray, D.M. and Robinson, A.J., IR thermography measurement of impinging jet heat transfer from a heated thin foil, 10th UK National Heat Transfer Conference, Edinburgh, 10-11 September 2007a

Lupton, T.L., Murray, D.B. and Robinson, A.J., Confinement effects in heat transfer to a miniature compressible impinging air jet, paper submitted for ASME-JSME Thermal Engineering Summer Heat Transfer Conference, Vancouver, British Columbia, Canada, 2007b

Marple, V.A., Liu, B.Y.H. and Whitby, K.T, On the Flow Fields of Inertial Impactors, Transactions of the ASME, Journal of Fluids Engineering, pp. 394–400, 1974

Martin, H., Heat and Mass Transfer between Impinging Gas jets and Solid Surfaces, Advances in Heat Transfer, Vol. 13, pp. 1-60, 1977

Matlab User's Guide, Image Processing Toolbox, The Math Works Inc., 1998

Matsumoto, R., Ishihara, I., Yabe, T., Ikeda, K., Kikkawa, S. and Senda, M., Impingement Heat Transfer Within Arrays of Circular Jets Including the Effect of Crossflow, (AJTE99-6386) International Proceedings of the 5th ASME/JSME Joint Thermal Engineering Conference, San Diego, California, paper AJTE99-6386, pp. 1–8, 1999

Meola, C., de Luca, L. and Carlomagno, G. M., Azimuthal Instability in an Impinging Jet: Adiabatic Wall Temperature Distribution, Experiments in Fluids (ISSN 0723-4864), Vol. 18 (5), pp. 303-310, 1995

Meola C. and Carlomagno G.M., Recent Advances in the Use of Infrared Thermography, Meas. Sci. Tech., Vol. 15, pp. R27–R58, 2004

Metzger, D.E., Florschuetz, L.W., Takeuchi, D.I., Behee, R.D., and Berry, R.A., Heat Transfer Characteristics for Inline and Staggered Arrays of Circular Jets with Cross-Flow of Spent Air, Journal of Heat Transfer, Vol. 101, pp. 526-531, 1979

Mohanty, A. K., and Tawfek, A. A., "Heat Transfer Due to a Round Jet Impinging Normal to a Flat Surface," Int. J. Heat Mass Transfer, Vol. 36, pp. 1639-1647, 1993

Motakef, S., High Heat Flux Removal by Microjet Impingement, article from Cooling Zone, was published 8th of July, 2005

Narasimha, R., Narayan, K.Y., Parthasarathy, S.P., Parametric Analysis of Turbulent Wall Jets in Still Air, Aeronautical Journal, Vol. 77, pp. 355 - 359, 1973

Narumanchi, S.V.J., Hassani, V., and Bharathan, D., Modeling Single-Phase and Boiling Liquid Jet Impingement Cooling in Power Electronics, Technical Report NREL/MP-540-38787, National Renewable Energy Laboratory, Golden, Colorado, 2005

Nishino, K., Samada, M., Kasuya, K., and Torii, K., Turbulence Statistics in the Stagnation Region of an Axisymmetric Impinging Jet Flow, Journal of Heat and Fluid Flow, Vol. 17 (3), pp. 193–201, 1996

O'Donovan, T.S. and Murray, D.B., Jet impingement Heat Transfer – Part I: Mean and Root-mean-square Heat Transfer and Velocity Distributions, International Journal of Heat and Mass Transfer, Vol. 50 (17-18), August 2007, pp. 3291-3301, 2007a

O'Donovan, T.S. and Murray, D.B., Jet Impingement Heat Transfer – Part II: A Temporal Investigation of Heat Transfer and Local Fluid Velocities, International Journal of Heat and Mass Transfer, Vol. 50 (17-18), August 2007, pp. 3302-3314, 2007b

Obot N.T., Majumdar A.S. and Douglas W.J.M., Effect of Nozzle Geometry on Impingement Heat Transfer under a Round Turbulent Jet, ASME Paper 79-WA/HT-53, 1979

Pan, Y. and Webb, B. W., Heat Transfer Characteristics of Arrays of Free-Surface Liquid Jets, Journal of Heat Transfer American Society of Mechanical Engineers, Vol. 117 (44), pp. 878-883, 1995

Patil, V.A. and Narayanan V., Application of Heated-thin-foil Thermography Technique to External Convective Microscale Flows, Measurement Science and Technology, Vol. (16), pp. 472–476, 2005

Peacock, G.R., Temperature Uncertainty of IR Thermal Imager Calibration, Proceedings of SPIE Thermosense XXVIII, Vol. 6205, 620509, 2006

Pence, D.V., Boeschoten, P.A. and Liburdy, J.A., Simulation of Compressible Micro-Scale Jet Impingement Heat Transfer, Journal of Heat Transfer, Vol. 125, pp. 447-453, 2003

Popiel, C. O. and Boguslawski, L., Mass or Heat Transfer in Impinging Single, Round Jets Emitted by a Bell-Shaped Nozzle and Sharp-Ended Orifice, Vol. 3 of the Proceeding of the 8th International Heat Transfer Conference, pp. 1187–1192, 1986

Raghu O., and Philip J., Thermal Properties of Paint Coatings on Different Backings Using a Scanning Photo Acoustic Technique, Measurement Science and Technology, Vol. 17 (11), pp. 2945-2949, 2006

Rahimi, M., Owen, I., and Mistry, J., Impingement Heat Transfer in an Under-expanded Axisymmetric Air Jet, International Journal of Heat and Mass Transfer, Vol. 46 (2), pp. 263-272, 2003

Rainieri, S. and Pagliarini, G., Data Processing Technique Applied to the Calibration of a High Performance FPA Infrared Camera, Infrared Physics and Technology, Vol. 43 (6), 2002a

Rainieri, S. and Pagliarini, G., Data Filtering Applied to Infrared Thermographic Measurements Intended for the Estimation of Local Heat Transfer Coefficient, Journal of Experimental Thermal and Fluid Science, Vol. 26 Vol. (2–4), pp. 109–114, 2002b

Robinson, A.J. and Schnitzler, E., An Experimental Investigation of Free and Submerged Miniature Liquid Jet Array Impingement Heat Transfer, Experimental Thermal and Fluid Science, Vol. 32 (1), pp. 1-13, 2007

Royne, A., Cooling Devices for Densely Packed, High Concentration PV Arrays, M.Sc. thesis, School of Physics, University of Sydney, Sydney, Australia, 2005

Royne, A. and Dey, C.J., Design of a Jet Impingement Cooling Device for Densely Packed PV Cells Under High Concentration, Solar Energy, vol 81 (8), August 2007, pp. 1014-1024, 2007

San, J.Y. and Lai, M.D., Optimum Jet-to-Jet Spacing of Heat Transfer for Staggered Arrays of Impinging Air Jets, International Journal of Heat and Mass Transfer, Vol. 44, (21), pp. 3997-4007, 2001

San, J.Y., Huang, C.H. and Shu, M.H., Impingement Cooling of a Confined Circular Air Jet, International Journal of Heat and Mass Transfer, Vol. 40, pp. 1355–1364, 1997

Sapatnekar, S. S., article from the A to Z of Materials, www.azom.com/news.asp?news ID=2921, 2005

Sarghini, F., and Ruocco, G., Enhancement and Reversal Heat Transfer by Competing Modes in Jet Impingement, International Journal of Heat and Mass Transfer, Vol. 47, pp. 1711-1718, 2004

Stafford, J., Walsh, E. and Egan, V., Charaterising Convective Heat Transfer using Infrared Thermography and the Heated Thin Foil Technique, Measurment Science and Thechnology, Vol. 20 (10), 2009

Striegl, S. A. and Diller, T. E., An Analysis of the Thermal Entrainment Effect on Jet Impingement Heat Transfer, American Society of Mechanical Engineers, Winter Annual Meeting, Phoenix, AZ, Nov. 14-19, 1982

Viskanta, R., Heat Transfer to Impinging Isothermal Gas and Flame Jets, Experimental Thermal and Fluid Science, Vol. 6 (2), pp. 111-134, 1993

Voke, P.R. and Gao, S., Numerical Study of Heat Transfer from an Impinging Jet, International. Journal of Heat Mass Transfer, Vol. 41, pp. 671–680, 1998

Walker, J.D.A., Smith, C.R., Cerra, A.W. and Doligalski, T.L., Jet Impact of a Vortex Ring on a Wall, Journal of Fluid Mechanics, Vol. 181, pp. 99–140, 1987

Walshaw, A.C. and Jobson, D.A., Mechanics of Fluids, 2nd ed., Longman Group Ltd, London, 1972

Webb, B.W. and Ma, C.F., Single Phase Liquid Jet Impingement Heat Transfer, Advances in Heat Transfer, Vol. 26, pp. 105-217, 1995

Whelan, B.P. and Robinson A.J., Nozzle Geometry Effects in Liquid Jet Array Impingement, Applied Thermal Engineering, Vol. 29 (11-12), pp. 2211-2221, 2009

White, F.M., Viscous Fluid Flow, McGraw Hill, New York , 1974

Wiener, N., Extrapolation, Interpolation, and Smoothing of Stationary Time Series. New York: Wiley. ISBN 0-262-73005-7, 1949

Wolfersdorf, J.von, Influence of Lateral Conduction due to Flow Temperature Variations in Transient Heat Transfer Measurements, International Journal of Heat and Mass Transfer, Vol. 50 (5-6), pp. 1122-1127, 2007

Womac, D.J., Ramadhyani, S. and Incropera, F.P., Correlating Equations for Impingement Cooling of Small Heat Sources with Single Circular Liquid Jets, ASME Journal of Heat Transfer, Vol. 115, pp.106-115, 1993

Xin Liu, Gabour, L.A. and Lienhard, J.H., Stagnation-Point Heat Transfer during Impingement of Laminar Liquid Jets: Analysis Including Surface Tension, ASME, Transactions, Journal of Heat Transfer (ISSN 0022-1481), Vol. 115 (1), pp. 99-105, 1993

Yule, A. J., Large-Scale Structure in the Mixing Layer of a Round Jet, Journal of Fluid Mechanics, Vol. 89 (3), pp. 413–432, 1978

# APPENDIX A: NOZZLE DESIGNS

Contained within the next three pages are the nozzle parts used in the confinement study. Included afterwards are the three 0.61 mm diameter nozzle configuration designs for the single, 2×2 square and 3×3 square jet array. 4 more similar nozzle arraignments with different interjet spacings were also tested. All dimensions are given in millimeters.

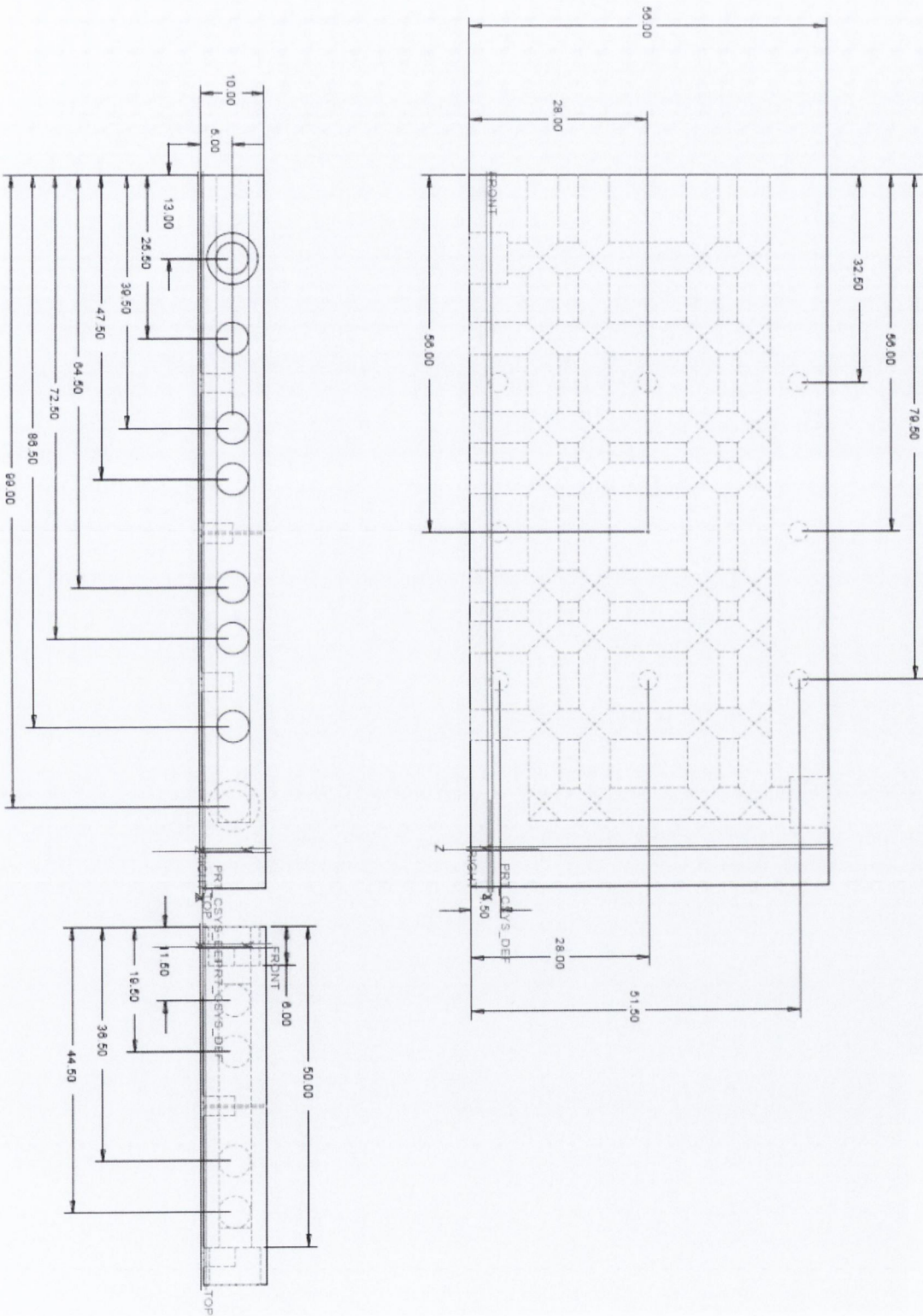## A.1 CONFINEMENT STUDY: CONFINEMENT PLATE
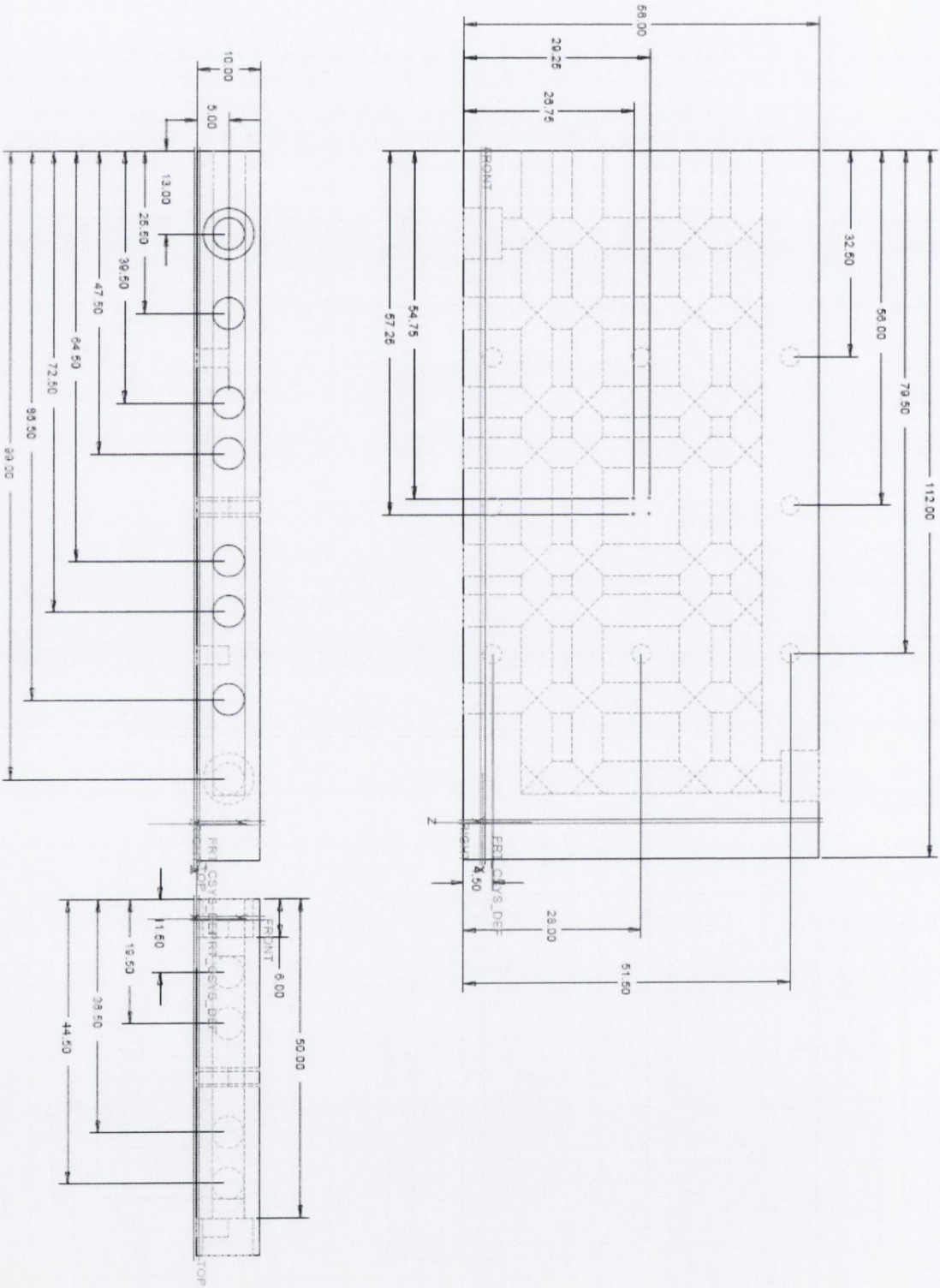
A.2 CONFINEMENT STUDY: BRASS GUIDANCE TRACK
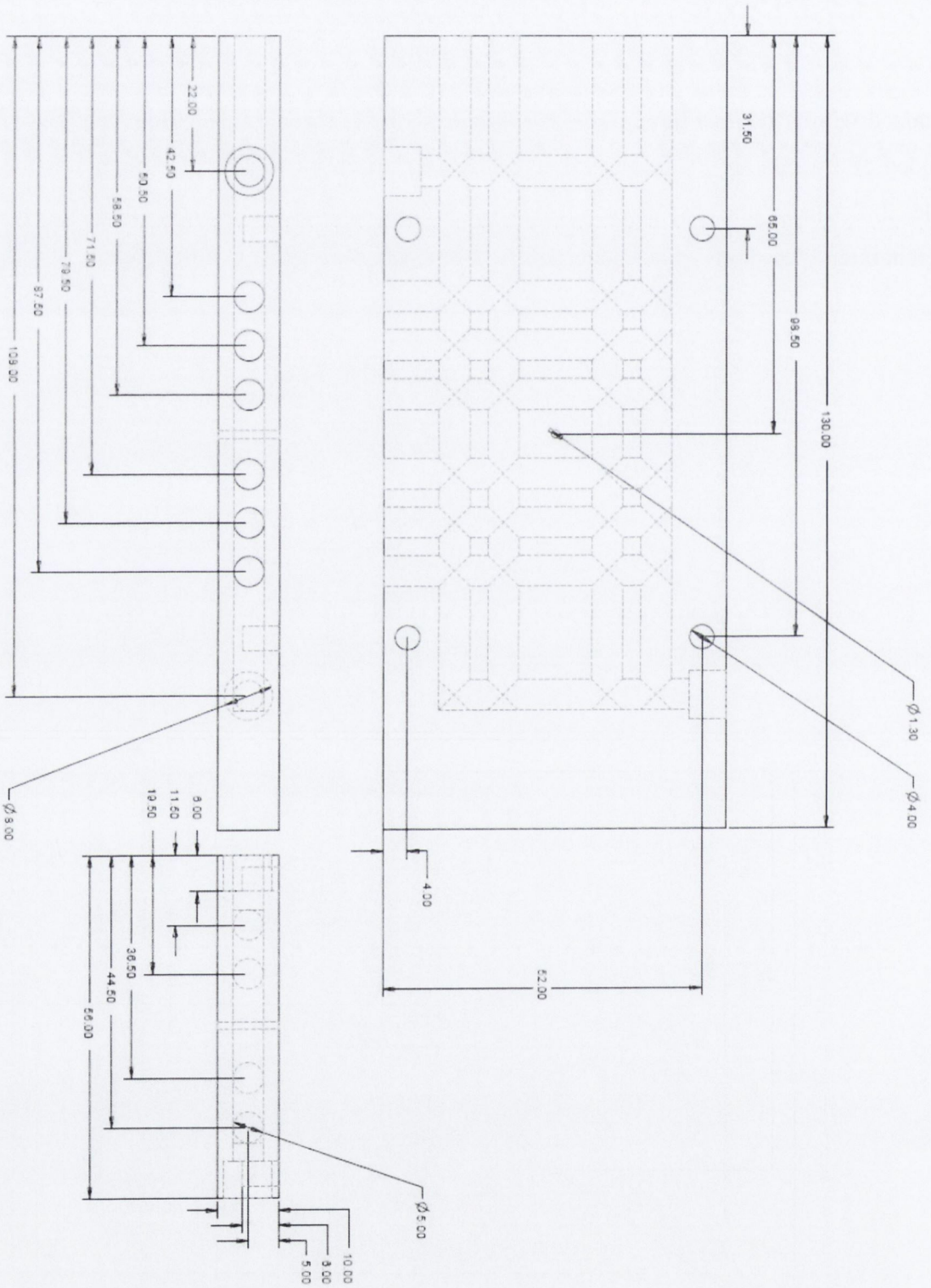
A.3 CONFINEMENT STUDY: BRASS SLIDER
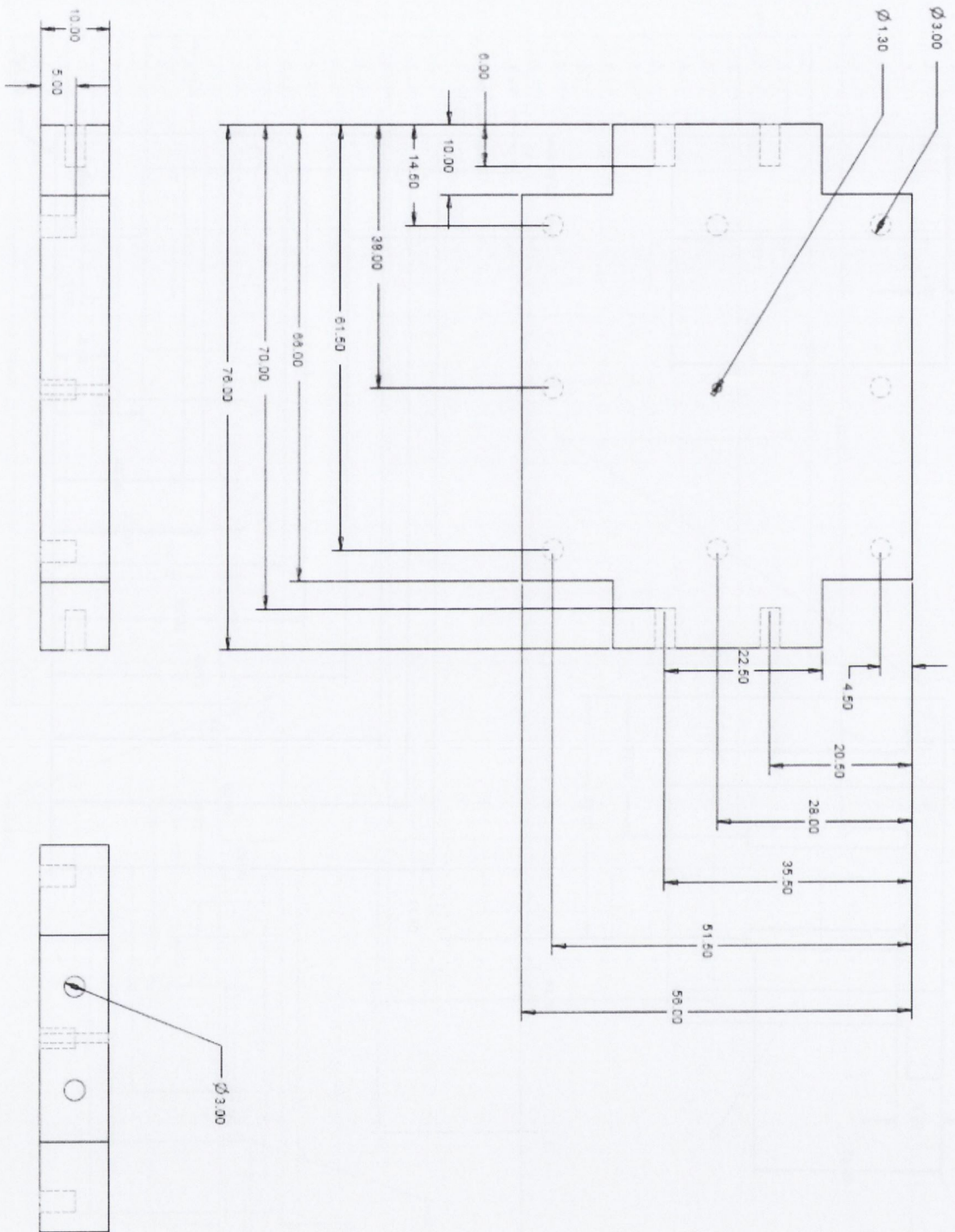
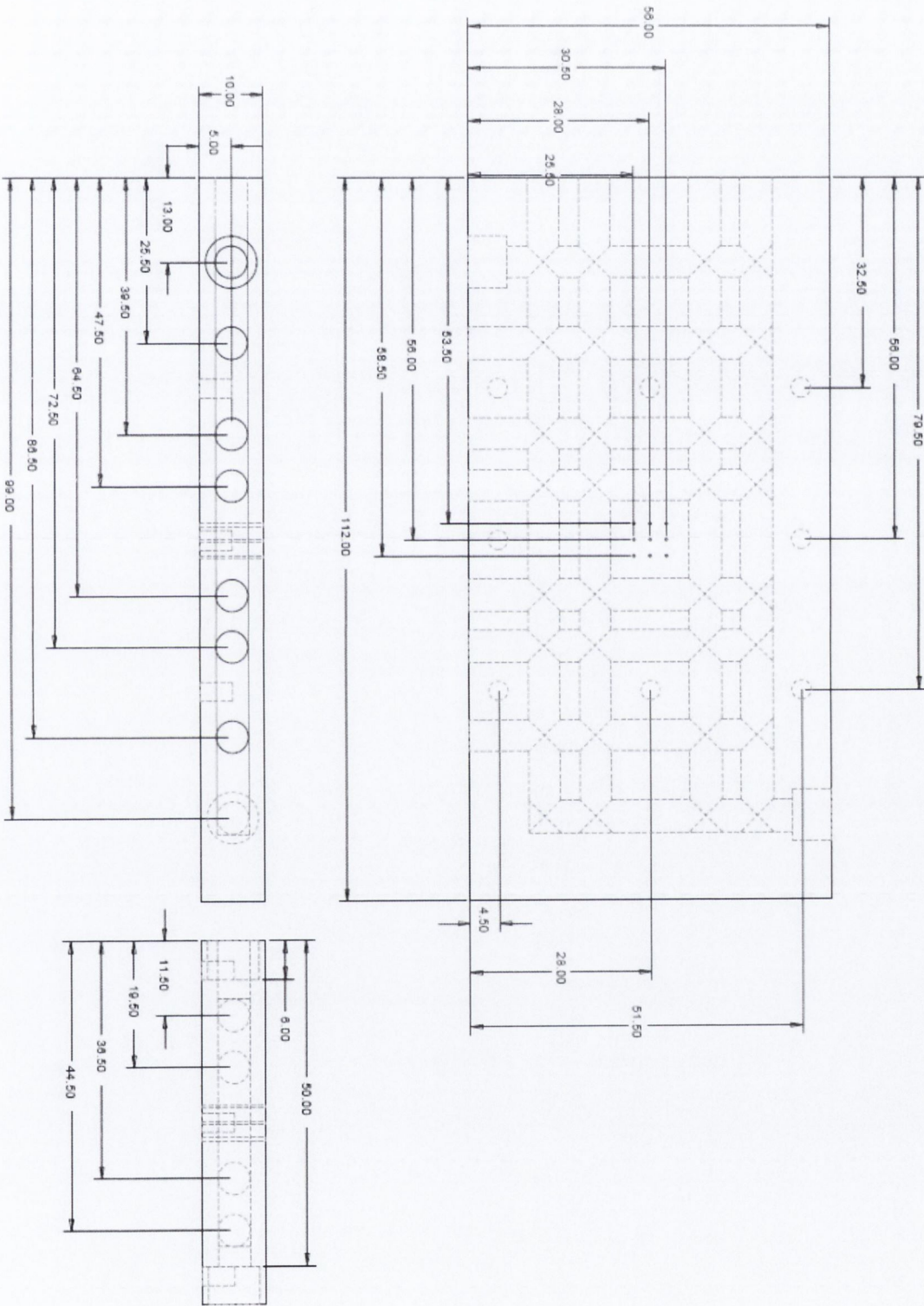## A.4 MULTIPLE JET STUDY: SINGLE JET NOZZLE

A.5 MULTIPLE JET STUDY: 2×2 JET ARRAY NOZZLE

A.6 MULTIPLE JET STUDY: 3×3 JET ARRAY NOZZLE

APPENDIX B:

CALIBRATION CERTIFICATES

B.1 FLIR A40 INFRARED CAMERA

◆FLIR SYSTEMS™

Certificate No. 02724

Instrument Calibration Certificate

This is to certify that FLIR, THV, ThermoVision, ThermaCAM and SC series of scanners, the FLIR Temperature Reference models BB-150 and BB-400, have been calibrated using radiation sources, the accuracy of which are traceable to National Standards at the Swedish National Testing and Research and Research Institute (Sweden) or at the NIST, National Institute of Standards and Technology (USA).

All readings are within manufacturers specification.

FLIR Systems recommend recalibration every 12 months.

- Service Order No: 097083

- Customer: University of Dublin

- Model: Thermovision A40M F/W

- Serial No: 25000193
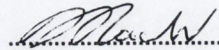
- Lenses: 24°, 50u, 18u

- Filters: NOF

INITIAL CHECK:
Within specification ☐
Out of Specification ☑ ... see attached Service Order Report

Calibration performed by: Adrian Goodhand

(signature)
(sign)

(signature)
(Title)

Calibration date: 28/08/2009

All business is conducted according to FLIR Systems Ltd. Standard Terms and Conditions of Sale and Service, a full set, of which, is available on request.

FORM 106 Issue 3

B.2 OMEGA RESISTANCE TEMPERATURE DETECTOR

OMEGA ENGINEERING LIMITED
ONE OMEGA DRIVE
RIVER BEND TECHNOLOGY CENTRE
NORTHBANK
IRLAM
MANCHESTER
M44 5BD
UNITED KINGDOM

Tel: +44 (0)161 777 6611
Fax: +44 (0)161 777 6622

FREEPHONE SALES 0800 488 488 (UK ONLY)

Website:

ISO 9002
REGISTERED COMPANY

NEWPORT®
OMEGA®
omega.co.uk

V.A.T. REG No. GB 620 0439 89   COMPANY REG No. 2564017

Certificate of Calibration

Certificate Number: M04481

Customer.:   University of Dublin
Description.:   RTD Probe
Type No.:   PR-11-2-100-M30-200-1/10DIN

Issue Date: 14-04-2003

S. O. No.:   09971
Serial No.:   4

The above instrument has been calibrated. All measurements made were referenced to standards of the laboratory whose values are traceable to UK National Standards. Copies of tests performed are on file at Omega Engineering Limited, Irlam, Manchester and are available upon request.

STD Temperature °C	Recorded Probe Temperature °C	Uncertainty of Measurement °C
0.00	0.05	0.15
49.95	50.10	0.18
99.90	100.05	0.20
200.20	200.20	0.27
300.20	300.1	0.37

Test Conditions	Humidity	35 %
	Temperature	22 °C

Instruments Used:	OE01, OE204, OE52

Calibrated By:	S. C. Roach

Signed:

Quality Manager

Ref: RTD.doc

The expanded uncertainties are based on the standard combined uncertainty multiplied by a coverage factor of K=2 providing a confidence probability of 95%

B.3 MKS MASS FLOW CONTROLLER

mks

MKS Instruments UK Limited - Telvac Engineering

Certificate of Calibration

Certificate Number:	090265827	
Date:	12-Jan-2009	
Calibration Data:	Final	
Mfg:	MKS	
Instrument Model:	1179A24CS1BVAB	
Serial number:	090265827	
Identifier:		
Test Gas:	N2	GCF 1.00
Nameplate Gas:	Air	GCF 1.00
Range (sccm):	20000	
Accuracy (%fsd):	1.00%	

Setpoint %	STD sccm	DUT sccm	Error sccm	Error mV	Error %
0%	0.00	0.00	0.00	0.00	0.00%
25%	5000.00	4964.00	-36.00	-9.00	-0.18%
50%	10000.00	10020.00	20.00	5.00	0.10%
75%	15000.00	15004.00	4.00	1.00	0.02%
100%	20000.00	19980.00	-20.00	-5.00	-0.10%
110%	22000.00	21844.00	-156.00	-39.00	-0.78%

The above calibration data was measured on the MKS
Mass Flow Standard identified below:

UK Ref.:	FS111
Range (sccm):	20000
Nameplate Gas:	N2
Serial Number:	477879
Part number:	1179A24CS1BV
Commissioned:	03-Apr-2001
Last cal date :	16-Jun-2008
Cal by:	MKS-UK
Technique:	ROR
Cal Gas:	N2

Leak Check: **Valve**   <0.5% FS   **Ext:**   <1.0E-9 mb/L/s

Data By: GD   **Comment:** MANUFACTURE

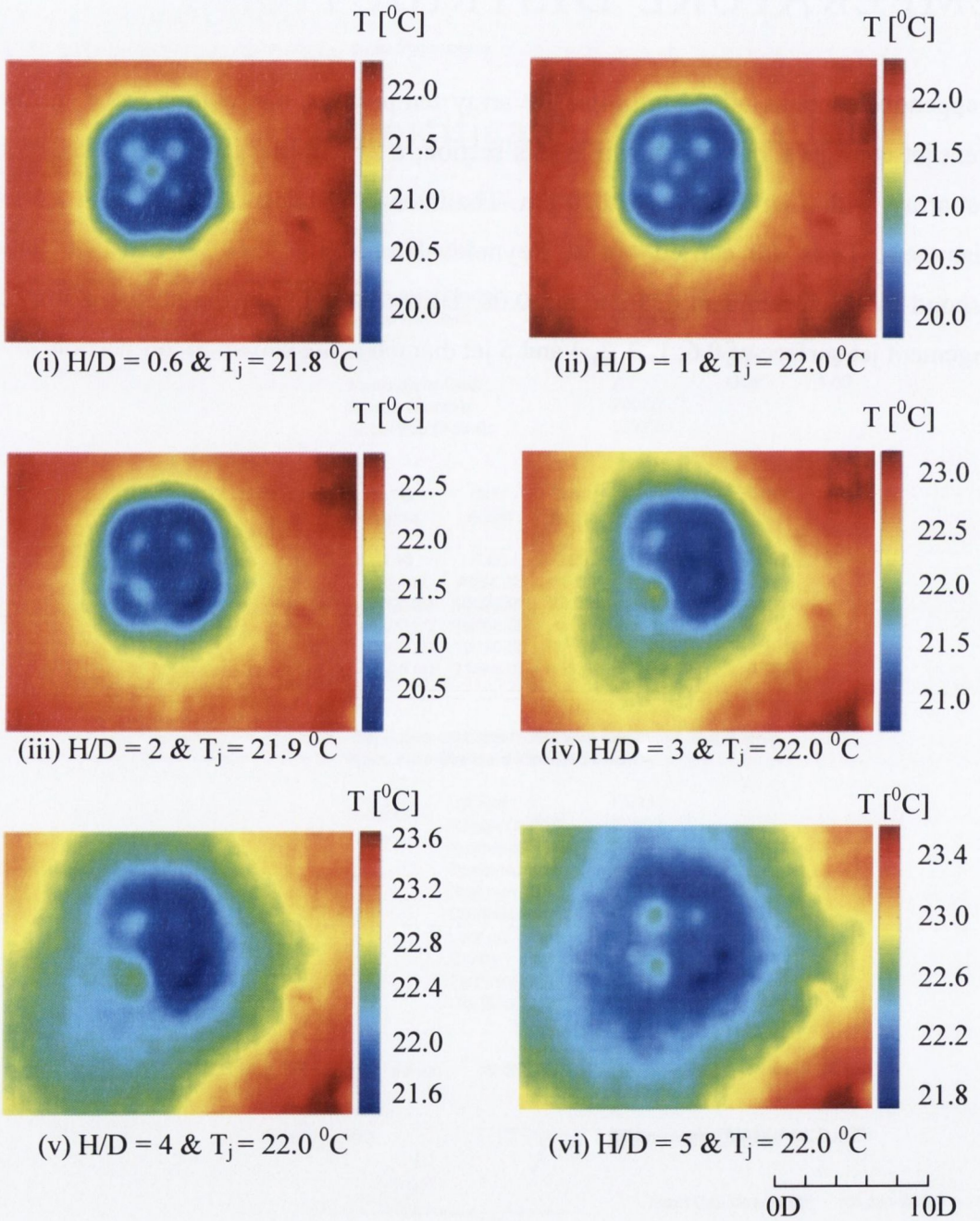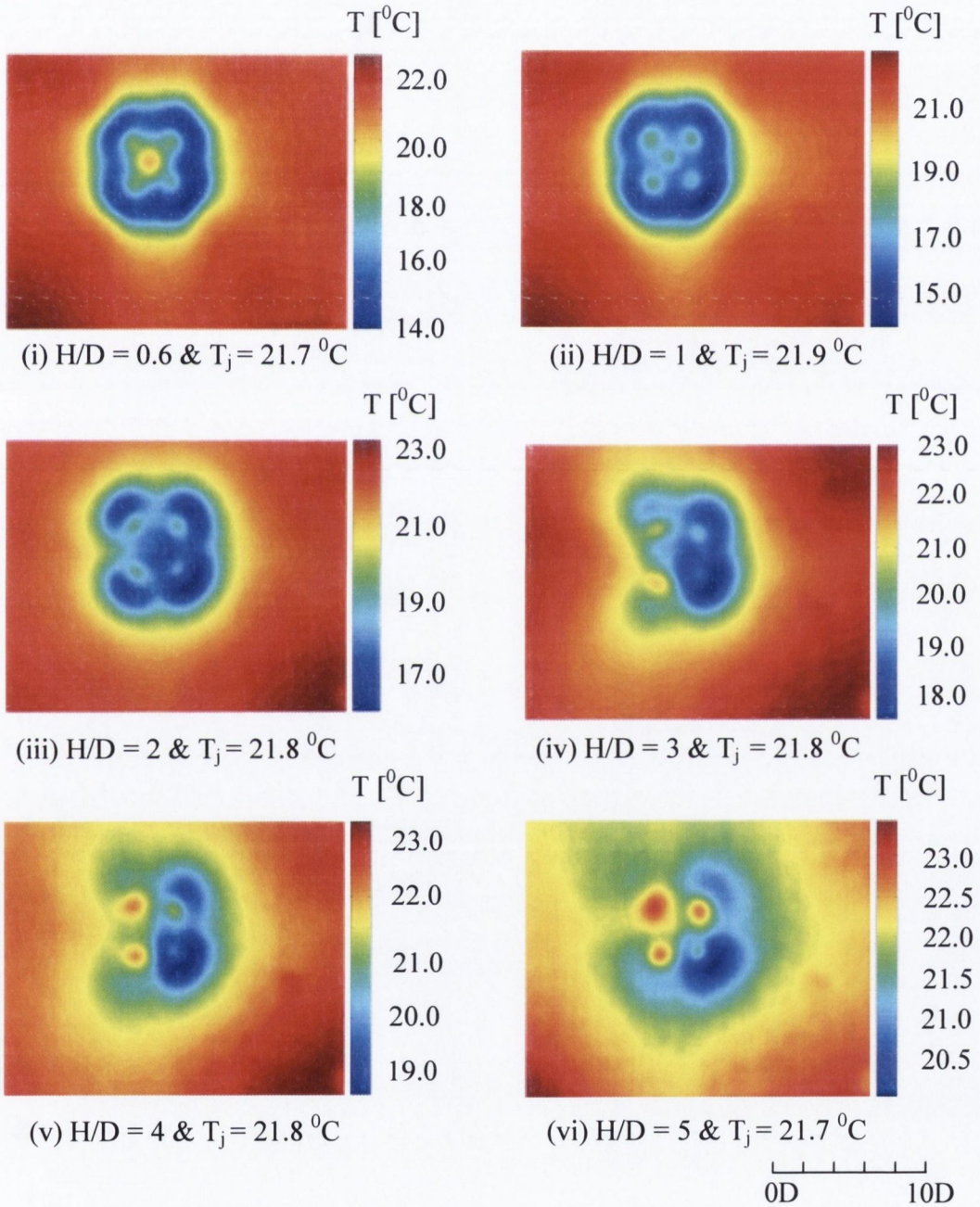**Checked By:**   **Next Cal. due date:**   12-Jan-2010

APPENDIX C:
TEMPERATURE DISTRIBUTIONS

This appendix contains all the multiple jet array temperature distributions studied. Two different jet configurations are shown in this section; a 2×2 in-line jet array and a 3×3 in-line jet array, with a jet diameter of 610 μm. The inter-jet spacing is altered from 2.5 to 6 jet diameters. Tests are carried out at Reynolds Numbers of 5100 and 10500 which correspond to Mach numbers of 0.36 and 0.68. Distances between the nozzle exit to the impingement jet surface of 0.6, 1, 2, 3, 4 and 5 jet diameters are shown in this section.

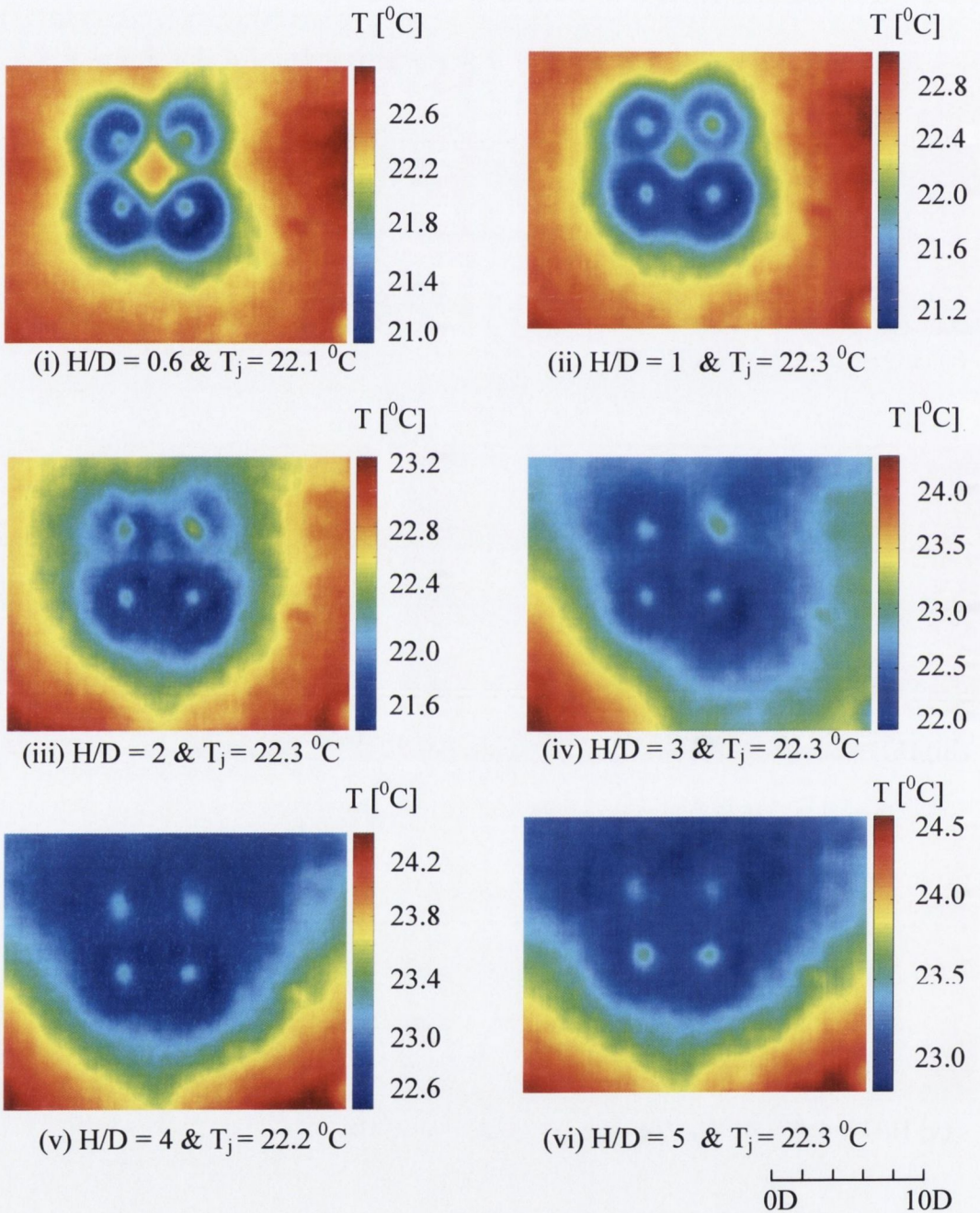## C.1 TEMPERATURE DISTRIBUTIONS FOR THE 2×2 JET ARRAY CONFIGURATION WITH RE = 5100 AND S/D = 2.5.

(i) H/D = 0.6 & T_j = 21.8 ^{0}C

(ii) H/D = 1 & T_j = 22.0 ^{0}C

(iii) H/D = 2 & T_j = 21.9 ^{0}C

(iv) H/D = 3 & T_j = 22.0 ^{0}C

(v) H/D = 4 & T_j = 22.0 ^{0}C

(vi) H/D = 5 & T_j = 22.0 ^{0}C

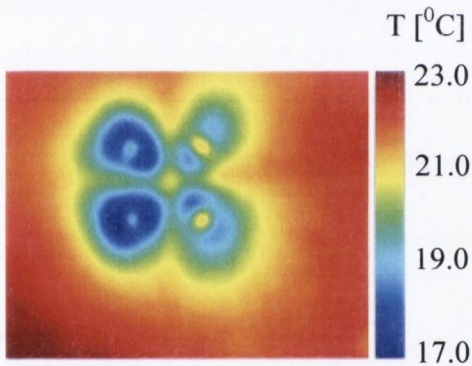## C.2 TEMPERATURE DISTRIBUTIONS FOR THE 2×2 JET ARRAY CONFIGURATION WITH RE = 10500 AND S/D = 2.5.

(i) H/D = 0.6 & T_j = 21.7 ^{0}C

(ii) H/D = 1 & T_j = 21.9 ^{0}C

(iii) H/D = 2 & T_j = 21.8 ^{0}C

(iv) H/D = 3 & T_j = 21.8 ^{0}C

(v) H/D = 4 & T_j = 21.8 ^{0}C

(vi) H/D = 5 & T_j = 21.7 ^{0}C

0D   10D

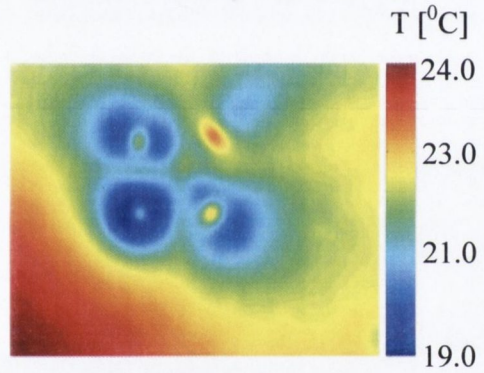## C.3 TEMPERATURE DISTRIBUTIONS FOR THE 2×2 JET ARRAY CONFIGURATION WITH RE = 5100 AND S/D = 4.

(i) H/D = 0.6 & T_j = 22.1 ^{0}C

(ii) H/D = 1 & T_j = 22.3 ^{0}C

(iii) H/D = 2 & T_j = 22.3 ^{0}C

(iv) H/D = 3 & T_j = 22.3 ^{0}C

(v) H/D = 4 & T_j = 22.2 ^{0}C

(vi) H/D = 5 & T_j = 22.3 ^{0}C

0D   10D

C.4 TEMPERATURE DISTRIBUTIONS FOR THE 2×2 JET ARRAY CONFIGURATION WITH RE = 10500 AND S/D = 4.

T [^{0}C]
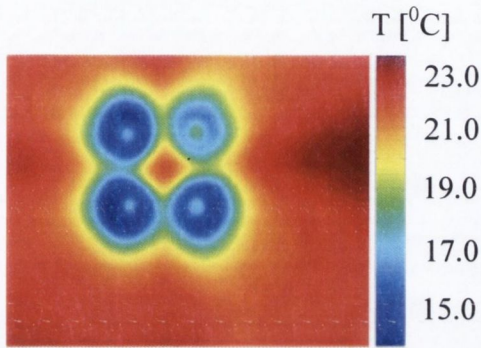
(i) H/D = 0.6 & T_j = 22.1 ^{0}C

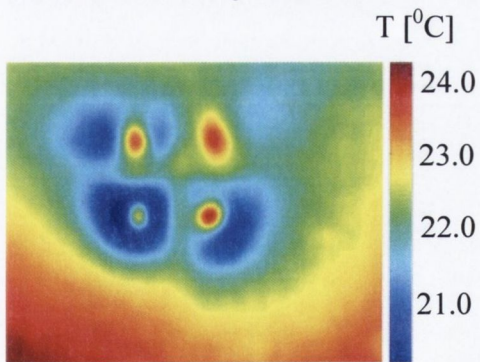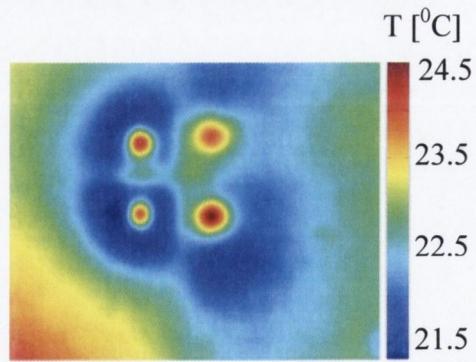(ii) H/D = 1 & T_j = 22.2 ^{0}C

(iii) H/D = 2 & T_j = 22.1 ^{0}C

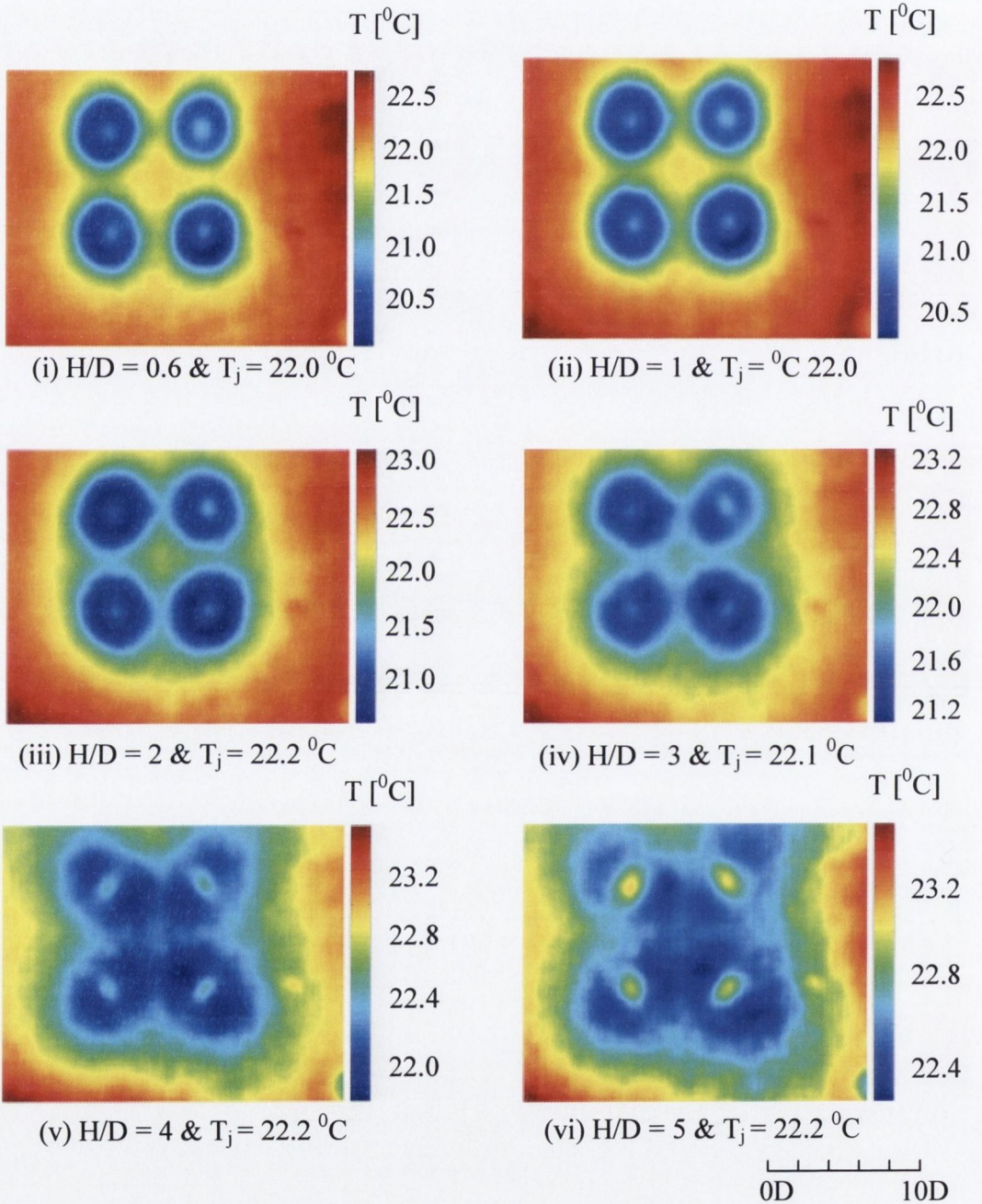(iv) H/D = 3 & T_j = 22.1 ^{0}C

(v) H/D = 4 & T_j = 22.1 ^{0}C

(vi) H/D = 5 & T_j = 22.1 ^{0}C

0D   10D

C.5 TEMPERATURE DISTRIBUTIONS FOR THE 2×2 JET ARRAY CONFIGURATION WITH RE = 5100 AND S/D = 6.

(i) H/D = 0.6 & T_j = 22.0 ^{0}C

(ii) H/D = 1 & T_j = ^{0}C 22.0

(iii) H/D = 2 & T_j = 22.2 ^{0}C

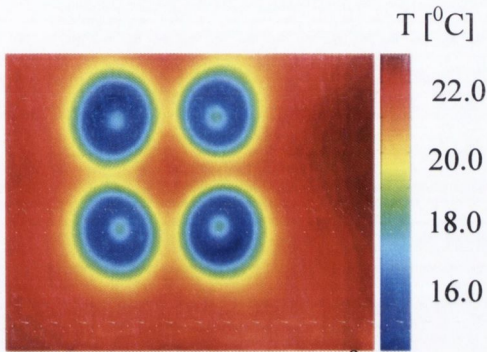(iv) H/D = 3 & T_j = 22.1 ^{0}C

(v) H/D = 4 & T_j = 22.2 ^{0}C

(vi) H/D = 5 & T_j = 22.2 ^{0}C

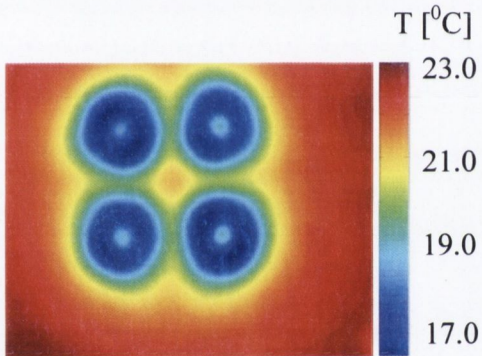0D   10D

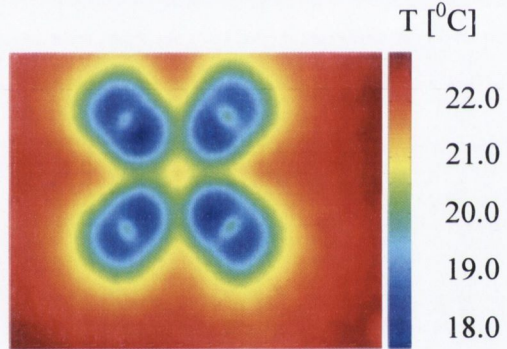## C.6 TEMPERATURE DISTRIBUTIONS FOR THE 2×2 JET ARRAY CONFIGURATION WITH RE = 10500 AND S/D = 6.

(i) H/D = 0.6 & T_j = 22.2 ^{0}C
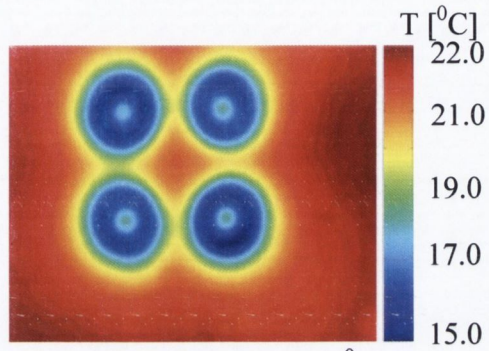
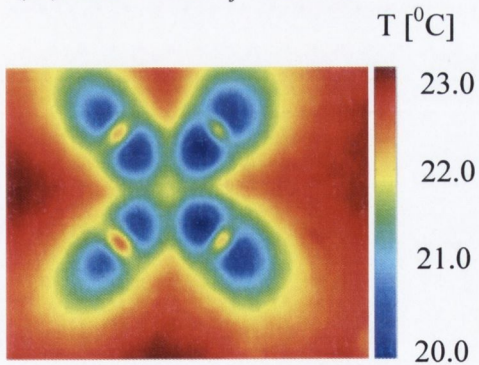(ii) H/D = 1 & T_j = 22.3 ^{0}C

(iii) H/D = 2 & T_j = 22.3 ^{0}C

(iv) H/D = 3 & T_j = 22.2 ^{0}C

(v) H/D = 4 & T_j = 22.4 ^{0}C
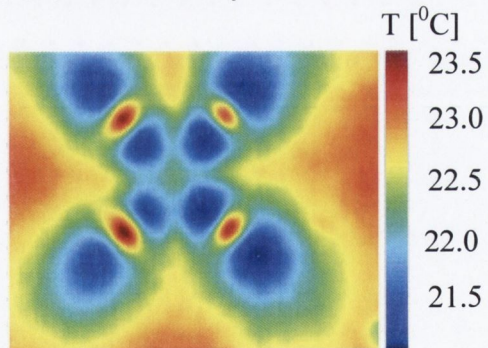
(vi) H/D = 5 & T_j = 22.3 ^{0}C

0D   10D

C.7 Temperature distributions for the 3×3 jet array configuration with Re = 5100 and S/D = 2.5.

(i) H/D = 0.6 & T_j = 20.7 ^{0}C

(ii) H/D = 1 & T_j = 19.9 ^{0}C

(iii) H/D = 2 & T_j = 19.8 ^{0}C

(iv) H/D = 3 & T_j = 19.6 ^{0}C

(v) H/D = 4 & T_j = 19.7 ^{0}C

(vi) H/D = 5 & T_j = 19.7 ^{0}C

0D   10D

C.8 TEMPERATURE DISTRIBUTIONS FOR THE 3×3 JET ARRAY CONFIGURATION WITH RE = 10500 AND S/D = 2.5.

(i) H/D = 0.6 & T_j = 20.4 ^{0}C

(ii) H/D = 1 & T_j = 20.4 ^{0}C

(iii) H/D = 2 & T_j = 20.6 ^{0}C

(iv) H/D = 3 & T_j = 20.1 ^{0}C

(v) H/D = 4 & T_j = 19.5 ^{0}C

(vi) H/D = 5 & T_j =19.6 ^{0}C

0D   10D

C.9 TEMPERATURE DISTRIBUTIONS FOR THE 3×3 JET ARRAY CONFIGURATION WITH $R_E = 5100$ AND $S/D = 4$.

(i) H/D = 0.6 & T_j = 21.3 ^{0}C

(ii) H/D = 1 & T_j = 21.1 ^{0}C

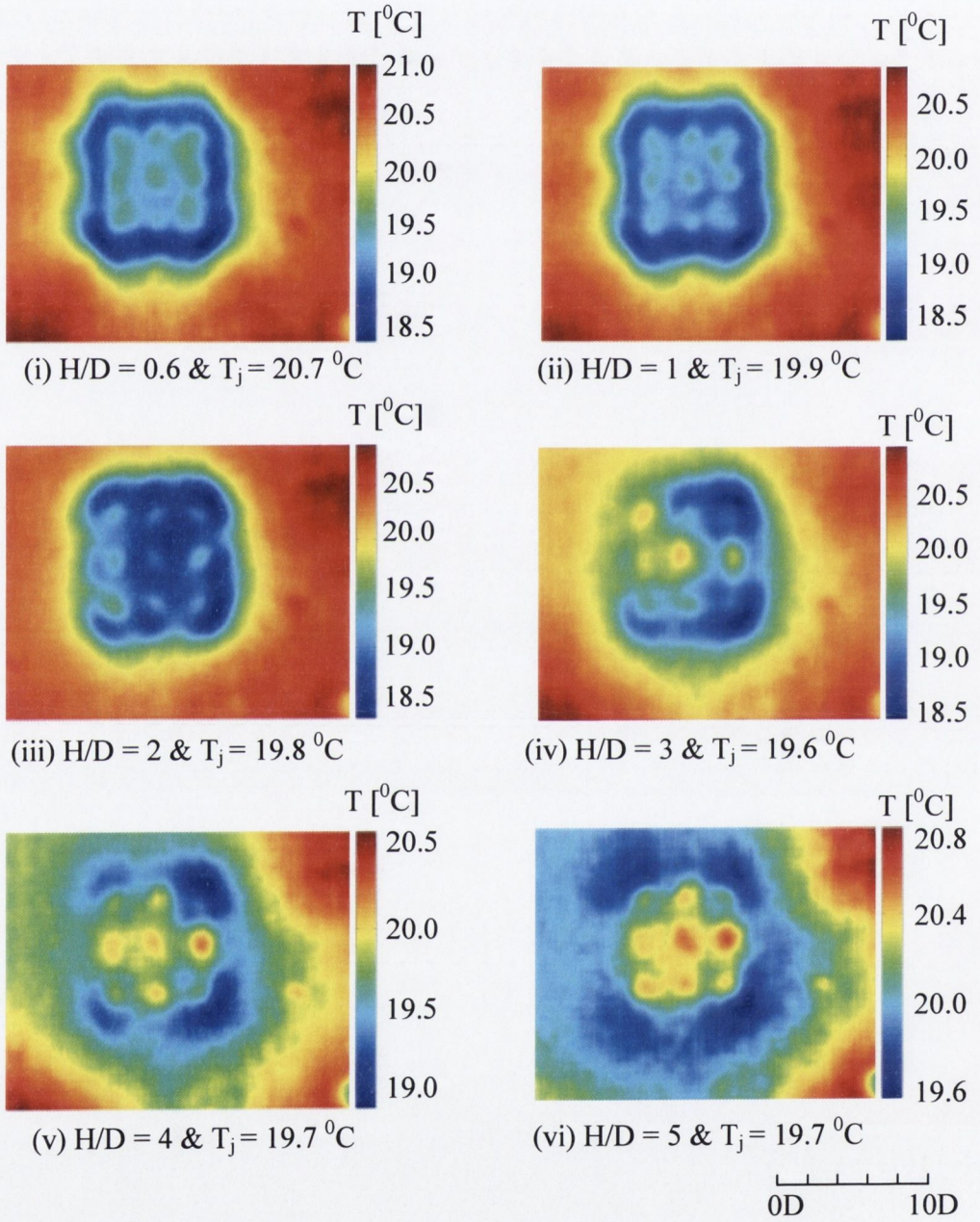(iii) H/D = 2 & T_j = 21.0 ^{0}C

(iv) H/D = 3 & T_j = 21.0 ^{0}C

(v) H/D = 4 & T_j = 21.0 ^{0}C

(vi) H/D = 5 & T_j = 21.0 ^{0}C

C.10 TEMPERATURE DISTRIBUTIONS FOR THE 3×3 JET ARRAY CONFIGURATION WITH RE = 10500 AND S/D = 4.

(i) H/D = 0.6 & T_j = 20.7 ^{0}C

(ii) H/D = 1 & T_j = 21.1 ^{0}C

(iii) H/D = 2 & T_j = 20.9 ^{0}C

(iv) H/D = 3 & T_j = 20.9 ^{0}C

(v) H/D = 4 & T_j = 20.8 ^{0}C

(vi) H/D = 5 & T_j = 21.0 ^{0}C

0D   10D

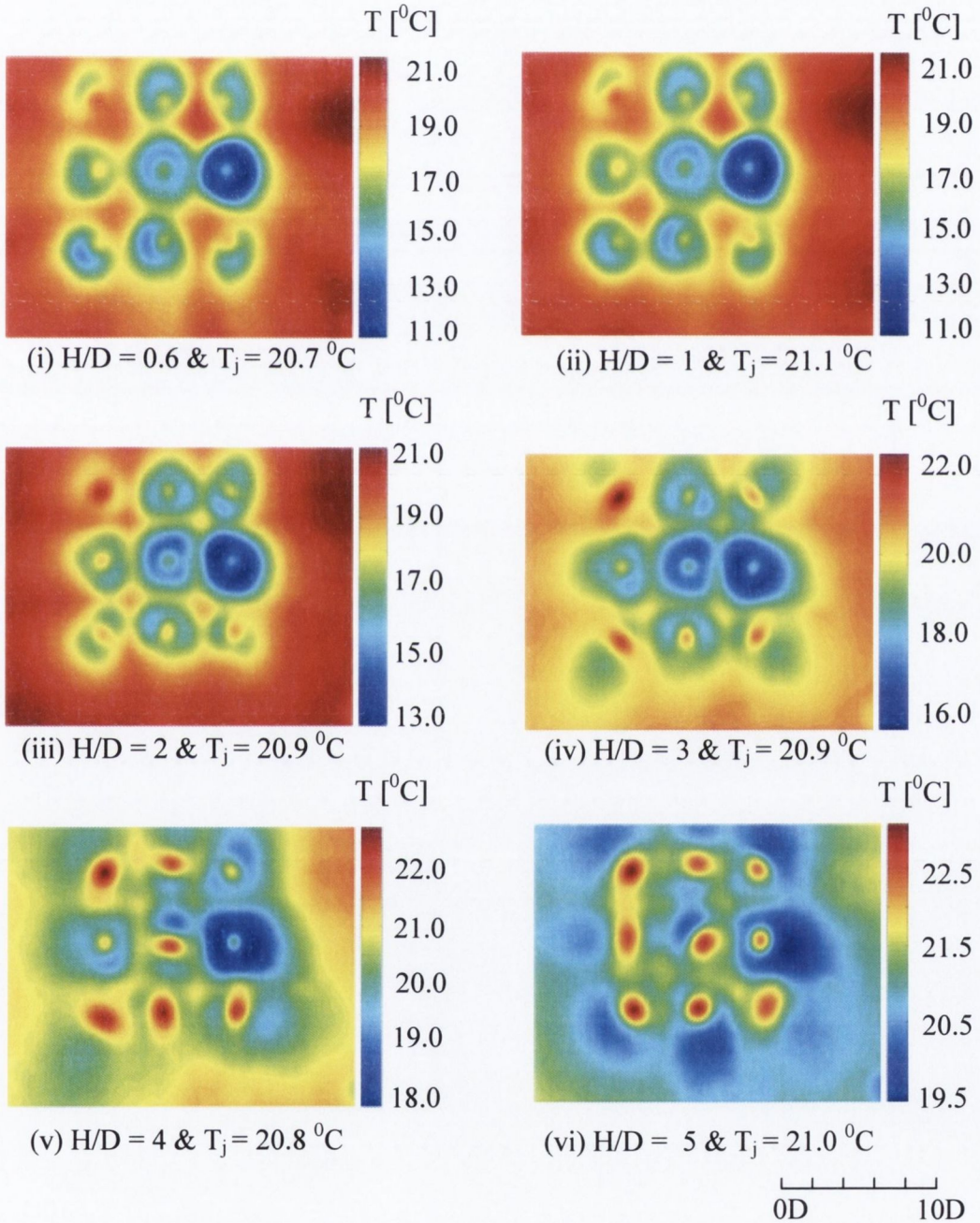# C.11 TEMPERATURE DISTRIBUTIONS FOR THE 3×3 JET ARRAY CONFIGURATION WITH RE = 5100 AND S/D = 6.

(i) H/D = 0.6 & T_j = 20.9 ^{0}C

(ii) H/D = 1 & T_j = 20.9 ^{0}C

(iii) H/D = 2 & T_j = 20.8 ^{0}C

(iv) H/D = 3 & T_j = 21.3 ^{0}C

(v) H/D = 4 & T_j = 21.2 ^{0}C

(vi) H/D = 5 & T_j = 20.9 ^{0}C

0D   10D

C.12 TEMPERATURE DISTRIBUTIONS FOR THE 3×3 JET ARRAY CONFIGURATION WITH $Re = 10500$ AND $S/D = 6$.

(i) H/D = 0.6 & T_j = 20.8 ^{0}C

(ii) H/D = 1 & T_j = 21.2 ^{0}C

(iii) H/D = 2 & T_j = 21.3 ^{0}C

(iv) H/D = 3 & T_j = 21.2 ^{0}C

(v) H/D = 4 & T_j = 21.2 ^{0}C

(vi) H/D = 5 & T_j = 21.3 ^{0}C
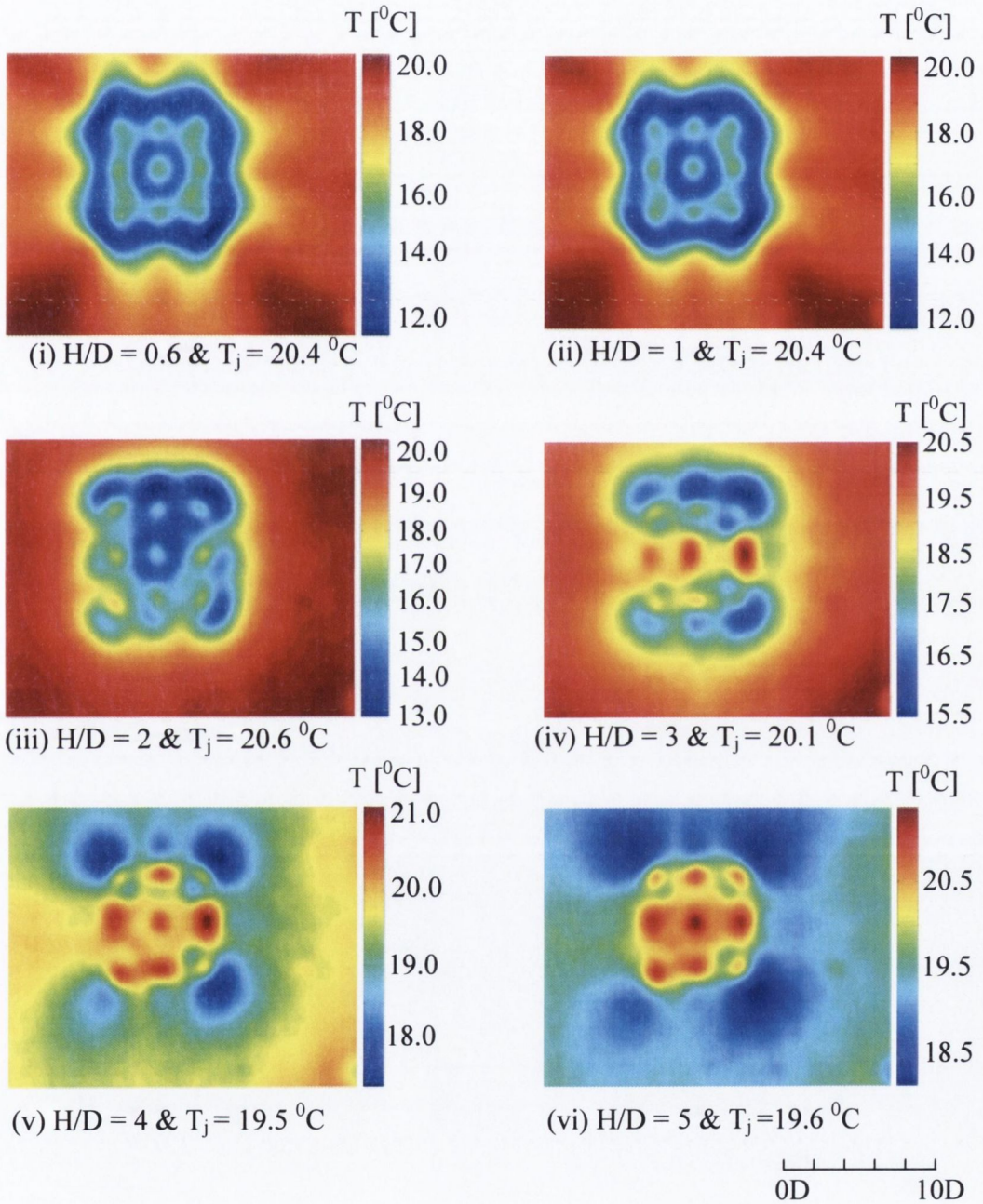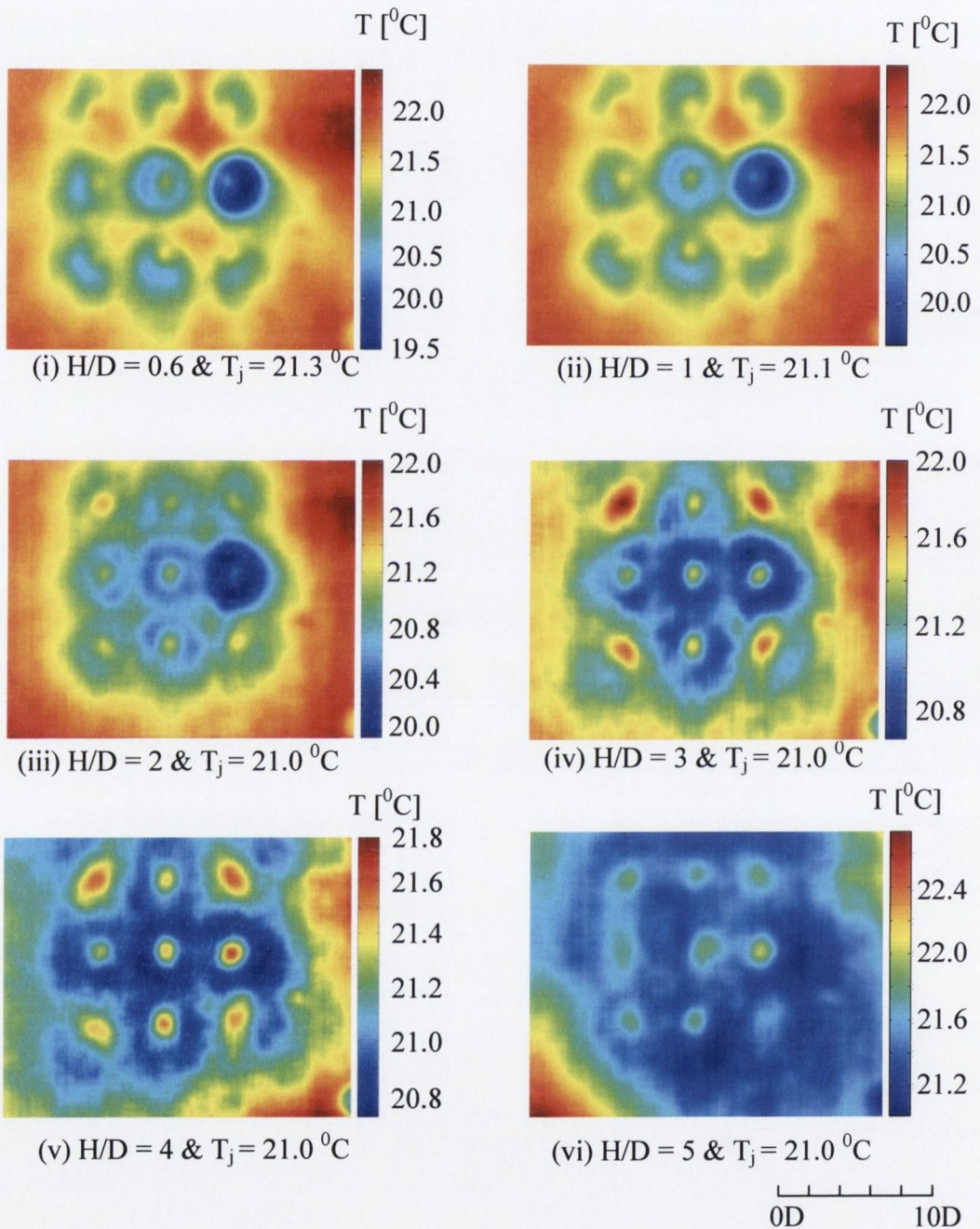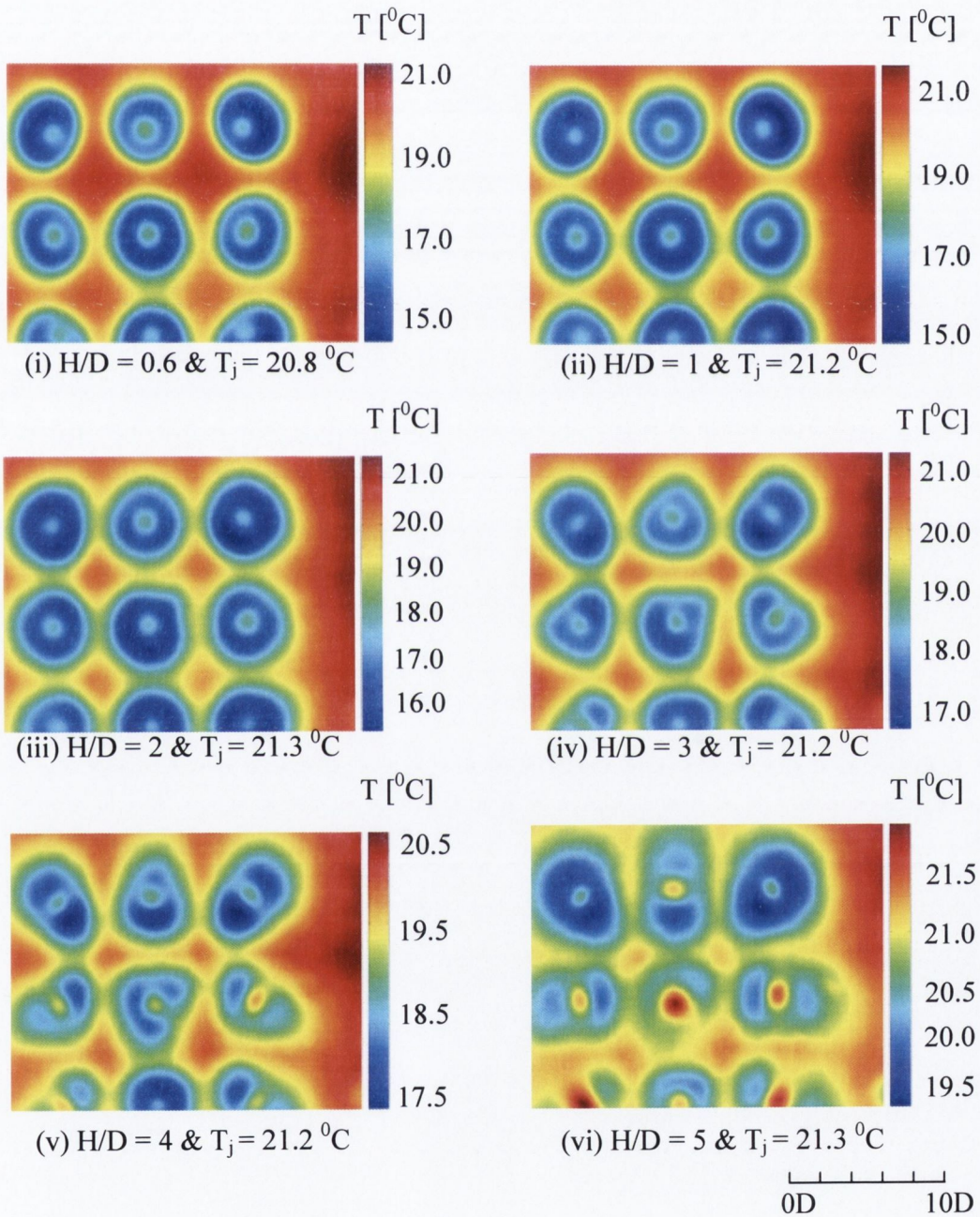
APPENDIX D: MATLAB CODE

This appendix contains the main Matlab code written to analysis the test data. This code allows for the calculation of recovery factor and heat flux due to lateral conduction distributions from temperature data recorded by the IR camera.

```matlab
function main
clc;close all;clear all;

test_name=[
    'adi140409';
    'adi150409';
    'adi160409';
    'adi170409';
    'adi190409';
    'adi200409';
    'adi210409';
    'adi270409';
    ];
neighbourhood=9;% Wiener filter parameter
dx=0.0000475;% pixel size
t=25e-6;% foil thickness
k=16.3;% foil conductivity

%RECOVERY FACTOR AND HEAT FLUX DUE TO LATERAL CONDUCTION ARE
EVALUATED
for test_name_counter=1:7
    for test_number=1:20
```

```matlab
load([test_name(test_name_counter,:),num2str(test_number),'.mat']);
% load a file that contains a test temperature distribution and all
% the test parameters
T_wiener=wiener2(T_calibrated,[neighbourhood,neighbourhood]);
Recovery_factor=1+(T_wiener_11-T_nozzle_exit)/((...
    velocity_nozzle_exit^2)/(2*1005));
for i_=2:length(T_wiener(1,:))-1 %the temperature laplacian is
% evaluated using finite difference
    for j_=2:length(T_wiener(:,1))-1
        temperature_laplacian(j_,i_)=( T_wiener(j_,i_+1)-2*(T_wiener(j_,i_))+...
            T_wiener(j_,i_-1)+ T_wiener(j_+1,i_)-2*(T_wiener(j_,i_))+...
            T_wiener(j_-1,i_) )./(dx^2);
    end
end
temperature_laplacian=wiener2(temperature_laplacian,[ neighbourhood,...
    neighbourhood]);
heat_flux_due_to_lateral_conduction=temperature_laplacian*t*k;
eval(['save ',test_name(test_name_counter,:),num2str(test_number)])
    end
end
```

APPENDIX E: PROJECT PUBLICATIONS

1. Lupton, T.L., Murray, D.B. and Robinson, A.J., "Local Heat Transfer from Micro Impinging Jet Arrays", *ExHFT-7, 7th World Conference on Experimental Heat Transfer, Fluid Mechanics and Thermodynamics*, June 28th - July 3rd, 2009, Krakow, Poland.

2. Lupton, T.L., Murray, D.B. and Robinson, A.J., "Heat Transfer from Micro Impinging Jet Arrays", *Heat Transfer and Fluid Flow in Microscale III*, Sept. 21st – 26th, 2008, Hilton Whistler, BC, Canada.

3. Lupton, T.L., Murray, D.B. and Robinson, A.J., "The Effects of Varying Confinement Levels on the Heat Transfer to a Miniature Impinging Air Jet", *5th European Thermal-Sciences Conference*, May 18th – 22nd, 2008, Eindhoven, The Netherlands.

4. Lupton, T.L., Murray, D.B. and Robinson, A.J., "IR Thermography Measurement of Impinging Jet Heat Transfer from a Heated Thin Foil", *10th UK National Heat Transfer Conference*, Sept. 10th – 11th, 2007, Edinburgh, Scotland.

5. Lupton, T.L., Murray, D.B. and Robinson, A.J., "Confinement Effects in Heat Transfer to a Miniature Compressible Impinging Air Jet", *ASME-JSME Thermal Engineering and Summer Heat Transfer Conference*, July 8th -12th, 2007, Vancouver, British Columbia, Canada.

6. Glynn, C., Robinson, A.J. and Murray, D.B., Lupton, T.L., "Microscale Heat Transfer of Confined Miniature Jets", *ASME , 4th International Conference on Nanochannels, Microchannels and Minichannels*, June 19th – 21st , 2006, Limerick, Ireland.